FINAL

IN-90-CR

IREF

2=15

56857

P.88

FINAL REPORT NAG1-1174

to the

NATIONAL AERONAUTICS AND SPACE ADMINISTRATION

by the

Department of Physics

and the

McDonnell Center for the Space Sciences
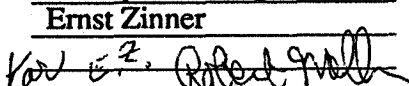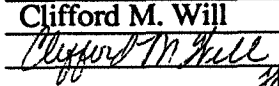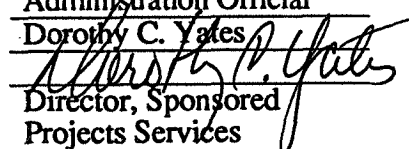
Washington University

St. Louis, MO 63130

Title: Analysis of LDEF Experiment AO187-2 Chemical and Isotopic Measurements of Micrometeoroids by Secondary Ion Mass Spectrometry

Principal Investigator:

Name: Ernst Zinner
               Research Professor of Physics
Soc. Sec. #:   ████████

Fax: 314-935-4083
E-mail: ekz@howdy

Endorsements:

	Principal Investigator	Department Head	Institutional Administration Official
Name:	Ernst Zinner	Clifford M. Will	Dorothy C. Yates
Signature:			Director, Sponsored
Title:	Director	Chairman	Projects Services
Telephone:	314-935-6240	314-935-6276	314-935-6950
Fax:	314-935-4083	314-935-6219	314-935-5862

FINAL REPORT
NASA NAG1-1174

INTRODUCTION

This grant was awarded to enable the analysis of experiment AO187-2 that was flown on board the Long Duration Exposure Facility (LDEF). The results of our work are presented in three scientific papers (1-3) and four abstracts (4-7) copies of which are attached to this report. These publications describe the experiment and analyses in detail and we here only summarize the major conclusions.

The spacecraft was originally scheduled to remain in orbit about one year, but its recovery was delayed due to the Challenger disaster and it actually spent 69 months in near-earth orbit, being recovered just prior to the time when it would have re-entered (catastrophically) on its own.

Experiment AO187-2 was designed to measure the chemical and isotopic compositions of interplanetary dust impinging on the spacecraft from outer space. Information on the nature and composition of orbital debris was also anticipated. The spacecraft maintained a constant orientation with respect to its velocity vector thereby defining leading and trailing edges that faced respectively into and away from the direction of motion. Arrays of individual capture cells each 80.8 cm^2 in size and totaling 237 in number were exposed on both the leading and trailing edges of LDEF. Each cell consisted of a pure Ge target surface slightly separated from a thin (2.5 μm) metallized plastic "entrance foil." The basic concept was that incoming projectiles would penetrate the foil, strike the Ge target plate at high velocity producing a vapor-liquid cloud that would re-deposit material on the underside of the plastic foil. This material would then be analyzed using the sensitive surface analysis technique of Secondary Ion Mass Spectrometry (SIMS).

In practice, most of the plastic entrance foils failed during the extended period of orbital exposure probably due to a combination of UV embrittlement, large densities of impact events and (for the leading edge) the effects of atomic oxygen erosion in orbit. However the foils failed gradually and most remained in place on the capture cells for a significant fraction of the duration of the flight. Because most of the impactors were small (<10 μm) they were heated and dispersed in traversing the entrance foils producing clouds of molten droplets and vapor that produced easily identifiable "extended impacts" on the Ge target plates. Fortunately, it proved possible to make ion probe measurements of projectile compositions from material deposited on the Ge in the extended impact structures.

In what follows, we first summarize the salient scientific results obtained from AO187-2. We then describe an extension of this work to the analysis of impacts on flat Au targets that were used in a closely related experiment AO187-1 whose PI is F. Hörz of the Johnson Spacecraft

Center. In a development potentially relevant to future flight experiments, we next describe how it is possible to determine impactor trajectories by comparing the erosion patterns produced by atomic oxygen with the geometry of the extended impacts. As part of this grant, we received a supplement from a Special Investigators Group (SIG) to devise and construct a novel ion imaging system for the SIMS instrument. While this system did not lead to better isotopic analyses of the LDEF impacts as we had hoped, we show briefly how it has proven enormously valuable in the closely related study of cosmic dust supported by NASA in its Planetary Materials Program.

The analysis of AO187 was terminated by NASA before all the information could be extracted from the LDEF materials. In a final section, we underscore the importance of preserving the experimental materials for future studies and describe the current state of the materials and our plans for their future safekeeping.

We note in passing that nine of the capture cells were transferred to scientists at the MBB company in Munich, Germany, as per the attached letters of agreement with MBB negotiated by NASA and ourselves in 1990. As far as we know these cells have not been analyzed using appropriate experimental techniques.

MAJOR RESULTS FROM AO187-2

1. The basic capture cell design worked successfully. As long as the entrance foils stayed in place projectile particles produced "extended impacts" that could be successfully analyzed by ion probe mass spectrometry (SIMS).
2. Even in the cases (the majority) where the entrance foils failed during flight, "extended impacts" registered on the Ge target plates gave sufficiently intense SIMS signals to permit elemental analyses of the projectiles. In contrast, SEM-EDS signals were not found for these same impacts showing that SIMS was essential for the analysis.
3. Measurement of over 60 extended impacts showed that at least 75% of the trailing edge events were produced by cosmic dust particles whereas virtually all the leading edge impacts were produced by man-made orbital debris.
4. The very thin deposits found in AO187-2 precluded measurements of isotopic ratios in all save one of the extended impacts using the SIMS technology available to us at the time. An attempt to devise an improved method for isotopic measurements of thin deposits using ion imaging was not successful.
5. Most extended impacts have compositions that differ markedly from those measured for IDPs collected in the stratosphere. The differences are consistent with volatile/refractory element fractionation affecting particles with cosmic compositions. This effect had previously been seen by us in simulation experiments of hypervelocity impacts, but is more pronounced in the

LDEF data, probably due to the high velocities of the impactors. <u>Elemental fractionation in the impact process itself represents the largest single impediment to accurate measurement of projectile chemistry.</u>

6.   Contamination of initially clean Ge surfaces during exposure in space was also found to be a significant effect limiting the ability to make accurate measurements of projectile chemistry. The source of the Si background seems to be outgassing from RTV, but other contaminant sources, contributing elements such as Mg and Al, are still unidentified.

RELATED STUDIES OF FLAT PLATE IMPACTS ON A0187-1

In reference 3 and in a separate final report for NASA grant NAG 9-684, we describe our closely related SIMS work on impacts registered in flat sheets of gold in experiment AO187-1 (F. Hörz, Johnson Space Center, PI). By pushing the target from the back against a flat plate, it was possible to create a geometry suitable for SIMS analysis. In some low velocity impacts it was possible to obtain good isotopic data on distributed chunks of projectile material. No isotopic anomalies were found in C, N, Mg, or Si. This is not inconsistent with measurements on interplanetary dust particles collected in the stratosphere where large anomalies are common in H and to a lesser extent in N but not in C, Si, or Mg. As in the case of AO187-2, it was sometimes possible to obtain reasonable SIMS data for which no SEM-EDS signals could be found.

TRAJECTORY DETERMINATION OF INDIVIDUAL IMPACTORS

As described in the attached extended abstract by one of our co-investigators, F. Stadermann [7] an unexpected phenomenon caused by the interaction of atomic oxygen with surfaces makes it possible to determine the angle of impact for certain projectiles. When a hole is produced in the entrance foil of a leading edge cell by an impacting particle, atomic oxygen will enter the hole with the stream direction parallel to the ram direction of the spacecraft. This produces on the Ge a characteristic oval discoloration pattern whose center of gravity is displaced from the center of gravity of the extended impact feature itself, the latter being determined by the initial direction of the impactor. In the future, such measurements coupled with independent determinations of the times at which specific events occurred could be used to determine the absolute trajectories of individual particles which could then be correlated with the measured compositions to give a more complete characterization of the meteoroid and debris complex.

DEVELOPMENT OF A NEW ION IMAGING SYSTEM AND ITS APPLICATION TO COSMIC DUST STUDIES

This grant received funding from the Special Investigators Group for Meteoroid and Orbital debris to implement a new ion imaging system for the Cameca IMS-3F ion microprobe used by us for the SIMS analyses. It was hoped that ion images could be used to define regions of thicker deposits for which the sequential measurement of masses could be used to obtain reliable isotopic data. However, we were not able to use the imaging to obtain useful isotopic data on the extended impacts.

However, the imaging system that was developed has proven enormously successful for locating rare interstellar dust grains in acid residues of certain primitive meteorites. For example, we were able to locate interstellar grains (as manifested by their very unusual $^{16}O/^{18}O$ ratios) of aluminum oxide even though such grains constitute only 10^{-2} to 10^{-3} of all aluminum oxide grains present in the mineral separates [8]. Another recent example of the power of the ion imaging system to locate rare interstellar grains is the isolation of large numbers of X-type SiC grains for detailed study [9].

IMPORTANCE OF PRESERVING LDEF MATERIALS FOR FUTURE SCIENTIFIC STUDY

As we previously pointed out in Reference 3:

"The extended impacts of LDEF experiment A0187-2 that have already been partially studied by existing SIMS techniques *represent an extremely important scientific resource for future work.* In particular, some of these impacts may make it possible to measure the isotopic composition of cometary material. Dust particles from long-period comets encounter the earth with very high velocities and are thus preferentially destroyed relative to slower asteroidal particles during atmospheric entry. Cometary particles may thus be grossly underrepresented in the stratospheric micrometeoroid collections. In contrast, high velocity particles produce extended impacts with high efficiency and should thus be well represented in the existing collection of capture cell impacts.

"Because of their potential scientific importance, continued care should be taken to store the relevant surfaces of experiment AO187-2 under clean conditions so they may be properly analyzed by future improved analytical instruments."

Attached to this final report is a current printout of the hypercard data system used to keep track of the location and current status of various measurements on specific impacts. It is our
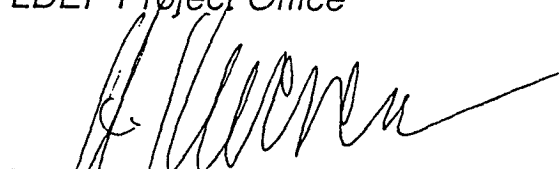
MEMORANDUM OF UNDERSTANDING

PROCESSING OF CAPTURE CELLS ON EXPERIMENT S1002
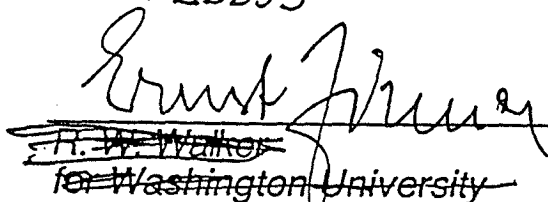
1. Demount all capture cells (N = 11) with intact foils and prepare for shipment to Washington University, St. Louis.

2. Demount an additional 57 capture cells and prepare for shipment to Washington University, St. Louis.

3. Leave 9 cells, ~~along an entire diagonal row of the capture cell array in their original configuration~~ *To Be selected at the time of Tray removal* and prepare for shipment to the Principle Investigator, MBB.

4. Provide access to additional LDEF hardware to the TU Munchen to study man-made and natural particle populations.

5. Document large impact feature on sandwich-baseplate and remove from hardware in SAEF II as part of the M&D SIG activities/sample acquisition efforts. These materials are on loan to the M&D SIG. After completional of the analyses, the materials will be returned to the Principle Investigator / MBB.

_____ 2/9/90
W. H. Kinard
LDEF Project Office

_____ 2/9/90
H. Kuczera
for L. Preess, MBB
PREUSS

_____
~~H. W. Walker~~
~~for Washington University~~
ERNST ZINNER
for WASHINGTON UNIO. W/C 2/9/90

MEMORANDUM OF CONCURRENCE

I have read the attached Memorandum of Agreement concerning processing of capture cells on LDEF Experiment S1002 entitled "Investigation of Critical Surface Degradation Effects on Coatings and Solar Cells Developed in Germany," and I concur with this agreement.

Ludwig Preuss   02/13/90
MBB Space Division   Date

Long Duration Exposure Facility
A0187-2 summary sheets
to 6/23/95

	E08	E03	C02
Total cells on	116	72	40
cells optically analyzed to date	112	72	40

optically seen Extended impacts A

sw	sp	cd	ri	total
157	259	32	35	483

possible extended impacts A:

Total: 204

number examined in sem: 18

number reclassified as Extended impact A: 7

number reclassified as Extended impact B: 6

TOTAL NUMBER OF EXTENDED IMPACTS A:

Impacts cut out for ion probe analysis: 86

Impacts analyzed in the SEM: 136

Impacts analyzed by Ion Probe: 83

Summary of Trailing Edge Covered Cells

optically seen Extended impacts A

sw	sp	cd	ri
4	5	5	6

possible extended impacts A

Total: 5

number examined in sem: 1

number reclassified as Extended impact A: 1

number reclassified as Extended impact B: 0

Impacts cut out for ion probe analysis: 18

Impacts analyzed in the SEM: 41

Impacts analyzed by Ion Probe: 18

Summary of Trailing Edge Uncovered Cells

optically seen Extended impacts A

sw	sp	cd	ri
23	7	12	5

possible extended impacts A

Total: 157
number examined in sem: 13
number reclassified as Extended impact A: 5
number reclassified as Extended impact B: 3

TOTAL NUMBER OF EXTENDED IMPACTS A:

Impacts cut out for ion probe analysis: 43
Impacts analyzed in the SEM: 51
Impacts analyzed by Ion Probe: 40

Summary of Leading Edge Cells

optically seen Extended impacts A

sw	sp	cd	ri
130	247	15	24

possible extended impacts A

Total: 42
number examined in sem: 4
number reclassified as Extended impact A: 1
number reclassified as Extended impact B: 3

TOTAL NUMBER OF EXTENDED IMPACTS A:

Impacts cut out for ion probe analysis: 25
Impacts analyzed in the SEM: 44
Impacts analyzed by Ion Probe: 25

summary of data analyzed to 6/23/95

cell		extended impacts A					extended impacts B					craters
		sw	sp	cd	ri	total	sw	sp	cd	ri	total	
C02-1-10		0	0	0	0	0	0	0	0	0	0	1
C02-1-11		0	0	0	0	0	0	0	0	0	0	2
C02-1-12		0	0	1	0	1	0	0	0	0	0	3
C02-1-13		0	0	0	0	0	0	0	0	0	0	3
C02-1-14		1	0	0	0	1	0	0	0	2	2	2
C02-1-15		0	0	1	0	1	1	0	0	2	3	1
C02-1-16		0	0	0	0	0	0	0	1	0	1	2
C02-1-17		0	0	0	0	0	0	0	0	0	0	2
C02-1-18		0	0	0	0	0	0	0	0	0	0	1
C02-1-19		0	0	0	0	0	1	0	0	0	1	4
C02-1-1		0	0	0	0	0	0	0	0	0	0	2
C02-1-20		1	0	0	0	1	0	0	0	1	1	1
C02-1-2		0	0	0	0	0	0	0	0	0	0	1
C02-1-3		2	0	0	0	2	1	0	0	1	2	0
C02-1-4		0	0	0	0	0	0	0	0	0	0	2
C02-1-5		0	0	0	0	0	2	0	0	0	2	3

summary of data analyzed to 6/23/95

cell		extended impacts A					extended impacts B					craters
		sw	sp	cd	ri	total	sw	sp	cd	ri	total	
C02-1-6		0	0	0	0	0	2	0	0	0	2	0
C02-1-7		0	0	0	0	0	0	0	0	0	0	0
C02-1-8		1	0	0	0	1	0	0	0	0	0	1
C02-1-9		0	0	0	0	0	0	0	0	0	0	3
C02-2-10		0	0	0	1	1	0	0	0	0	0	2
C02-2-11		1	0	0	0	1	0	0	0	0	0	2
C02-2-12	C	0	1	2	1	4	0	0	1	2	3	0
C02-2-13		1	0	0	0	1	0	0	0	0	0	1
C02-2-14		1	0	0	0	1	0	0	0	0	0	2
C02-2-15		0	0	0	0	0	0	0	0	2	2	5
C02-2-16		1	0	0	0	1	0	0	0	2	2	2
C02-2-17		0	0	1	0	1	0	0	0	0	0	0
C02-2-18		0	0	1	0	1	1	0	0	0	1	2
C02-2-19		0	0	0	0	0	0	0	0	0	0	2
C02-2-1		0	0	0	0	0	0	0	0	1	1	2
C02-2-20		0	0	0	0	0	0	0	0	0	0	5

summary of data analyzed to 6/23/95

cell		extended impacts A					extended impacts B					craters
		sw	sp	cd	ri	total	sw	sp	cd	ri	total	
C02-2-2		0	0	0	0	0	0	0	0	0	0	2
C02-2-3		0	0	0	0	0	0	0	0	0	0	1
C02-2-4		1	0	0	0	1	0	0	0	1	1	1
C02-2-5		1	0	0	0	1	0	0	0	1	1	3
C02-2-6		0	0	0	0	0	0	0	0	0	0	1
C02-2-7		0	0	0	0	0	0	0	0	0	0	5
C02-2-8		1	0	0	1	2	0	0	0	1	1	0
C02-2-9		0	0	0	0	0	0	0	0	0	0	4
E03-1-14		0	0	0	0	0	0	1	0	0	1	1
E03-1-15	C	0	2	0	0	2	0	3	0	2	5	0
E03-1-22		1	0	0	0	1	0	0	0	0	0	1
E03-1-23		0	0	0	0	0	0	0	0	1	1	4
E03-1-24		0	0	0	0	0	0	0	0	0	0	3
E03-1-2	C	1	0	0	1	2	0	0	0	1	1	0
E03-1-30		0	1	0	0	1	0	0	0	2	2	3
E03-1-31	C	0	0	0	0	0	0	1	0	0	1	0

summary of data analyzed to 6/23/95

cell		extended impacts A					extended impacts B					craters
		sw	sp	cd	ri	total	sw	sp	cd	ri	total	
E03-1-32		0	0	1	0	1	0	0	0	0	0	2
E03-1-33	C	1	0	0	0	1	0	0	0	1	1	0
E03-1-39		1	0	0	0	1	0	0	0	0	0	2
E03-1-3		0	0	0	0	0	0	0	0	2	2	1
E03-1-40		0	0	1	0	1	0	0	0	0	0	2
E03-1-41		0	0	0	0	0	0	0	0	0	0	0
E03-1-42		0	0	1	0	1	0	1	0	0	1	0
E03-1-5		0	0	0	0	0	1	0	0	0	1	5
E03-1-6		1	0	0	0	1	0	0	0	0	0	7
E03-1-8		0	0	0	0	0	0	0	0	1	1	0
E03-2-10		0	0	0	0	0	0	0	0	0	0	5
E03-2-11	C	1	0	1	0	2	0	2	0	1	3	0
E03-2-12		1	1	0	0	2	4	1	1	3	9	2
E03-2-13		0	0	0	0	0	0	1	0	2	3	0
E03-2-16		0	0	0	0	0	0	2	0	0	2	2
E03-2-17		0	0	0	0	0	0	0	0	0	0	1

summary of data analyzed to 6/23/95

cell		extended impacts A					extended impacts B					craters
		sw	sp	cd	ri	total	sw	sp	cd	ri	total	
E03-2-18		0	0	0	0	0	1	26	0	0	27	2
E03-2-19		1	0	0	0	1	0	0	0	0	0	0
E03-2-20		0	0	0	0	0	0	2	0	1	3	3
E03-2-25		0	0	0	0	0	0	0	0	0	0	1
E03-2-26		0	0	0	0	0	0	3	0	1	4	2
E03-2-27		0	0	1	0	1	0	0	0	0	0	1
E03-2-28		1	1	0	0	2	0	0	1	1	2	0
E03-2-29		0	0	0	0	0	1	0	0	0	1	2
E03-2-34		0	0	0	0	0	0	2	0	0	2	2
E03-2-35		0	0	0	0	0	0	1	1	1	3	1
E03-2-36		0	0	0	0	0	0	1	0	0	1	1
E03-2-37		2	0	0	0	2	0	0	0	2	2	7
E03-2-38		0	0	0	0	0	0	0	0	1	1	6
E03-2-9		0	1	0	0	1	0	0	0	0	0	7
E03-3-43		0	0	1	0	1	0	1	0	0	1	6
E03-3-44		0	0	0	0	0	0	0	0	0	0	0

summary of data analyzed to 6/23/95

cell		extended impacts A					extended impacts B					craters
		sw	sp	cd	ri	total	sw	sp	cd	ri	total	
E03-3-45		0	0	0	0	0	0	0	0	0	0	0
E03-3-46		0	0	1	0	1	0	0	0	0	0	9
E03-3-52		1	0	0	0	1	1	1	0	1	3	0
E03-3-53		0	0	1	0	1	0	0	0	1	1	7
E03-3-54	C	0	0	0	0	0	0	2	0	4	6	0
E03-3-55		0	0	0	0	0	0	0	0	0	0	0
E03-3-61	C	0	0	1	1	2	0	0	0	0	0	0
E03-3-62		0	1	1	1	3	0	6	0	0	6	0
E03-3-63		0	0	0	1	1	0	1	0	0	1	0
E03-3-64		0	0	0	0	0	0	1	0	0	1	1
E03-3-70		0	0	0	0	0	0	30	0	0	30	0
E03-3-71	C	0	0	1	2	3	0	0	0	0	0	0
E03-3-72		0	0	0	0	0	0	5	0	0	5	6
E03-3-73		0	0	0	0	0	0	3	0	0	3	1
E03-4-47		1	0	0	0	1	0	0	1	4	5	0
E03-4-48		0	0	0	0	0	0	1	0	0	1	4

summary of data analyzed to 6/23/95

cell		extended impacts A					extended impacts B					craters
		sw	sp	cd	ri	total	sw	sp	cd	ri	total	
E03-4-49		0	0	0	0	0	0	0	0	0	0	2
E03-4-50		0	0	0	0	0	0	2	0	1	3	0
E03-4-56	C	1	0	0	0	1	0	0	0	5	5	2
E03-4-57		0	0	0	0	0	0	0	0	1	1	4
E03-4-58		0	0	0	0	0	0	0	0	0	0	0
E03-4-59		0	1	0	0	1	0	2	0	1	3	1
E03-4-60		0	0	0	0	0	0	0	0	1	1	1
E03-4-65		0	0	0	0	0	0	0	0	0	0	1
E03-4-66		0	0	0	0	0	0	0	0	0	0	3
E03-4-67		1	0	0	0	1	0	0	0	0	0	0
E03-4-68		0	0	0	0	0	0	0	0	0	0	4
E03-4-69		0	0	0	0	0	0	0	0	0	0	1
E03-4-74		0	0	0	0	0	0	0	0	0	0	0
E03-4-75	C	0	2	0	0	2	0	0	0	0	0	0
E03-4-76	C	0	0	0	1	1	0	0	0	1	1	0
E03-4-77		0	1	0	1	2	0	0	0	1	1	0

summary of data analyzed to 6/23/95

cell		extended impacts A					extended impacts B					craters
		sw	sp	cd	ri	total	sw	sp	cd	ri	total	
E08-1-10		0	0	0	0	0	0	1	0	0	1	73
E08-1-12		1	5	0	0	6	0	9	0	0	9	48
E08-1-13		0	1	0	0	1	0	0	0	0	0	70
E08-1-14		1	2	0	0	3	1	2	0	0	3	36
E08-1-15		0	2	0	0	2	0	1	0	0	1	64
E08-1-16		0	0	0	0	0	0	1	1	0	2	95
E08-1-17		0	0	0	0	0	0	2	0	0	2	62
E08-1-18		0	0	0	0	0	0	0	0	0	0	86
E08-1-19		2	0	0	0	2	0	1	0	0	1	34
E08-1-1		0	3	0	0	3	1	2	0	0	3	51
E08-1-20		0	0	1	0	1	1	0	0	0	1	35
E08-1-2		1	5	0	1	7	0	0	0	0	0	48
E08-1-3		2	2	0	0	4	0	0	0	0	0	75
E08-1-4		0	2	0	0	2	0	10	0	0	10	62
E08-1-5		2	4	0	0	6	0	7	0	0	7	76
E08-1-6		0	2	1	0	3	1	1	1	0	3	45

summary of data analyzed to 6/23/95

cell	extended impacts A					extended impacts B					craters
	sw	sp	cd	ri	total	sw	sp	cd	ri	total	
E08-1-7	0	0	0	0	0	0	0	0	0	0	88
E08-1-9	2	0	0	0	2	0	0	0	0	0	24
E08-2-10	0	1	0	0	1	0	2	0	0	2	63
E08-2-11	1	0	0	0	1	0	1	0	0	1	41
E08-2-12	2	1	0	0	3	0	1	0	1	2	56
E08-2-13	0	1	0	1	2	0	2	0	0	2	39
E08-2-14	0	0	0	0	0	0	0	1	0	1	47
E08-2-15	2	2	0	0	4	1	0	0	0	1	50
E08-2-16	0	4	0	1	5	0	2	0	1	3	30
E08-2-17	0	4	0	0	4	0	0	2	0	2	59
E08-2-18	0	4	0	0	4	0	4	0	0	4	42
E08-2-19	3	2	1	0	6	0	1	1	0	2	65
E08-2-1	0	1	0	0	1	0	1	0	0	1	29
E08-2-20	0	1	0	0	1	1	2	0	1	4	34
E08-2-2	0	0	0	0	0	0	0	0	0	0	85
E08-2-3	0	2	1	0	3	0	0	0	0	0	99

summary of data analyzed to 6/23/95

cell	extended impacts A					extended impacts B					craters
	sw	sp	cd	ri	total	sw	sp	cd	ri	total	
E08-2-4	0	0	0	0	0	0	0	0	0	0	53
E08-2-5	0	0	0	0	0	0	0	0	0	0	100
E08-2-6	0	4	1	0	5	0	1	0	0	1	77
E08-2-7	3	0	0	0	3	0	0	2	0	2	52
E08-2-8	0	3	0	0	3	0	4	0	0	4	48
E08-2-9	0	2	0	0	2	0	2	0	0	2	60
E08-3-10	2	4	0	1	7	0	3	2	0	5	38
E08-3-11	2	6	0	0	8	1	4	0	1	6	41
E08-3-12	1	0	0	0	1	1	0	0	0	1	58
E08-3-13	2	1	0	1	4	0	0	0	3	3	66
E08-3-14	0	0	0	0	0	0	0	0	0	0	67
E08-3-15	0	2	0	0	2	0	0	0	0	0	85
E08-3-16	0	0	0	0	0	2	0	1	0	3	78
E08-3-17	0	0	0	0	0	1	0	0	0	1	77
E08-3-18	1	2	0	0	3	1	1	0	0	2	57
E08-3-19	2	4	0	0	6	2	4	0	2	8	32

summary of data analyzed to 6/23/95

cell		extended impacts A					extended impacts B					craters
		sw	sp	cd	ri	total	sw	sp	cd	ri	total	
E08-3-1		1	2	0	0	3	0	0	0	0	0	71
E08-3-20		0	2	0	0	2	2	4	0	1	7	39
E08-3-2		0	1	0	0	1	0	0	0	0	0	84
E08-3-3		0	2	0	0	2	0	0	0	0	0	67
E08-3-4		1	3	0	0	4	0	4	0	0	4	41
E08-3-5		4	5	0	0	9	2	2	0	2	6	53
E08-3-6		0	4	0	0	4	0	4	1	0	5	55
E08-3-7		1	2	0	0	3	0	1	0	1	2	48
E08-3-9		0	0	0	0	0	0	0	0	0	0	31
E08-4-10		1	6	0	0	7	2	2	0	1	5	38
E08-4-11		0	4	0	0	4	0	0	0	0	0	44
E08-4-12		1	0	0	0	1	0	1	0	0	1	65
E08-4-13		2	0	0	0	2	0	0	0	0	0	30
E08-4-14		0	4	0	1	5	0	0	0	0	0	29
E08-4-15		5	8	1	0	14	0	1	0	0	1	22
E08-4-16		0	2	1	0	3	0	1	0	0	1	20

summary of data analyzed to 6/23/95

cell		extended impacts A					extended impacts B					craters
		sw	sp	cd	ri	total	sw	sp	cd	ri	total	
E08-4-18		1	1	0	0	2	1	1	0	1	3	23
E08-4-19		3	2	0	0	5	0	2	0	2	4	19
E08-4-1		1	2	0	1	4	0	1	0	0	1	45
E08-4-20		1	1	0	0	2	0	1	1	0	2	59
E08-4-2		1	2	0	0	3	3	2	0	0	5	50
E08-4-3		1	2	0	1	4	1	3	0	0	4	23
E08-4-4		0	1	0	0	1	0	2	0	0	2	19
E08-4-5		1	4	0	0	5	0	0	0	1	1	36
E08-4-6		0	2	0	0	2	1	0	0	0	1	72
E08-4-7		1	4	0	0	5	1	2	1	2	6	42
E08-4-9		0	1	0	0	1	0	1	0	0	1	19
E08-5-10		0	1	0	0	1	0	0	1	0	1	49
E08-5-11		3	5	0	0	8	1	2	0	0	3	66
E08-5-12		2	5	0	0	7	2	1	0	0	3	13
E08-5-13		0	3	0	1	4	2	1	1	3	7	48
E08-5-14		1	1	0	0	2	1	0	0	2	3	45

summary of data analyzed to 6/23/95

cell	extended impacts A					extended impacts B					craters
	sw	sp	cd	ri	total	sw	sp	cd	ri	total	
E08-5-15	0	0	0	0	0	0	0	0	1	1	72
E08-5-16	0	3	0	1	4	0	2	0	0	2	60
E08-5-17	8	3	0	0	11	0	5	0	1	6	21
E08-5-18	3	2	2	0	7	0	11	0	0	11	10
E08-5-19	7	4	0	0	11	0	0	0	1	1	22
E08-5-1	1	0	0	1	2	0	0	3	0	3	59
E08-5-20	0	0	2	1	3	2	0	1	0	3	56
E08-5-2	0	4	0	0	4	0	4	1	1	6	45
E08-5-3	1	2	1	0	4	1	3	0	0	4	91
E08-5-4	0	0	0	1	1	0	0	1	0	1	60
E08-5-5	1	3	0	0	4	3	6	0	0	9	68
E08-5-6	0	2	0	2	4	0	1	0	0	1	50
E08-5-7	6	1	0	0	7	0	4	0	1	5	31
E08-5-8	0	3	0	0	3	0	1	0	0	1	29
E08-5-9	2	3	0	1	6	1	5	0	2	8	20
E08-6-10	0	4	0	0	4	0	1	0	0	1	50

summary of data analyzed to 6/23/95

cell	extended impacts A					extended impacts B					craters
	sw	sp	cd	ri	total	sw	sp	cd	ri	total	
E08-6-12	0	1	0	0	1	2	1	0	0	3	14
E08-6-13	5	2	1	1	9	0	3	0	2	5	29
E08-6-14	0	1	0	0	1	0	0	0	3	3	41
E08-6-15	1	1	0	0	2	0	0	2	1	3	45
E08-6-16	3	2	0	1	6	0	2	0	0	2	28
E08-6-17	8	6	0	0	14	1	1	0	1	3	23
E08-6-18	1	0	1	0	2	0	1	0	0	1	58
E08-6-19	0	2	1	0	3	3	1	0	0	4	38
E08-6-1	2	5	0	0	7	0	0	0	0	0	19
E08-6-20	1	5	0	0	6	4	2	1	4	11	48
E08-6-2	2	1	0	1	4	0	5	0	0	5	26
E08-6-5	3	4	0	2	9	0	3	0	0	3	29
E08-6-6	3	10	0	0	13	0	0	0	0	0	17
E08-6-7	6	6	0	3	15	3	3	0	1	7	15
E08-6-8	2	5	0	0	7	0	1	0	0	1	10
E08-6-9	0	1	0	0	1	0	3	0	0	3	29

summary of extended impacts A
as of 6/23/95

impact name		type of impact	size	comments	analysis to date
C02 1 15B 2		crater	3800		sem sims
E03 3 46A 1		crater	3200		sem sims
C02 2 17C 1		crater	3000	crater 800	sem sims
C02 1 12C 2		crater	2400	crater 700um	sem sims
E03 1 42A 1		crater	2100	crater 1000um, surrounding spray (?) 2100um	none
E08 2 6C 11		crater	2100	caused much damage	none
E08 5 18A 2		crater	1792	half of cr impact destroyed edge, cracks extend, debris visible inside as well as white substance	none
E03 1 32B 1		crater	1600	hard to judge whether it is cd or sp. promising for ion probe analysis	none
E03 3 43C 3		crater	1600		sem sims

summary of extended impacts A
as of 6/23/95

impact name		type of impact	size	comments	analysis to date
E08 4 16A 9		crater	1344	through wafer, debris visible inside, cracks extend, some debris on wafer below crater, white dust?	none
E03 3 53B 1		crater	1200		sem
E08 4 15C 6		crater	1120		sem sims
E03 2 11A 2	C	crater	1040		sem sims
C02 2 18B 1		crater	1000		sem sims
E08 2 3D 11		crater	900	erosion too	none
C02 2 12B 1	C	crater	800		sem
E03 1 40B 1		crater	800		sem sims
E03 3 61D 2	C	crater	800		sem
E08 6 18A 1		crater	720	debris mostly on edge	none
E08 6 19D 10		crater	720	debris extends out	none
E03 3 71C 1	C	crater	640		sem
E03 2 27D 1		crater	600		sem sims

summary of extended impacts A
as of 6/23/95

impact name		type of impact	size	comments	analysis to date
E03 3 62B 1		crater	540		sem sims
C02 2 12D 2	C	crater	480	relatively small	sem sims
E08 6 13D 15		crater	480	large debris area	none
E08 5 18B 3		crater	336	w/ extensive spray	none
E08 2 19C 12		crater	300	debris over wide area	none
E08 1 20A 1		crater	280		none
E08 1 6C 8		crater	224	looks very promising	none
E08 5 20B 6		crater	224		sem
E08 5 20C 2		crater	168		none
E08 5 3C 18		crater	?900	white substance inside	none
C02 2 8A 2		ring	800		sem sims
E03 4 77D 1		ring	800	melting zone	sem sims
E03 1 2A 1	C	ring	720		sem sims
E03 3 61D 1	C	ring	720		sem
E03 4 76A 3	C	ring	720	melting zone on the left	sem sims

summary of extended impacts A
as of 6/23/95

impact name		type of impact	size	comments	analysis to date
C02 2 10B 1		ring	650		sem sims
E03 3 71A 1	C	ring	640		none
E03 3 71B 1	C	ring	640	melting zone in lower left	sem
E08 6 7A 7		ring	560	cr-like damage, bottom	none
E08 5 9B 18		ring	504	overlaps erosion	none
E08 6 5B 11		ring	504		none
E08 6 5D 10		ring	504		none
E03 3 62B 2		ring	500		sem
C02 2 12D 3	C	ring	480	long tailed melting zone	sem sims
E08 1 2A 14		ring	448		none
E08 4 1C 6		ring	448	below BED	sem sims
E08 6 2C 8		ring	448		none
E08 5 16B 4		ring	420	below erosion	none
E08 4 3B 3		ring	392	below BED	none
E08 6 7B 9		ring	392		none
E03 3 63D 1		ring	360		none
E08 3 13D 7		ring	360	spray, below erosion	sem sims

summary of extended impacts A
as of 6/23/95

impact name		type of impact	size	comments	analysis to date
E08 5 13B 4		ring	360	spray in middle of ring	sem sims
E08 5 4A 6		ring	360	spray at bottom	none
E08 6 13D 18		ring	360	below errosion	none
E08 2 13D 14		ring	336		none
E08 5 6B 17		ring	336		none
E08 6 16B 5		ring	336	very faint	none
E08 5 20C 3		ring	280	blue ellipt. discolor.	none
E08 6 7C 4		ring	280		none
E08 2 16A 17		ring	224		none
E08 3 10C 11		ring	224		none
E08 4 14D 7		ring	224		none
E08 5 1D 12		ring	224		none
E08 5 6D 21		ring	224	concentric rings?	none
C02 1 14C 2		spiderweb	2000	very promising	sem sims
E03 1 39C 1		spiderweb	1600		sem sims
C02 1 20D 2		spiderweb	1500		sem sims
E03 4 56D 4	C	spiderweb	1400		sem sims
E03 2 37A 5		spiderweb	1300		none

summary of extended impacts A
as of 6/23/95

impact name		type of impact	size	comments	analysis to date
C02 1 8A 2		spiderweb	1200		sem sims
C02 2 8D 1		spiderweb	1200		sem sims
C02 2 4B 1		spiderweb	1100		sem sims
C02 1 3B 2		spiderweb	1000		sem sims
C02 2 11A 2		spiderweb	1000		sem sims
C02 2 13B 1		spiderweb	1000	near the edge	sem sims
E03 1 22D 2		spiderweb	1000		sem sims
E03 3 52D 4		spiderweb	1000	material seen in sem	sem sims
E03 4 67D 1		spiderweb	1000		sem sims
E03 2 11A 1	C	spiderweb	960		sem sims
E03 2 19C 1		spiderweb	840		sem sims
E08 3 10B 13		spiderweb	840		sem sims
C02 1 3C 1		spiderweb	800	or EXT.IMPB?	sem sims
C02 2 14B 1		spiderweb	800	250x800, lots of contamination around it.	sem sims
E03 2 37C 2		spiderweb	800		sem sims
E08 3 7C 17		spiderweb	784		none
E03 1 2D 2	C	spiderweb	720		sem sims

summary of extended impacts A
as of 6/23/95

impact name		type of impact	size	comments	analysis to date
E03 1 33C 1	C	spiderweb	720		sem
E08 1 14C 11		spiderweb	672		sem sims
C02 2 5A 1		spiderweb	650		sem sims
E03 1 6D 2		spiderweb	640		sem sims
E08 4 13B 4		spiderweb	616		none
E08 6 5D 15		spiderweb	616		none
E03 2 12A 3		spiderweb	600	large classical mat!!	sem sims
E03 4 47B 2		spiderweb	600	near the edge	none
E08 4 2D 15		spiderweb	600		none
E08 2 7C 7		spiderweb	560		sem
E08 2 7C 8		spiderweb	560	large scatter of associated impacts; no residue apparent	sem
E08 4 13B 5		spiderweb	560		sem sims
E08 5 12A 2		spiderweb	560		none
E08 6 17C 15		spiderweb	560		none
E08 6 5C 4		spiderweb	560		none
E08 6 5C 6		spiderweb	560		none
E08 6 6C 6		spiderweb	560		none

summary of extended impacts A
as of 6/23/95

impact name		type of impact	size	comments	analysis to date
C02 2 16A 1		spiderweb	550		sem sims
E08 2 19A 3		spiderweb	540		none
E08 2 15D 1		spiderweb	504		none
E08 3 11A 16		spiderweb	504		none
E08 4 15D 7		spiderweb	504	deep and crater-like	none
E08 4 19C 4		spiderweb	504		none
E08 5 17D 7		spiderweb	504		sem
E08 6 13B 2		spiderweb	504		none
E08 6 2C 11		spiderweb	504		none
E08 2 19A 2		spiderweb	480		none
E08 3 11A 21		spiderweb	448		none
E08 3 19C 15		spiderweb	448	overlaps BED	sem sims
E08 4 5A 9		spiderweb	448		none
E08 5 11A 17		spiderweb	448		none
E08 5 17D 11		spiderweb	448		sem
E08 5 19D 10		spiderweb	448		none
E08 6 13A 8		spiderweb	448		none
E08 6 17A 1		spiderweb	448		none
E08 6 1D 6		spiderweb	448		none
E08 6 6C 7		spiderweb	448		sem sims

summary of extended impacts A
as of 6/23/95

impact name	type of impact	size	comments	analysis to date
E03 2 28A 6	spiderweb	420		none
E08 4 20D 8	spiderweb	400		none
E08 5 17D 4	spiderweb	392	faint, below erosion	sem
E08 5 19D 8	spiderweb	392		none
E08 5 7B 2	spiderweb	392		none
E08 6 13A 4	spiderweb	392		none
E08 6 17C 5	spiderweb	392		none
E08 6 17C 8	spiderweb	392		none
E08 6 17C 9	spiderweb	392		none
E08 6 17C 12	spiderweb	392		none
E08 6 2C 16	spiderweb	392		none
E08 3 13C 16	spiderweb	360	below erosion	none
E08 6 18A 13	spiderweb	360	below erosion	none
E08 4 1C 18	spiderweb	336	below BED	sem sims
E08 5 17A 9	spiderweb	336		none
E08 5 17D 9	spiderweb	336		sem
E08 5 7B 3	spiderweb	336		none
E08 5 7C 14	spiderweb	336		none
E08 6 13A 2	spiderweb	336		none
E08 6 17C 10	spiderweb	336		none

summary of extended impacts A
as of 6/23/95

impact name	type of impact	size	comments	analysis to date
E08 6 7A 8	spiderweb	336		none
E08 6 7A 11	spiderweb	336		none
E08 1 5A 7	spiderweb	300		none
E08 2 15B 16	spiderweb	300		none
E08 3 18D 25	spiderweb	300		none
E08 3 5C 12	spiderweb	300	below erosion	none
E08 5 14B 14	spiderweb	300	below erosion	none
E08 1 2C 6	spiderweb	280		none
E08 1 9C 9	spiderweb	280		none
E08 3 19A 2	spiderweb	280		none
E08 4 10A 1	spiderweb	280		none
E08 4 15D 6	spiderweb	280	below erosion	none
E08 4 15D 16	spiderweb	280		none
E08 4 3A 3	spiderweb	280		none
E08 5 18D 18	spiderweb	280	below erosion	none
E08 5 18D 20	spiderweb	280		none
E08 5 19D 12	spiderweb	280		none
E08 5 19D 14	spiderweb	280		none
E08 6 16C 15	spiderweb	280		none
E08 6 16D 11	spiderweb	280		none
E08 6 17B 12	spiderweb	280		none

summary of extended impacts A
as of 6/23/95

impact name		type of impact	size	comments	analysis to date
E08 6 1D 7		spiderweb	280		none
E08 6 6D 4		spiderweb	280	surr by spray	none
E08 6 7A 5		spiderweb	280		none
E08 6 7B 1		spiderweb	280		none
E08 6 8B 1		spiderweb	280		none
E08 1 3D 17		spiderweb	250		none
E08 2 12B 5		spiderweb	250		none
E08 2 12B 13		spiderweb	250		none
E08 2 19A 12		spiderweb	240		none
E08 3 12C 19		spiderweb	240		none
E08 3 13B 17		spiderweb	240	below erosion	none
E08 3 1A 9		spiderweb	240	overlapping erosion	none
E08 3 5B 1		spiderweb	240		none
E08 3 5B 2		spiderweb	240		none
E08 3 5C 18		spiderweb	240		none
E08 4 12B 3		spiderweb	240		none
E08 5 3C 23		spiderweb	240		none
E08 6 13D 14		spiderweb	240		none
E08 6 15A 8		spiderweb	240		none
E08 1 12A 6		spiderweb	224		none

summary of extended impacts A
as of 6/23/95

impact name		type of impact	size	comments	analysis to date
E08 1 19D 10		spiderweb	224		none
E08 1 9A 2		spiderweb	224		none
E08 2 11C 5		spiderweb	224		sem sims
E08 2 7B 5		spiderweb	224		sem sims
E08 3 10C 8		spiderweb	224		none
E08 3 4C 14		spiderweb	224		none
E08 4 15D 9		spiderweb	224	below erosion, ring too	none
E08 4 15D 13		spiderweb	224		none
E08 5 11A 13		spiderweb	224		none
E08 5 17A 6		spiderweb	224	below erosion	none
E08 5 17A 10		spiderweb	224		none
E08 5 19B 4		spiderweb	224		none
E08 5 19D 4		spiderweb	224	below erosion	none
E08 5 7B 4		spiderweb	224		none
E08 5 7C 9		spiderweb	224		none
E08 5 7C 13		spiderweb	224	below erosion	none
E08 5 9D 5		spiderweb	224		none
E08 5 9D 10		spiderweb	224	below erosion	none
E08 6 7A 4		spiderweb	224		none
E08 6 7C 5		spiderweb	224		none

summary of extended impacts A
as of 6/23/95

impact name		type of impact	size	comments	analysis to date
E08 1 5D 29		spiderweb	180		none
E08 5 5B 3		spiderweb	180	below erosion	none
E08 4 18B 2		spiderweb	175		none
E08 5 17A 15		spiderweb	170	faint, below erosion	none
E08 1 19D 11		spiderweb	168		none
E08 4 19A 5		spiderweb	168		none
E08 4 19C 15		spiderweb	168	below erosion	none
E08 5 11A 15		spiderweb	168		none
E08 5 1D		spiderweb	168		none
E08 6 16C 13		spiderweb	168		none
E08 6 8A 1		spiderweb	168	at edge	none
E08 5 19D 2		spiderweb	160		none
E08 5 12A 3		spiderweb	140		none
E08 4 7A 11		spiderweb	120		none
E08 6 20A 1		spiderweb	120	sp extends 720µ out	none
E08 5 18D 7		spiderweb	112		none
E08 1 3D 18		spiderweb	400?	maybe just scratches	none

summary of extended impacts A
as of 6/23/95

impact name		type of impact	size	comments	analysis to date
E08 2 1B 3		spray	5600	out from edge	none
E03 1 15A 1	C	spray	2400	not so dense	sem
E08 2 18B 2		spray	1680	more extends down	none
E08 2 16A 3		spray	1568		sem sims
E08 4 1A 6		spray	1512		none
C02 2 12A 1	C	spray	1200		sem sims
E03 4 59A 5		spray	1200		sem sims
E08 2 6B 1		spray	1200		none
E08 4 20B 11		spray	1200	very visible	sem
E08 2 9B 4		spray	1120		none
E08 6 6C 4		spray	1064		none
E08 2 6A 12		spray	900		none
E08 4 7C 3		spray	900	in semicircle	sem
E08 5 3C 16		spray	900	long and narrow	none
E08 5 9D 9		spray	896		none
E08 2 20A 12		spray	840		none
E08 6 8C 2		spray	840		none
E03 4 75D 1	C	spray	800		sem sims
E03 4 77A 2		spray	800		sem sims
E08 3 7D 2		spray	784		none

summary of extended impacts A
as of 6/23/95

impact name		type of impact	size	comments	analysis to date
E08 4 14D 8		spray	784	visible discolor. with naked eye	none
E08 6 17C 7		spray	784		none
E08 6 6D 3		spray	728	crlike damage incenter	none
E08 2 15D 2		spray	672		none
E08 2 17A 3		spray	672		sem sims
E08 3 11A 14		spray	672		none
E08 3 11A 18		spray	672		none
E08 3 20D 16		spray	672	is around crater	none
E08 6 6C 8		spray	672	extensive, in a sunburst formation (from edge) other individual sprays may be there, but difficult to tell because of erosion in the area.	none
E08 6 8A 2		spray	672		none

summary of extended impacts A
as of 6/23/95

impact name		type of impact	size	comments	analysis to date
E03 1 15B 2	C	spray	640	close to the edge	sem
E08 6 6D 8		spray	616	cr in center, sp surr.	none
E08 2 10B 15		spray	600		none
E08 3 6C 11		spray	600		none
E08 5 14B 7		spray	600	strange shape	none
E08 6 20C 19		spray	600		none
E08 6 20D 25		spray	600	good center	none
E08 1 14B 10		spray	560		none
E08 2 17C 16		spray	560	hit the very edge: there is a debris trail that extends for another 1960 μm	sem
E08 3 11A 12		spray	560		none
E08 3 19D 9		spray	560		none
E08 3 7C 11		spray	560		none
E08 4 16C 10		spray	560		none
E08 5 11A 10		spray	560	w/ 110μ crater	none
E08 5 19D 9		spray	560		none
E08 6 13B 5		spray	560		none

summary of extended impacts A
as of 6/23/95

impact name		type of impact	size	comments	analysis to date
E08 6 5D 8		spray	560		sem sims
E03 3 62C 4		spray	550		none
E08 5 16B 19		spray	540	below erosion	sem
E08 1 12B 12		spray	504		none
E08 2 18C 23		spray	504		none
E08 3 11A 11		spray	504		none
E08 5 11A 6		spray	504		none
E08 6 1D 5		spray	504	below erosion	none
E08 6 7C 9		spray	504	crater-like center	none
E03 2 38C 5		spray	500		sem sims
E08 4 7D 7		spray	500		none
E03 4 75B 1	C	spray	480	dense, like a ring	sem
E08 4 2B 9		spray	480	good center	none
E08 4 2C 14		spray	480		none
E08 5 2D 13		spray	480		none
E08 6 19D 8		spray	480	fainter sp extends	none
E08 3 11B 10		spray	448		none
E08 4 14B 9		spray	448		none

summary of extended impacts A
as of 6/23/95

impact name		type of impact	size	comments	analysis to date
E08 6 6B 5		spray	448		none
E08 6 8A 5		spray	448		none
E08 6 7B 10		spray	440		none
E08 2 15B 15		spray	420		none
E08 2 19A 5		spray	420		none
E08 2 6D 23		spray	420		none
E08 5 11C 21		spray	420		none
E08 5 2D 14		spray	420		none
E08 6 9C 3		spray	420		none
E03 1 30B 2		spray	400	has a tail (800um)	sem sims
E08 1 4A 19		spray	400		none
E08 1 12B 8		spray	392	extending from edge	none
E08 1 2C 9		spray	392	large brown discoloration erosion?	none
E08 1 2C 13		spray	392	brown ED in ring	none
E08 1 5A 11		spray	392	has some debris below	none
E08 2 8D 10		spray	392		none

summary of extended impacts A
as of 6/23/95

impact name	type of impact	size	comments	analysis to date
E08 3 10C 17	spray	392		none
E08 4 18D 3	spray	392		none
E08 6 16C 11	spray	392	overlaps erosion	none
E08 6 17B 6	spray	392		none
E08 6 17C 13	spray	392		none
E08 6 1B 2	spray	392		none
E08 6 6D 10	spray	392		none
E08 6 6D 12	spray	392	below erosion	none
E08 6 8D 3	spray	392		none
E03 2 9A	spray	360		none
E08 3 3A 6	spray	360	below erosion elipse	none
E08 6 10B 1	spray	360		none
E08 1 13D 14	spray	336		none
E08 1 15A 18	spray	336	overlies bl. ellipt. disc.	none
E08 1 15B 2	spray	336		none
E08 1 5A 19	spray	336	surrounded by brownED	none
E08 2 8D 12	spray	336		none
E08 3 19D 10	spray	336		none

summary of extended impacts A
as of 6/23/95

impact name	type of impact	size	comments	analysis to date
E08 4 10A 9	spray	336		none
E08 4 11A 3	spray	336		none
E08 4 11D 1	spray	336		none
E08 4 11D 8	spray	336		none
E08 4 15A 3	spray	336		none
E08 4 19C 6	spray	336	overlaps ri and erosion	none
E08 4 5A 18	spray	336		none
E08 5 11A 19	spray	336		none
E08 5 12A 6	spray	336		none
E08 5 17A 12	spray	336	below erosion	none
E08 6 17B 2	spray	336		none
E08 6 2C 18	spray	336		none
E08 6 5A 5	spray	336		none
E08 6 5A 7	spray	336		none
E08 6 7B 6	spray	336	crater-like center	none
E08 6 7C 8	spray	336		none
E03 2 12D 1	spray	300	strange-shaped, dense	sem

summary of extended impacts A
as of 6/23/95

impact name		type of impact	size	comments	analysis to date
E08 3 13C 5		spray	300	below erosion	none
E08 3 18D 23		spray	300		none
E08 3 5B 6		spray	300	below erosion elipse	none
E08 3 6C 13		spray	300		none
E08 5 13C 18		spray	300	strange shape	none
E08 5 16C 10		spray	300		none
E08 5 2D 6		spray	300		none
E08 5 2D 16		spray	300		none
E08 5 3C 15		spray	300		none
E08 5 8C 11		spray	300		none
E08 6 15A 20		spray	300		none
E08 6 20A 17		spray	300	below erosion	none
E08 6 20B 5		spray	300	below erosion	none
E08 6 5C 5		spray	300		none
E08 3 19A 3		spray	296	almost crater like	none
E08 1 14A 11		spray	280		none
E08 1 1C 16		spray	280		none
E08 1 1C 21		spray	280		none
E08 1 1C 23		spray	280		none

summary of extended impacts A
as of 6/23/95

impact name		type of impact	size	comments	analysis to date
E08 1 2C 12		spray	280		none
E08 1 2C 14		spray	280		none
E08 1 2C 15		spray	280		none
E08 1 6B 14		spray	280	debris fans out for 280 µm	none
E08 2 16A 7		spray	280		none
E08 2 3A 2		spray	280		none
E08 2 9B 11		spray	280		none
E08 3 10C 14		spray	280		none
E08 3 10D 1		spray	280		none
E08 3 1A 1		spray	280		none
E08 3 20A 4		spray	280		none
E08 4 10A 3		spray	280	below BED	none
E08 4 15A 13		spray	280		none
E08 4 15D 15		spray	280	below erosion	none
E08 4 3D 8		spray	280		none
E08 5 11A 2		spray	280	below erosion	none
E08 5 12A 4		spray	280		none
E08 5 19A 6		spray	280		none
E08 5 19C 5		spray	280		none

summary of extended impacts A
as of 6/23/95

impact name	type of impact	size	comments	analysis to date
E08 5 8D 2	spray	280	below erosion	none
E08 5 9B 17	spray	280	overlaps erosion	sem sims
E08 5 9D 2	spray	280	below erosion	none
E08 6 16D 3	spray	280		none
E08 6 17A 5	spray	280		none
E08 6 8C 6	spray	280		none
E08 5 12D 11	spray	252		none
E08 1 3D 16	spray	250		none
E08 2 12B 3	spray	250		none
E08 2 6C 16	spray	240		none
E08 3 1D 19	spray	240		none
E08 3 3D 5	spray	240		none
E08 3 5B 5	spray	240	below erosion elipse	none
E08 3 5B 7	spray	240	below erosion, faint	none
E08 3 5B 9	spray	240		none
E08 3 5B 17	spray	240		none
E08 3 6B 15	spray	240		none
E08 5 13C 6	spray	240	below erosion	none

summary of extended impacts A
as of 6/23/95

impact name	type of impact	size	comments	analysis to date
E08 5 13C 17	spray	240	strange shape	none
E08 6 10B 2	spray	240		none
E08 6 10D 16	spray	240		none
E08 6 14C 9	spray	240	faint &below errosion	none
E08 1 5A 15	spray	235		none
E08 1 12A 18	spray	224		none
E08 1 12C 11	spray	224	BED below SP	none
E08 1 4C 35	spray	224		none
E08 1 6B 1	spray	224		none
E08 2 16A 5	spray	224		none
E08 2 16A 10	spray	224	extends towards corner #4	none
E08 2 18C 11	spray	224	overlaps BED	none
E08 2 18D 11	spray	224		none
E08 2 3A 1	spray	224		none
E08 2 8D 13	spray	224		none
E08 3 11B 2	spray	224		none
E08 3 19C 13	spray	224	overlaps BED	none
E08 3 4A 2	spray	224		none
E08 4 10A 10	spray	224		none

summary of extended impacts A
as of 6/23/95

impact name	type of impact	size	comments	analysis to date
E08 4 10A 19	spray	224		none
E08 4 10A 22	spray	224	below BED	none
E08 4 11B 3	spray	224		none
E08 4 14D 11	spray	224		none
E08 4 15A 6	spray	224		none
E08 5 12D 8	spray	224		none
E08 5 6C 8	spray	224		sem sims
E08 5 7C 6	spray	224	below erosion	none
E08 6 13B 6	spray	224		none
E08 6 1A 8	spray	224		none
E08 4 1B 2	spray	220		none
E08 4 7A 10	spray	210	below erosion	none
E08 4 7C 11	spray	210		none
E08 5 5B 1	spray	210	below erosion	none
E08 3 4C 16	spray	196		none
E08 4 15A 10	spray	196	below erosion	none
E03 2 28A 4	spray	180	very dense spray	none
E08 2 19A 13	spray	180		none
E08 3 6B 4	spray	180		none
E08 4 6A 20	spray	180	dark, below erosion	none

summary of extended impacts A
as of 6/23/95

impact name	type of impact	size	comments	analysis to date
E08 5 5B 15	spray	180	below erosion	none
E08 6 19D 15	spray	180	below erosion	none
E08 6 20C 18	spray	180		none
E08 1 12B 5	spray	168		none
E08 2 13D 13	spray	168		none
E08 2 17C 9	spray	168		none
E08 2 17D 10	spray	168		sem
E08 3 10D 18	spray	168		none
E08 3 15B 18	spray	168		none
E08 3 15C 22	spray	168	also a number of craters in the area - interesting!	none
E08 3 4A 1	spray	168		none
E08 4 10A 4	spray	168		none
E08 4 14A 3	spray	168		none
E08 4 15A 4	spray	168		none
E08 4 15D 11	spray	168	below erosion	none
E08 4 3A 2	spray	168		none
E08 4 4C 3	spray	168		none

summary of extended impacts A
as of 6/23/95

impact name	type of impact	size	comments	analysis to date
E08 4 5A 5	spray	168	below BED	none
E08 4 5B 1	spray	168		none
E08 5 12D 12	spray	168		none
E08 5 17B 8	spray	168		none
E08 5 18D 14	spray	168		none
E08 5 6C 10	spray	168	blue ellipt. discolor.	sem
E08 5 8B 1	spray	168		none
E08 6 17C 14	spray	168		none
E08 6 1A 6	spray	168		none
E08 6 6A 1	spray	168		none
E08 6 7C 2	spray	168		none
E08 4 6B 2	spray	150	below erosion ellipse	none
E08 4 9B 1	spray	140		none
E08 6 1A 1	spray	140		none
E08 1 5A 13	spray	130		none
E08 3 18D 17	spray	120	or bottom of ring??	none
E08 5 5D 20	spray	120		none
E08 4 16D 10	spray	112		none

summary of extended impacts A
as of 6/23/95

impact name	type of impact	size	comments	analysis to date
E08 4 19A 4	spray	112		none
E08 4 5B 3	spray	112		none
E08 5 10B 2	spray	112		sem sims
E08 5 17A 13	spray	112		none
E08 5 18D 9	spray	112		none
E08 5 19A 2	spray	112	below erosion	none
E08 6 12C 12	spray	112		none
E08 6 6D 2	spray	112		none
E08 4 15A 8	spray	110	below erosion	none
E08 3 2C 11	spray	75		none
E08 1 3D 15	spray	200?		none
E08 5 16D 15	spray	600+	extensive, fainter out to approx 6000μ	none
E08 6 10C 1	spray	900?		none
E08 6 6D 7	spray	840?		none
E08 6 7A 10	spray	168?	cr-like spray	none

crater survey summary as of 4/11/92

wafer	mag	area scanned	# of craters	density	sigma(%)
E08-3-15A	300	1cm^2	55	55	13.48
E08-3-2B	300	1 cm^2	66	66	12.31
E08-3-9C	300	1 cm^2	53	53	13.74
E08-4-11D	300	1 cm^2	41	41	15.62
E08-4-14C	300	1 cm^2	61	61	12.8
E08-4-4D	300	1cm^2	85	85	10.85
E08-4-4D1000.2	1000	1cm^2	211	211	6.88
E08-4-4D2	300	1cm^2	67	67	12.22
E08-4-8B	300	1 cm^2	73	73	11.7
E08-6-3A	300	1 cm^2	66	66	12.31
E08-6-3A1000	1000	0.7272cm^2	49	67.4	14.29
E08-6-3A300f	300	2.1 cm^2	40	19	15.81

SIMS CHEMICAL ANALYSIS OF EXTENDED IMPACT FEATURES FROM THE TRAILING EDGE PORTION OF EXPERIMENT AO187-2

Sachiko Amari, John Foote, Charles Simon,
Pat Swan, Robert M. Walker, Ernst Zinner
McDonnell Center for the Space Sciences
Washington University
One Brookings Drive
Saint Louis MO 63130-4899 USA
Phone: 314-889-6257, Fax: 314-889-6219

Elmar K. Jessberger, Gundolf Lange, Frank Stadermann
Max-Planck-Institut für Kernphysik
Postfach 103980
6900 Heidelberg, Germany

SUMMARY

One hundred capture cells from the trailing edge, which had lost their cover foils during flight, were optically scanned for extended impact features caused by high velocity projectiles impinging on the cells while the foils were still intact. Of 53 candidates, 24 impacts were analyzed by secondary ion mass spectrometry for the chemical composition of deposits. Projectile material was found in all impacts, and at least 75% of them appear to be caused by interplanetary dust particles. Elemental ratios are fractionated, with refractory elements enriched in the impacts relative to interplanetary dust particles collected in the stratosphere. Although this could be due to systematic differences in the compositions, a more likely explanation is volatility fractionation during the impact process.

INTRODUCTION

The main scientific objective of LDEF experiment AO187-2 was the collection of interplanetary dust material in space and its elemental and isotopic analysis in the laboratory. Although interplanetary dust collected in the upper atmosphere has been available for analysis in terrestrial laboratories for more than a decade (e.g., refs. 1, 2), the stratospheric collection undoubtedly is biased since not all extraterrestrial dust particles entering the Earth's atmosphere are collected. For example, cometary dust particles have, on average, a higher velocity and are therefore expected to have a much smaller survival probability of atmospheric entry than dust grains originating from asteroids (refs. 3, 4). In order to obtain an unbiased sample of interplanetary dust it is necessary to collect this material in space. LDEF provided an unprecedented opportunity for this purpose, combining large collecting areas with long exposure times.

A fundamental problem for the collection of interplanetary dust material is the high relative velocity of dust grains (10-15 km/sec). At these high velocities a major fraction of projectile material is lost upon impact with most collection surfaces. A viable compromise is to forgo the collection of solid dust grains

503

or fragments thereof and to concentrate on the collection of their atoms in capture cells. LDEF carried several capture cell experiments (AO023, AO138-2); the principle of AO187-2 is shown in Figure 1. A target plate is covered by a thin foil separated by a small distance. A high velocity dust grain of sufficient size penetrates the foil and normally is disrupted in the process, spreading out into a shower of debris. This shower impacts the target plate, being further disrupted, melted and vaporized. The projectile material ejected from the impact zone is collected on the backside of the foil and then analyzed.
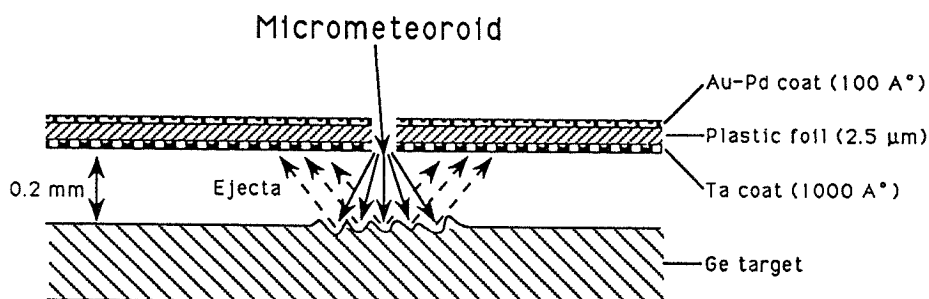
Figure 1. Principle of capture cell of experiment AO187-2.

A series of simulation experiments on laboratory dust accelerators proved this concept to be viable (refs. 5-7): projectile material could indeed be collected on the surface of the target plate and the backside of the foil and its elemental and isotopic composition measured. Since the collected material exists as a thin surface deposit, secondary ion mass spectrometry (SIMS) with its extremely high surface sensitivity proved to be the best-suited analysis technique. In fact, since one of the main objectives of the experiment was the isotopic measurement of dust material, AO187-2 was originally conceived and optimized for SIMS analysis. The choice of materials was largely determined by the requirements for extreme purity and high ion yields for SIMS analysis.

EXPERIMENT DESCRIPTION AND PRELIMINARY ASSESSMENT

LDEF experiment AO187-2 consisted of 237 capture cells, each 8.6×9.4 cm in size. A capture cell in turn consisted of four polished high purity germanium plates, $42 \times 39 \times 0.5$ mm, covered with a plastic foil separated from the Ge plate by 200μm. The Ge plates were glued to an Al base plate, the 2.5 μm thick mylar cover foil was coated with 1300 Å of Ta on the backside and 100 Å of Au-Pd on the front side. Ta was chosen to optimize the SIMS analysis of deposited projectile material; Au-Pd was chosen to protect the foil from erosion by atomic oxygen in the residual atmosphere impinging on the leading edge of LDEF (refs. 8, 9).

The capture cells occupied locations on three different trays. A full tray, E8, on the leading edge contained 120 cells, 77 cells were mounted on tray E3 and 40 took up a third of tray C2, both on the trailing edge. By having capture cells on both the leading and the trailing edge, the experiment was expected to obtain information on both interplanetary dust and man-made space debris in low Earth orbit.

After the return of LDEF it was found that all capture cells on the leading edge tray E8 had lost their plastic-metal foils and only 12 cells on the trailing edge had retained them, 11 on tray E3 and one on tray C2. Four capture cells from tray E8 and 5 cells without foil from tray E3 were shipped to Messerschmitt-Bölkow-Blohm in Germany; the rest of the cells went to Washington University. At present we do not know why the foils failed or when this happened. The fact that 12 intact cells were found on the trailing

edge indicates that the failure mechanism probably was not the same for the two locations. Atomic oxygen erosion starting from impact holes or spots with damages in the protective metal coating is a likely cause for the complete failure of the cells on the leading edge of tray E8. The capture cells on the trailing edge, however, never were exposed to an atomic oxygen flux. A combination of embrittlement by solar UV and stress failure under thermal cycling is a possible cause but this hypothesis has to be substantiated by future tests. If we assume that the failure of foils on the trailing edge is an exponential function of time, 67% of the cells would have been still intact after one year, the nominal deployment duration for LDEF.

Preliminary optical microscope examination of cells from the trailing edge that had lost their cover foils (bare cells) showed numerous "extended impact features" as well as typical hypervelocity impact craters produced by direct hits. The extended impact features resembled laboratory simulation impacts produced by projectile material that had penetrated plastic foils and had suffered disruption. Apparently, the extended impact features found on the bare LDEF cells were produced by high velocity impacts onto the cells while the foils were still intact. Since prior simulation studies (ref. 7) had shown that extended impacts on the Ge plates contained sufficient projectile material for chemical and isotopic analysis by SIMS

Figure 2. Lateral elemental profiles across plastic foil and Ge wafer of the same simulation impact.

(Fig. 2), we first concentrated our analysis effort on the extended impacts found in the bare LDEF capture cells from the trailing edge (trays E3 and C2). These were the best candidates to contain impacts of interplanetary dust particles with a minimum contribution from orbital debris. Furthermore, foil survival on 10% of trailing edge cells compared to none on the leading edge indicated that even foils that failed lasted, on average, longer on the trailing than the leading edge.

All 100 bare capture cells from E3 and C2 in our possession were optically scanned for impact features. During the scanning we developed criteria for the classification of these impacts and for the selection of candidates for SIMS analysis. All selected candidates were further documented in a scanning electron microscope (SEM). To date, a subset of these candidates has been analyzed by SIMS for the chemical composition of deposited material.

OPTICAL AND SEM CHARACTERIZATION

All bare cells in our possession from the trailing edge, 61 from tray E3 and 39 from tray C2, were scanned under oblique illumination in an optical stereo microscope with a 12× objective and 20× eyepiece. The Al plates with the Ge wafers were mounted on a scanning stage whose position could be read with an accuracy of 50 μm. The wafers were scanned a row (of 6.0 mm width) at a time. Recorded were the locations of impact features and their sizes and other interesting properties. Among the impacts we distinguished between "craters" and "extended impacts." Since Ge is very brittle, craters produced by direct hits (i.e. without penetration of a foil) are not likely to contain much residual material from the projectile and this expectation was confirmed by subsequent analysis. Figure 3 shows a SEM image of a crater.

The extended impacts are the most interesting since they are expected to contain projectile material. They range from 200 μm to 4000 μm in diameter and were divided into two categories, A and B. Category A comprises larger impacts that are expected to contain deposits and are high priority candidates for SIMS analysis. Category B impacts are smaller and will be studied last. Features that could not be recognized with certainty as extended impacts in the optical microscope were classified as "possible extended impacts (Category A or B)," and were examined in more detail in the SEM.

Figure 3. Crater produced by hypervelocity impact onto Ge wafer without cover foil.

Extended impacts of category A and B were further classified into four sub-categories according to their morphology.

1) Craters surrounded by deposits (CD).
2) Ring-shaped features (RI).
3) Sprays (SP).
4) Spider webs (SW).

Figure 4 shows SEM micrographs of one of each morphology. The more detailed SEM images revealed that in many cases an extended impact showed features of different categories (e.g. a crater surrounded by deposits also had spider web features).

Scanning in the SEM was performed with a twofold purpose:

a) To check all features that had been classified as "possible extended impacts" during the initial optical scanning to determine which of them are true "extended impacts."
b) To document in detail all extended impacts to be selected for SIMS analysis.

Table 1 gives a summary of the results of the optical scanning. So far, 98 of 157 possible extended impacts have been examined in the SEM and five of them have been reclassified as extended impacts (2 CD, 3 RI).

506

Figure 4. Morphologies of extended impacts: Craters surrounded by deposits (upper left), ring (upper right), spray (lower left), and spider web (lower right).

Table 1. Classification of impacts on bare capture cells from the trailing edge

Extended Impacts		CD	RI	SP	SW	Total
	A	14	8	8	23	53
	B	5	42	94	14	155
Possible Extended Impacts	A					157
	B					177
Craters						203

During the SEM documentation of extended impacts energy dispersive x-ray (EDX) spectra were obtained in most cases, especially if fragments were observed in the area of the impact. However, fragments usually turned out to be pieces of the Ta coating of the mylar foil or other apparent contaminants. Generally it was not possible to detect any elements besides Ge. An exception was Si which is present in quantities detectable by EDX on all Ge wafers

507

from the leading and trailing edge. The Si concentrations on the wafers are non-uniform, being highest on the edges and lowest in the middle of the Ge plates. The most likely cause for this ubiquitous Si background is outgassing or migration of the RTV used to bond the Ge onto the Al substrate (in spite of the space rating of this material). This unfortunate circumstance deprived us (with a few exceptions) of the opportunity to measure one of the most important cosmochemical elements in the projectile deposits.

A comparison of the extended impact features on Ge from the trailing edge and simulation impacts produced on the same foil-target assembly in the Munich plasma dust accelerator (refs. 10, 11) at velocities between 3 and 8 km/sec shows significant differences. The LDEF impacts are, on average, larger and much more irregular. The simulation impacts usually are spider webs with a high degree of rotational symmetry or ring-shaped features with typical diameters of 100-200µm. There are two possible explanations for the large irregular impact features found on the Ge plates from the trailing edge. One is that many impacts were produced by projectiles that hit the capture cells at oblique angles. The second is that the foil had already been damaged and some of it had curled up when the impact occurred, leading to a much more complex foil-target geometry than for the simulation impacts, which were produced at normal incidence.

SIMS ANALYSIS OF EXTENDED IMPACTS

For SIMS analysis the Ge wafers were cut into smaller pieces containing extended impacts of interest. This was done by a newly developed laser cutting technique, which avoids any of the contamination incurred by sawing. A CW YAG laser beam of 1.06 µm wavelength was focussed onto the rough backside of the Ge wafer (this side has a higher absorption at this wavelength than the polished front side). At a power of 50 W a short scan across the wafer at a speed of 5 cm/sec was sufficient to cause a break along the scanned line most of the time. Sometimes the wafers broke along other defects or along crystal boundaries; however, in all such cases intact pieces of appropriate size could be obtained for ion probe analysis.

To date 24 of a total 53 extended impacts of category A have been analyzed by SIMS for the chemical composition of projectile deposits. All measurements were made on the Washington University ion microprobe, a modified CAMECA IMS 3f instrument. For chemical analysis we obtained lateral scanning profiles across the impact features. For this purpose at each analysis point an O^- primary ion beam of 1-2 nA current was rastered over an area of 40µm×40µm. As the primary ion beam sputtered away the surface of the analyzed sample layer by layer, positive secondary ions selected from the central portion of the rastered area by a beam aperture were mass analyzed in a double focussing magnetic mass spectrometer and counted by an electron multiplier detection system.

Multi-element depth profiles are obtained by cycling the mass spectrometer through a set of isotopic masses of the selected elements. After analysis of a given area consisting of 40 cycles the sample is stepped (by 40 or 50 µm) to the next area. Fig. 5a shows a SEM micrograph of an extended impact after two step-scanning analyses were made on this sample. The individual depth profiles were integrated over cycles 4 to 40 to obtain lateral profiles in the form of the integrated secondary ion intensity as a function of lateral distance. The first three cycles were not included in order to reduce the effect of surface contamination and because a variety of artifacts are encountered during sputtering of the very surface.

508

Ion signals associated with material from the impacts could be detected in all 24 analyzed impact areas but large variations were observed between individual impacts. For example, the ratio of the maximum $^{24}Mg^+$ signal to the $^{72}Ge^+$ signal for an individual lateral intensity profile varies over almost 5 orders of magnitude.

The ideal case is shown by the profile of Fig. 5b, which corresponds to the top scan in Fig. 5a. This scan has well defined maxima for all the isotopic masses measured except for $^{72}Ge^+$. It is one of the few cases where the $^{28}Si^+$ also displays a clear maximum above background; the latter, however, is much higher for this element than for all the others (since the yield of positive secondary ions is less for Si than for Mg, Al, Ca and Fe; this discrepancy in the background is actually much larger than is indicated by the plot of Fig. 5b). The profile across impact EO3-2-19C-1 is also one of the few which gives a clear signal for Ni$^+$ at mass 60. The reason is that the signals associated with impact deposits are relatively high compared to the Si background. In most other cases, these signals are much lower so that the molecular interference from $^{28}SiO_2^+$ dominates at mass 60.

In order to obtain elemental abundances, the ion yields of different elements as well as the isotopic abundances have to be taken into account. Table 2 gives sensitivity factors S relative to Si so that

$$\frac{C_{El}}{C_{Si}} = \frac{I_{El}}{I_{Si}} / S_{El/Si}$$

where C are the atomic concentrations and I are the secondary ion signals (corrected for isotopic abundances) for the element of interest and the standard element Si. The sensitivity factors were determined from measurements on four different glasses (Lunar Analog Glass, Solar Glass NTR-1, Window Glass and Dunite Glass).
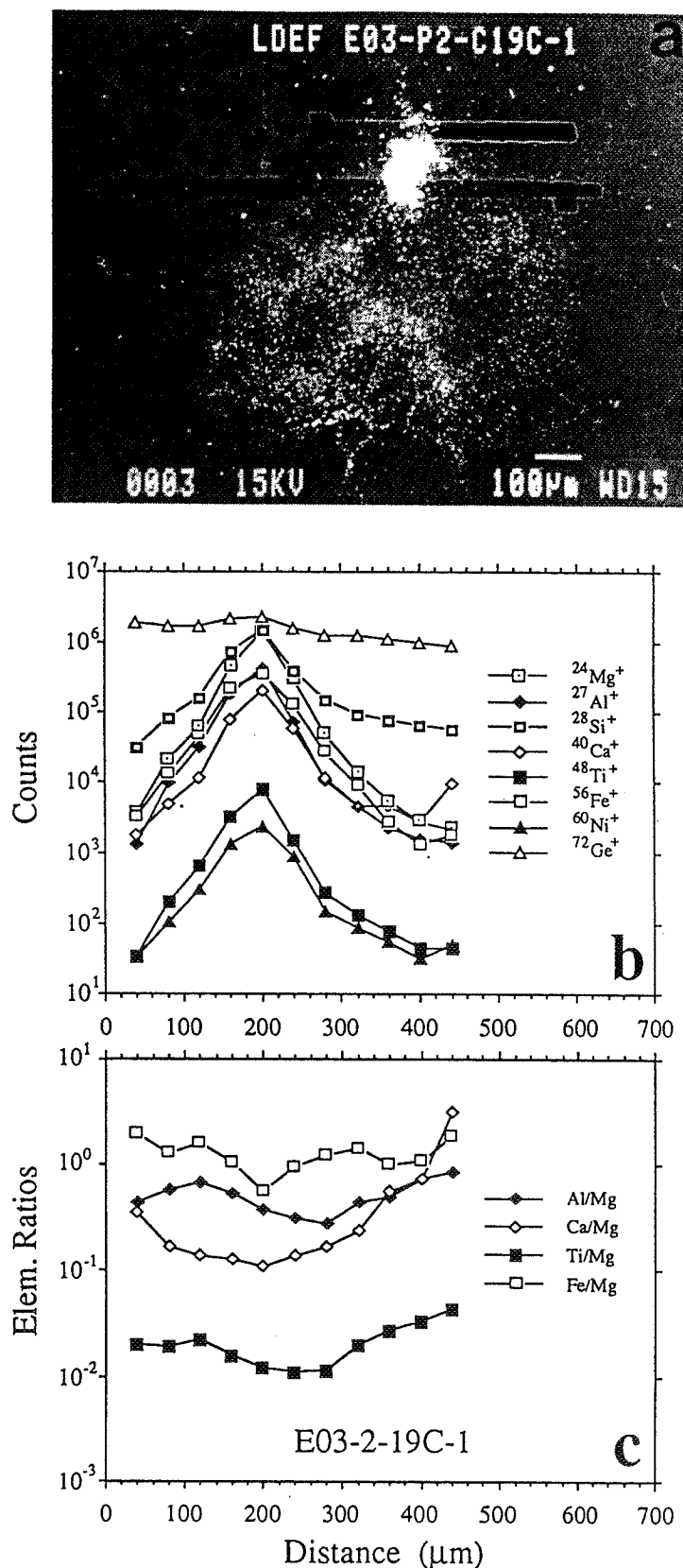
Figure 5. Ion microprobe elemental scans across impact E03-2-19C-1. Profiles in b and c correspond to the upper scan in the SEM micrograph.

Because of the problems with Si contamination of the Ge wafers we normalized the lateral intensity profiles to Mg by applying the relative sensitivity factors of Table 2. The resulting profiles of atomic elemental ratios are shown in Fig. 5c. One feature typical for almost all impacts is apparent from this figure: elemental ratios change across a lateral profile or, in other words, the deposits from the impact have different spatial distributions for different elements. For example, the Fe/Mg ratio has a minimum at lateral position 200 μm, where all the elements show a maximum, and changes by more than a factor of two 80-100 μm to the left and right of the maximum position. This can also be seen directly in Fig. 5b where the $^{56}Fe^+$ profile is slightly wider between positions 100 μm and 300 μm than the $^{24}Mg^+$ profile. This means that Fe apparently is distributed over a wider area than Mg.

Table 2. Secondary ion sensitivity factors relative to Mg.

Element	S
Na	3.28 ± .15
Al	0.77 ± .09
Si	0.13 ± .01
Ca	1.47 ± .24
Ti	0.50 ± .04
Cr	0.38 ± .15
Mn	0.51 ± .09
Fe	0.47 ± .07

Most impacts show even more complex distributions of the deposited elements. An example is impact CO2-1-20D-2 whose SEM micrograph after SIMS analysis is shown in Fig. 6a. The corresponding lateral intensity profile is displayed in Fig. 6b. There are several interesting observations to be made on this impact, which was classified as CD (crater with deposits). The first is that the ion signals of elements apparently deposited from the projectile (Mg, Ca, Fe) are much lower in the crater itself (dip in the middle of the profile) than in surrounding areas. Secondly, the concentrations of Mg and Fe are much higher to the left of the crater than to the right, although on the SEM micrograph the area to the right shows much more "structure" in the impact. The reason for this apparent paradox is that what is "seen" in the SEM is mostly damage to the Ge surface by high-velocity debris from the impact, which, however, contains only little deposited material, while the deposits themselves are not seen in the SEM. Finally, in this impact different elements have very different spatial distributions: the $^{56}Fe^+$ signal is higher than the $^{40}Ca^+$ signal to the left of the crater, but lower to the right. It is likely that such changing elemental ratios reflect heterogeneities in the chemical composition of the original projectile.
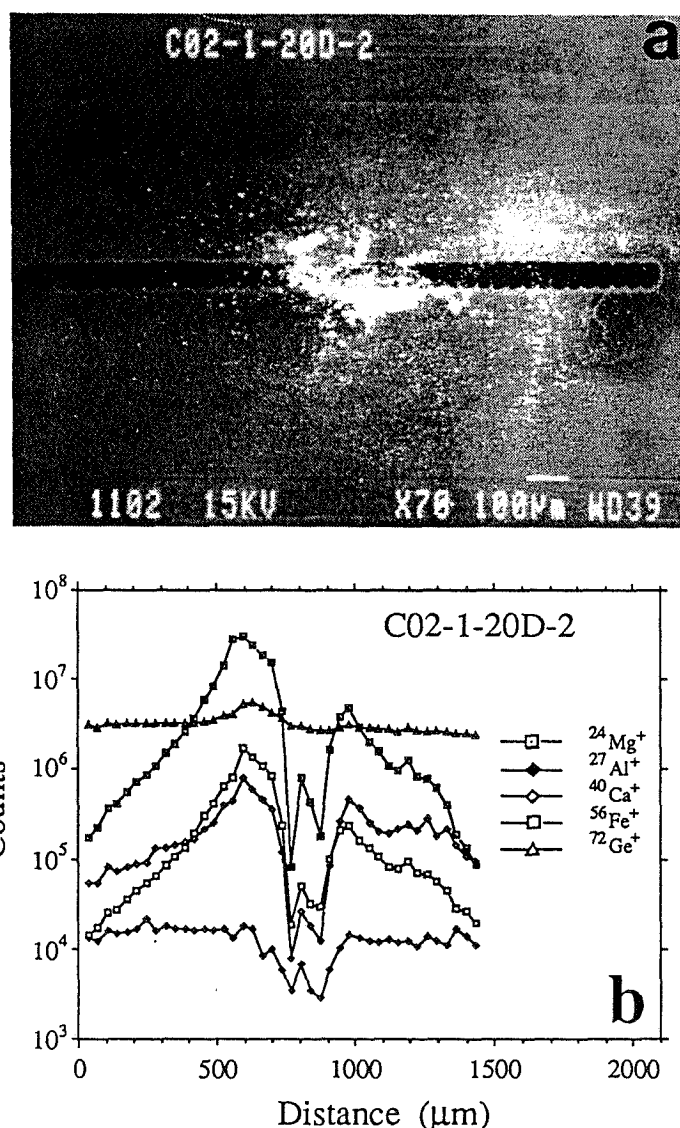
Figure 6. Ion probe scan across impact CO2-1-20D-2, a crater with associated deposits.
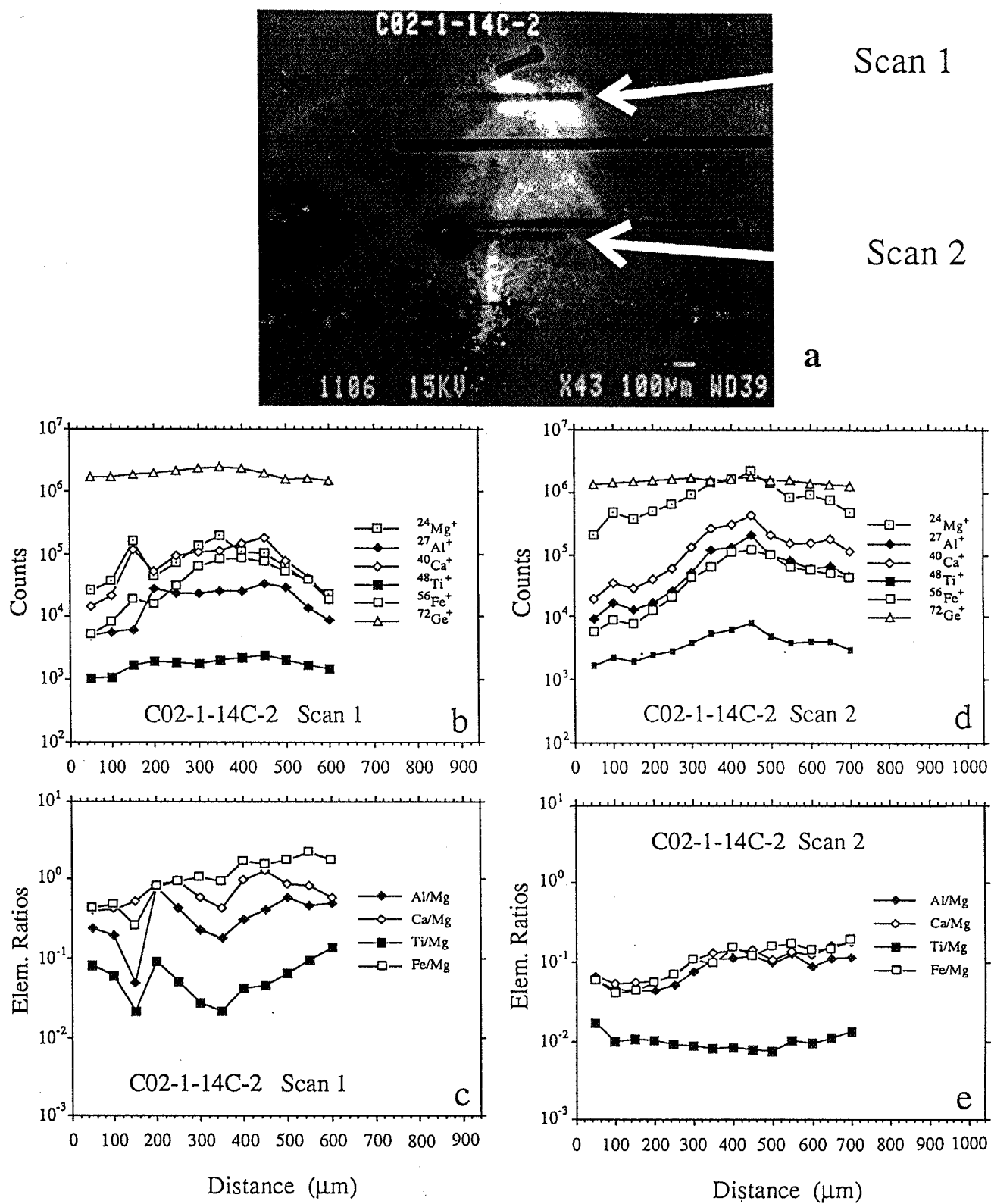
Figure 7. Two ion microprobe elemental scans across the same extended impact.

An even more extreme example of elemental heterogeneity is shown in Fig. 7, depicting a large extended impact (C02-1-14C-2) classified as SW (spider web) together with the results of two lateral scans (the short scans in the SEM micrograph). Not only do the absolute concentrations differ between the two scans (Fig. 7b,d) but there are also large differences in the elemental ratios (Fig.7c,e).

The non-uniform distribution of different elements in the deposition area of a given extended impact makes it difficult to obtain average elemental ratios. As a compromise we have taken elemental ratios determined at the maximum of the $^{24}Mg^+$ signal for a given scan. Histograms of these elemental ratios are plotted in Fig. 8 together with histograms of the same ratios measured by SIMS on individual stratospheric dust particles of probable extraterrestrial origin (ref. 12). Chondritic compositions are indicated for reference. The ratios measured in projectile deposits on the LDEF Ge wafers not only show much wider
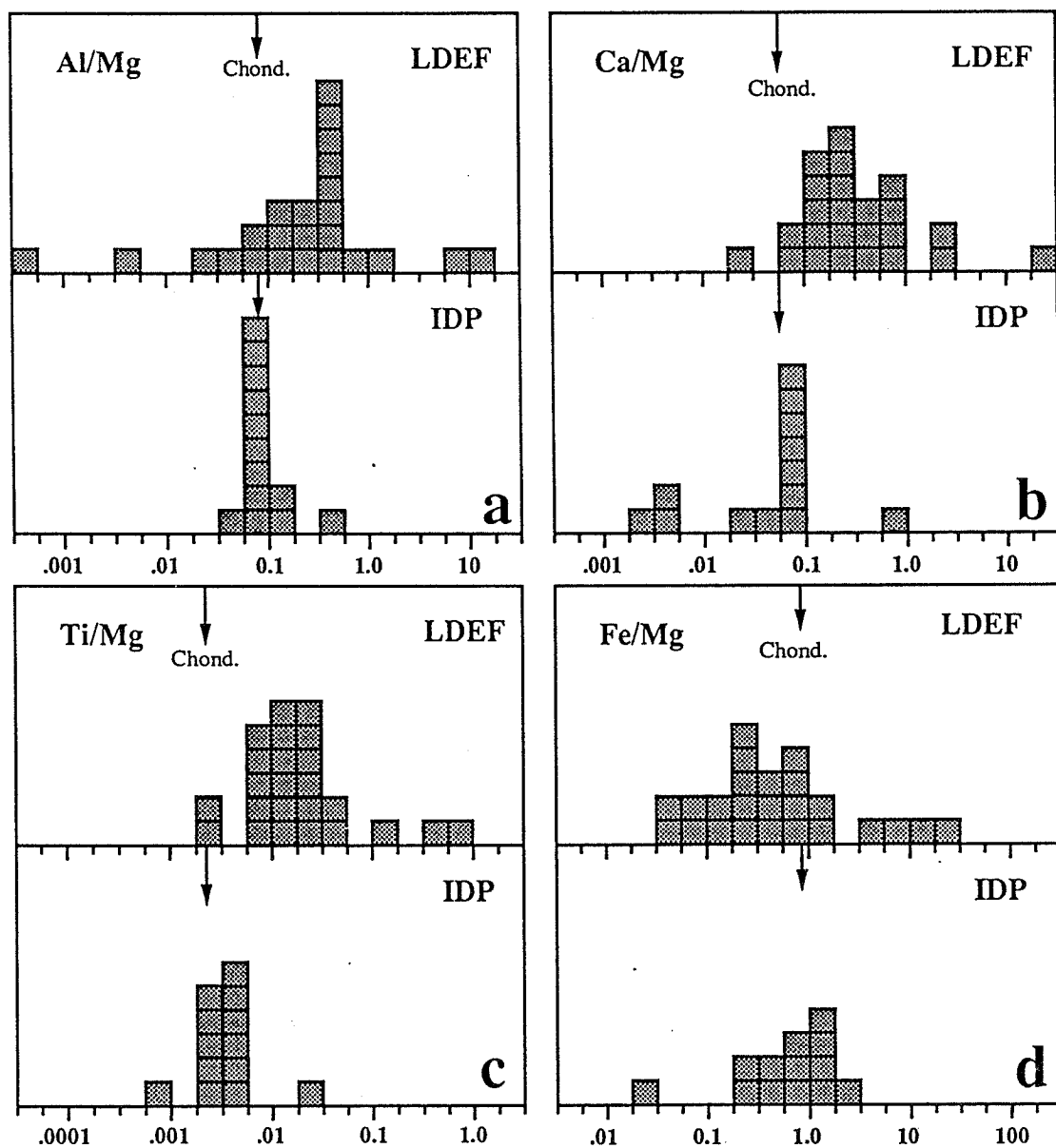
Figure 8. Histograms of elemental ratios in LDEF deposits and interplanetary dust particles.

distributions than those of IDPs but the mean of the distributions are systematically shifted relative to one another. This shift is toward lower values for Fe/Mg but toward higher values for the other three ratios, Al/Mg, Ca/Mg, and Ti/Mg.

There are at least two explanations for these differences. The first is simply that the particles whose material was collected on the Ge wafers on LDEF have chemical compositions that differ significantly from those of IDPs collected in the stratosphere. The second is that the impact process caused strong fractionation between the elements so that the compositions of the deposits do not accurately reflect those of the projectiles. One reason the particles that impacted LDEF have compositions different from IDPs could be that a major portion of them are not interplanetary dust but man-made debris. This, however, is unlikely in our case. First, collection on the trailing edge discriminates to a large extent against orbital debris. Furthermore, Mg is the dominant element in most impacts compared to Fe, Al, Ca and Ti. This is not expected for most man-made debris in orbit, which in this size range is presumably dominated by Al-oxide particles from the exhaust of solid fuel rockets. Moreover, we did not detect any impacts that contain primarily Al (Fig. 9).

Before we consider the possibility of differences in the chemical composition of interplanetary dust particles collected on LDEF and in the stratosphere, we have to discuss elemental fractionation during the impact process. There is evidence for such fractionation from simulation impacts onto the same foil/Ge wafer targets as flown on LDEF. The analysis of 12 extended impacts on the Ge produced by Lunar Analog Glass and Solar Glass showed fractionation between Mg and the other elements in the deposits with average fractionation factors relative to Mg of 0.28 for Fe, 0.58 for Si, 1.60 for Al, 1.95 for Ti and 2.41 for Ca. A fractionation factor smaller than one means that, compared to the projectile, less of the element is found in the deposition area than Mg and the
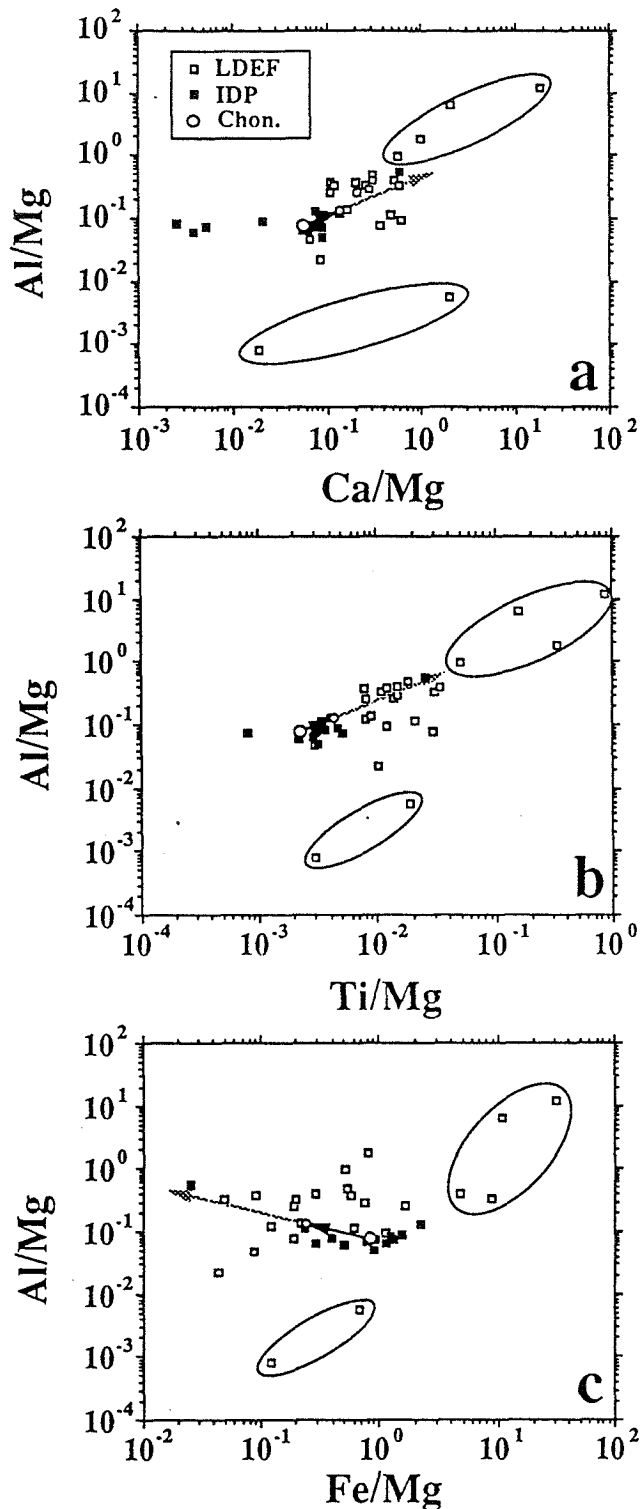
Figure 9. Scatter plots of elemental ratios in LDEF impact deposits and in interplanetary particles. Also shown are chondritic ratios, the elemental fractionations determined from simulation impacts (solid arrows) and the extension of these fractionations (light arrows).

opposite is the case for fractionation factors greater than one. We note that elemental fractionations are related to the relative volatilities of the elements during high temperature evaporation and condensation: the elements Fe and Si are more volatile than Mg and are depleted in the deposits relative to Mg while Al, Ca and Ti are more refractory and are enhanced relative to Mg.

During the impact apparently a large part of the projectile either melts or evaporates. Elements with different volatilities behave differently during this process. More volatile elements such as Fe are almost completely vaporized and expand into a larger volume before they condense onto the Ge and foil surfaces. More refractory elements, on the other hand, either remain in the melt or, if they evaporate, condense sooner and therefore onto a more limited area. Except for the (small) fraction that escapes through the penetration hole, all of the projectile material is retained inside the capture cell but some (preferentially the more volatile elements) is distributed over such a large area that it is lost in the background. For example, if the material of a 10μm projectile is spread out over an area of 1 mm diameter, its thickness is only 2.5 atomic monolayers, only 1/6 of a monolayer for the 4 mm largest observed extended impact.

Figure 9 shows scatterplots of pairs of elemental ratios for the LDEF deposits and individual IDPs. Also shown are the chondritic compositions and the shifts in these compositions if this material experienced the same elemental fractionations as those determined in the impact simulation experiments. The differences between most LDEF deposit compositions and the IDP compositions qualitatively agree with the shifts expected from fractionation during impacts, except that the differences are much larger than the shifts predicted from fractionation. However, we cannot exclude the possibility that elemental fractionations are actually much higher during impacts on LDEF than during simulation impacts. We have already pointed out that the LDEF extended impacts on the Ge are generally much larger than the simulation impacts from which the above fractionation factors were derived. It is reasonable to expect that elemental fractionation factors increase with the size of the extended impact feature. However, the uncertainty in this extension, the extremely irregular structure of most impact features and the fact that the fractionation factors undoubtedly depend on the composition of the projectile itself set a fundamental limit to the extent to which the projectile composition can be derived from the measured composition of the deposits.

Tentatively we can identify most of the LDEF impacts as being caused by cosmic dust particles. Six data points in Fig. 9 fall completely outside of the predicted trend due to elemental fractionation (they are enclosed in ellipses in the Figures). Four of them have extremely high Al/Mg, Ti/Mg and Ca/Mg but also very high Fe/Mg and are likely to be contaminants. The other two have low Al/Mg ratios. This leaves us with 18 (75%) impacts of likely interplanetary origin. While some of them have only little deposited material, some have plenty of it (see, e.g., Figs. 5, 6 and 7) and are candidates for future isotopic measurements. We also plan additional chemical analyses of elements that can easily be detected as negative secondary ions such as C, O, and S.

CONCLUSIONS

1. SIMS analyses of 24 extended impact features on Ge surfaces from "bare" trailing edge capture cells show evidence for projectile material in all of them, but there are large variations in the detected concentrations.

2. The deposits are very thin and cannot be detected by EDX analysis; SIMS appears to be the only method to detect them.

3. Elemental concentrations on the Ge do not correlate exactly with impact features seen in the SEM images; the latter are dominated by damaged regions which contain little projectile material.

4. There is evidence for large variations of elemental ratios within a given extended impact, indicating a heterogeneous chemical composition of the projectile.

5. Comparison with simulation impacts indicates that most LDEF impacts analyzed by SIMS were caused by small ($<10\mu m$) projectiles.

6. At least 75% of the analyzed impacts appear to be from interplanetary dust particles but elemental ratios scatter much more than those measured in IDPs collected in the stratosphere.

7. Elemental ratios are also shifted compared to IDPs, with refractory elements being relatively enriched. These shifts are likely to be due to elemental fractionation effects caused by evaporation during the impact process, but systematic differences between IDPs and LDEF impacts cannot be ruled out.

FUTURE WORK

Fractionation effects should be much less pronounced in isotopic ratios than in elemental ratios. Moreover, such effects will not obscure large anomalies of specific isotopes (if present) such as those found by us in studies of interstellar grains isolated from meteorites (ref. 13). As a consequence, future work will concentrate on isotopic measurements in those impacts that have been found in our initial survey to contain sufficient amounts of projectile material.

We have also refrained from studying the 12 intact (precious) capture cells until our handling and analysis techniques had been perfected on the more abundant, extended impacts found in the bare cells. The analysis of the intact cells should provide a critical test of the usefulness of our capture cell concept for future space flight experiments.

Detailed studies of impacts on the cells from the leading edge tray E8 should yield data relevant to the orbital debris problem. The ratios of extended impacts to single craters in these cells should allow us to determine when the plastic cover foils failed on the leading edge capture cells.

515

REFERENCES

1. Bradley, J. P.; Sandford, S. A.; and Walker, R. M.: Interplanetary dust particles. In Meteorites and the Early Solar System, eds. Kerridge, J. F.; and Matthews, M. S.; University of Arizona Press, 1988; pp. 861-895.
2. Brownlee, D. E.: Cosmic dust: collection and research. Ann. Rev. Earth Planet. Sci., 13, 1985, pp. 147-173.
3. Flynn, G. J.: Asteroids, Comets and Meteors III, 1989, pp. 59-62.
4. Flynn, G. J.: Survival of large micrometeorites on atmospheric entry: implications for their sources and the flux of cometary dust. Lunar Planet. Sci. XXII, 1991, pp. 393-394.
5. Zinner, E.; Kuczera, H.; and Pailer, N.: Simulation experiments for the chemical and isotopic measurements of interplanetary dust on LDEF. Lunar Planet. Sci. XIII, 1982, pp. 891-892.
6. Jessberger, E.; Kuczera, H.; Lange, G.; Sutton, S.; and Zinner, E.: Ion microprobe analyses of simulated LDEF impact residues. Lunar Planet. Sci. XVI, 1985, pp. 400-401.
7. Lange, G.; Eigner, S.; Igenbergs, E.; Jessberger, E. K.; Kuczera, H.; Maas, D.; Sutton, S.; Weishaupt, U.; and Zinner, E.: Ion microprobe sensitivities and their application to multielement analysis of LDEF impact residues. Lunar Planet. Sci. XVII, 1986, pp. 456-457.
8. Fraundorf, P.; Lindstrom, D.; Pailer, N.; Swan, P.; Walker, R.; and Zinner, E.: Rapid erosion of plastics in near-earth orbit and a means of prevention. Lunar Planet. Sci. XIV, 1983, pp. 205-206.
9. Fraundorf, P.; Lindstrom, D.; Pailer, N.; Sandford, S.; Swan, P.; Walker, R.; and Zinner, E.: Erosion of mylar and protection by thin metal films; AIAA Shuttle Environment and Operations Meeting; 1983; Paper 83-2636, pp. 131-137.
10. Fechtig, H.; Grün, E.; and Kissel, J.: Laboratory simulations. In Cosmic Dust, ed. McDonnell, J. A. M.; Wiley and Sons, New York, 1978; pp. 607-669.
11. Igenbergs, E.: Ein neuer Beschleuniger für die Simulation von Mikrometeoriten. Forschungsbericht, 1974, pp. BMFT-FBW 1974-03.
12. Stadermann, F.: Rare earth and trace element abundances in individual IDPs. Lunar Planet. Sci. XXII, 1991, pp. 1311-1312.
13. Zinner, E.; Tang, M.; and Anders, E.: Interstellar SiC in the Murchison and Murray meteorites: I sotopic composition of Ne, Xe, Si, C, and N. Geochim. Cosmochim. Acta, 53, 1989, pp. 3273-3290.

SIMS CHEMICAL ANALYSIS OF EXTENDED IMPACTS ON THE LEADING AND TRAILING EDGES OF LDEF EXPERIMENT AO187-2

S. Amari, J. Foote, P. Swan, R. M. Walker, E. Zinner
McDonnell Center for the Space Sciences and Physics Department
Washington University
One Brookings Drive
St. Louis, MO 63130-4899
Phone: 314/935-6257, Fax: 314/935-6219

G. Lange
Max-Planck-Institut für Kernphysik
Postfach 103980
D-6900 Heidelberg, Germany
Phone: 6221 516 247, Fax: 6221 516 540

SUMMARY

Numerous "extended impacts" found in both leading and trailing edge capture cells have been successfully analyzed for the chemical composition of projectile residues by secondary ion mass spectrometry (SIMS). Most data have been obtained from the trailing edge cells where 45 of 58 impacts have been classified as "probably natural" and the remainder as "possibly man-made debris." This is in striking contrast to leading edge cells where 9 of 11 impacts so far measured are definitely classified as orbital debris. Although all the leading edge cells had lost their plastic entrance foils during flight, the rate of foil failure was similar to that of the trailing edge cells, 10% of which were recovered intact. Ultra-violet embrittlement is suspected as the major cause of failure on both leading and trailing edges. The major impediment to the accurate determination of projectile chemistry is the fractionation of volatile and refractory elements in the hypervelocity impact and redeposition processes. This effect had been noticed in a simulation experiment but is more pronounced in the LDEF capture cells, probably due to the higher average velocities of the space impacts. Surface contamination of the pure Ge surfaces with a substance rich in Si but also containing Mg and Al provides an additional problem for the accurate determination of impactor chemistry. The effect is variable, being much larger on surfaces that were exposed to space than in those cells that remained intact. Future work will concentrate on the analyses of more leading edge impacts and the development of new SIMS techniques for the measurement of elemental abundances in extended impacts.

INTRODUCTION

LDEF experiment A0187-2 consisted of 228 Ge-mylar cells for the capture of interplanetary dust material. The principle of the experiment and a more detailed description of the capture cells is given by Amari et al. (ref. 1). One full tray of capture cells was exposed on the leading edge and an area equivalent to a full tray in two locations on the trailing edge.

All cells on the leading edge and 90% of the cells on the trailing edge had lost their plastic covers (bare cells) during exposure in space. However, Ge plates from both leading and trailing edge bare cells contain extended impact features that must have been produced by high velocity projectiles while the mylar foils were still intact. Moreover, these extended impact features contain projectile material that could be measured by secondary ion mass spectrometry (SIMS), an extremely sensitive surface analysis technique.

Last year we reported results of the optical scanning of 100 bare cells from the trailing edge as well as the first results of SIMS analysis of 24 extended impacts on Ge from these cells (ref. 1). In the present paper we extend the SIMS analysis to 16 additional impacts from bare trailing edge cells and 18 impacts from the 12 trailing edge cells that had retained their plastic covers. We also optically scanned the Ge plates of 106 capture cells from the leading edge for single craters and extended impacts and analyzed 11 of the latter by SIMS.

OPTICAL SCANNING FOR SINGLE CRATERS AND EXTENDED IMPACTS

All cells were optically scanned under oblique illumination at a magnification of 240× as previously described by Amari *et al.* (ref. 1). The results are given in Table 1. There is a clear distinction between "extended impact features" and "single craters." The former consist of complex patterns of debris and ejecta, and must have been produced while the plastic cover foils were in place. In contrast, "single craters" show no evidence of associated debris deposits and represent direct hits on the Ge plates <u>after</u> the foils had failed in flight. The distinction between "extended impacts A and B" is subjective with the former generally being larger than the latter and being visible with the unaided eye. Although we have chosen to analyze the type A impacts first, we consider it likely that also many of the type B impacts contain sufficient material for chemical and isotopic analysis.

Table 1. Analysis of Cells on AO187-2

	Cells scanned	Single Craters	Extended Impacts A	Extended Impacts B	Measured by SIMS Ge	Foil
Trailing Edge Bare	100	203	53	155	40	
Trailing Edge Covered	12	-	20	26	18	5
Leading Edge	106	5121	403	298	11	

514

There are several differences between the impacts on the two sides of the spacecraft. Figure 1 shows histograms of the sizes of extended impacts on the leading and trailing edge cells. As can be seen, the trailing edge impacts have, on average, much larger diameters than those on the leading edge. This is undoubtedly a reflection of the lower projectile velocities and shallower impact directions (ref. 2) for the trailing edge. An additional reason could be differences in the chemical compositions and physical properties of the projectiles, since a large fraction of leading edge impacts appear to be caused by man-made debris (see below), while those on the trailing edge are predominately produced by cosmic dust particles.

Fig. 1. Distribution of the sizes of extended impacts on Ge plates for both leading and trailing edge capture cells.
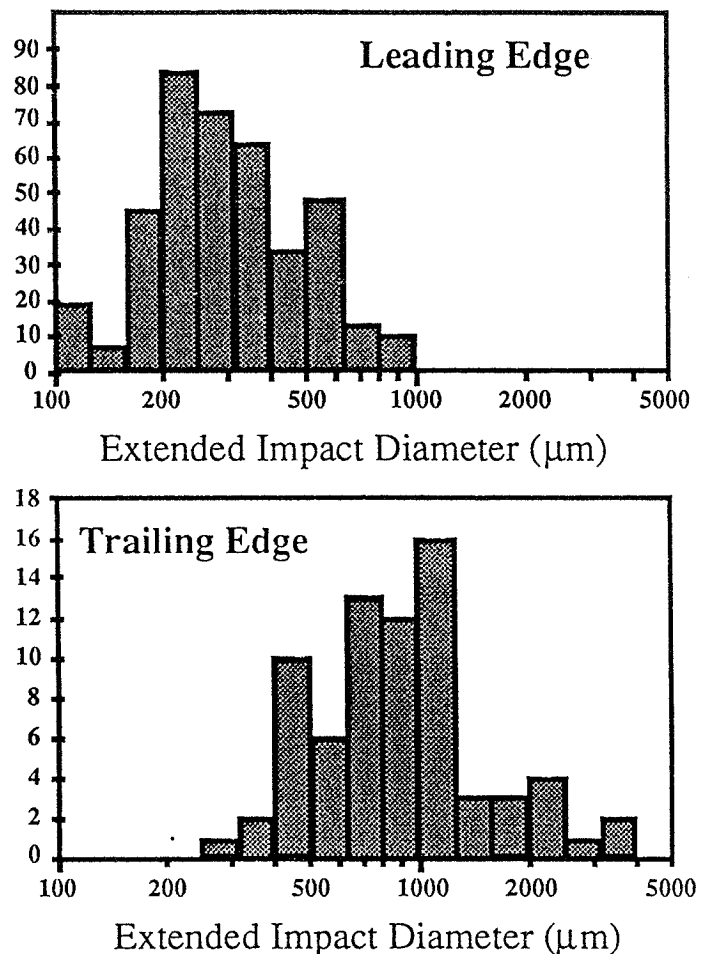
LIFETIMES OF ENTRANCE FOILS - FRONT AND BACK

All of the plastic cover foils on the leading edge failed during flight while ~ 10% on those of the trailing edge survived. At first glance it thus appears that there may have been a qualitative difference in the foil destruction processes between front and back. However, as we will show below, this is a somewhat misleading impression. While it is true that the foil loss occurred at a higher rate on the leading edge, foils on this edge lasted for long periods of time in space. The difference in foil survival between front and back is thus more quantitative than qualitative.

Although some corners and edges of many cells contained small pieces of intact or rolled up foil material, when different foils ruptured they appear to have done so suddenly, exposing a major part of the area of any given cell to free space. Since direct hits producing single craters are possible only after the foil has been removed, the density of single craters in a given cell is proportional to the time it was exposed without a foil provided, of course, that the flux of impacting particles is constant in time.

Consider first the results from the leading edge cells. Although none of the plastic foils survived for the entire exposure, it is clear that many remained in place for a considerable period of time. In Fig. 2, we show a histogram of the number of single craters per cell. The width of the distribution far exceeds that expected for a single exposure time for all cells and indicates, in itself, a distribution of survival times. The locations of individual impacts were plotted for the two cells with the largest density of single craters. No clustering was seen, consistent with the assumption that single craters represent a random population of impinging particles.

The maximum number of single craters per cell is 101. If we assume that the foil on this cell failed immediately after launch, the distribution of craters in Fig. 2 would indicate that more than 50% of the foils survived at least to the half way mark and that some foils lasted through almost 90% of the total exposure time before rupturing.

In contrast to single craters, the density of extended impacts is a measure of the time the foils remained in place. However, only a small fraction of the particles that produce single craters produce extended impacts that are visible under the same scanning conditions. Thus the statistics on extended impacts are less favorable than those for single craters. Figure 3 is a scatter diagram showing the relation between extended impacts (A plus B) and single craters. This figure also shows the same data after binning into groups of 20 single craters and averaging the number of extended impacts in each bin. The data show the expected inverse relationship between number of extended impacts and number of single craters (Fig. 3). Furthermore, the best-fit line through these binned averages intercepts the abscissa at 111 craters per cell, not very different from the maximum number of 101
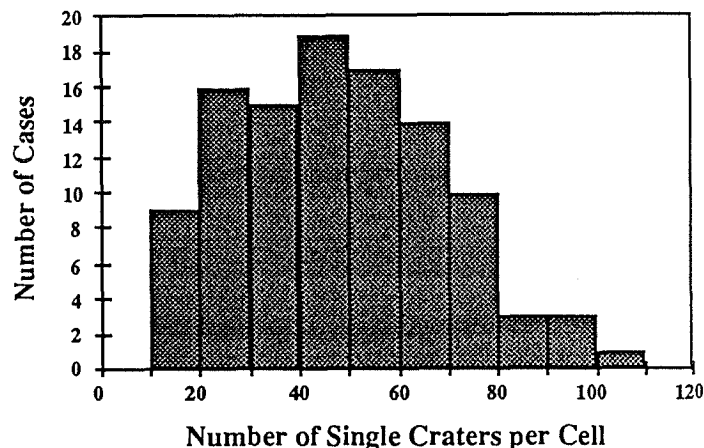
Fig. 2. Distribution of the number of single craters per cell for leading edge capture cells. Such craters are produced only after the entrance foils have ruptured and their numbers are a measure of the time different Ge surfaces were exposed to space. The width of this distribution indicates a considerable spread in foil lifetimes.
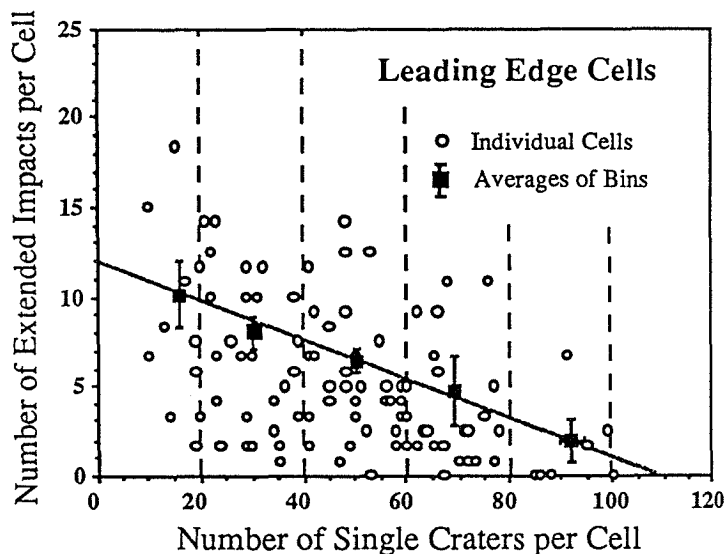
Fig. 3. Extended impacts and single craters for leading edge capture cells. The solid squares show averages for the number of extended impacts versus single crater counts binned in groups of 20. Since extended impacts are produced only when the entrance foils are intact and single impacts only after they have ruptured, there is an inverse correlation between the two densities.

we assumed to be the number of craters on a cell whose foil was removed right after the launch of LDEF. Thus the two indicators of foil lifetimes yield consistent results and a sizable fraction of the foils on the leading edge survived a considerable fraction of the total time of LDEF in orbit.

Consider next the data on the trailing edge cells. The 12 cells which remained covered during the entire period have a total of 46 extended impacts of types A and B for an average of 3.8 impacts/cell. The bare cells have an average of 2.1 extended impacts/cell, suggesting that the foils lasted, on average, about half of the total time. This is similar to the result inferred for the leading edge cells from consideration of the single impact crater data. The first order conclusion is thus that the foil failure rates are similar for both the leading and trailing edge cells.

While we do not know in detail what caused the foils to fail, certain general aspects of the problem seem clear. Firstly, since the rates at which the foils failed were approximately the same for both the leading and trailing edges, the same causative factors must be present. Thus neither atomic oxygen erosion nor enhanced impact fluxes, which are characteristic of the front side only, appears to be the principal cause of failure. However, both effects could have contributed to an enhanced failure rate of the leading edge cells.

Some contribution of atomic oxygen erosion indeed seems likely since we have evidence that most impacts alone do not destroy foils. This conclusion is based on the presence of peculiar elliptical features that accompany approximately half of the extended impacts on the leading edge. Fig. 4 shows two such features that are associated with extended impacts. The fact that these elliptical features occur only on the leading edge Ge plates and only in connection with extended impacts indicates that they must have been caused by the interaction of the residual atmosphere, mostly atomic oxygen, with the penetration hole left by the high velocity impact. At present we do not have any detailed understanding of this process.

Foil failure probably results from repeated stressing of the foils due to cyclical temperature changes, coupled with degradation of the mechanical properties of the foils in the space environment. In spite of the fact that the plastic was metal-coated, we consider UV
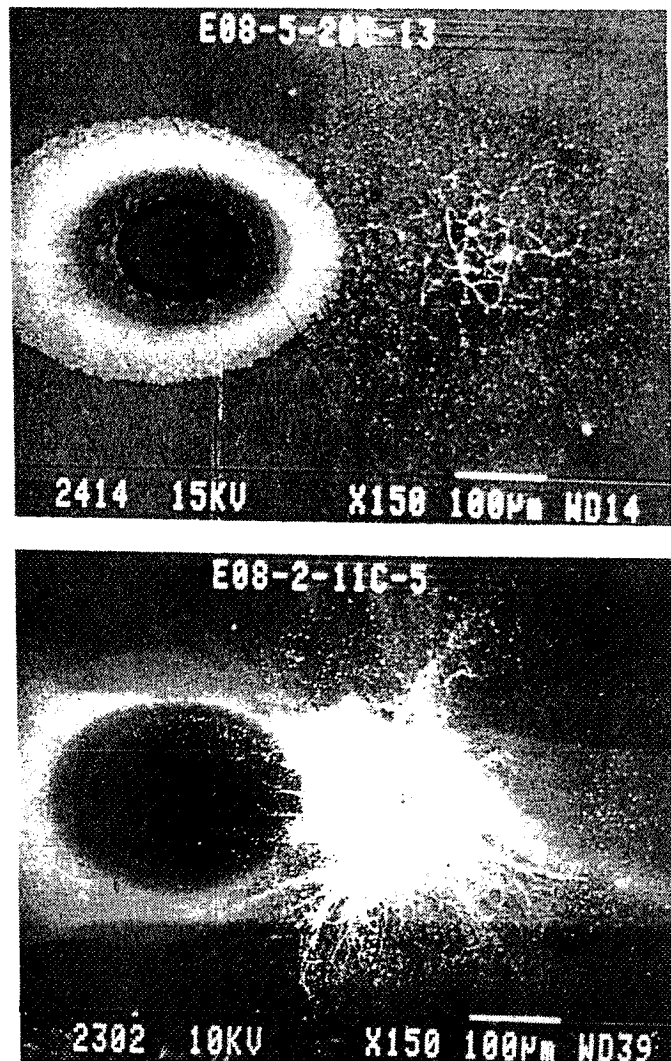
Fig. 4. Elliptical features associated with extended impacts. These multi-ringed concentric features are seen in about half of the extended impacts found in the leading edge cells. Their presence indicates that the entrance foils did not rupture immediately upon impact.

embrittlement to be a likely source of this degradation.

We plan to continue to address the question of foil lifetimes by determining the density of small craters (down to ≤ 1 μm diameter) that can be seen by scanning at 1000× in an SEM. A possible difficulty with this approach, however, is the observation of temporal changes of the flux of very small particles impinging on the leading edge capture cells (ref. 3).

SIMS CHEMICAL ANALYSIS OF EXTENDED IMPACTS

The procedures for the SIMS chemical analysis of projectile deposits in extended impacts have been described previously (ref.1). To summarize briefly: lateral multielement profiles across extended impacts are obtained by integrating secondary ion intensity depth profiles measured in areas 40 μm apart. From the ion signals we obtain elemental ratios by applying sensitivity factors determined from measurements on standards. Previous measurements have shown that different elements can be distributed differently in a given impact, apparently reflecting compositional heterogeneity of the projectile. While we plan to use a newly acquired secondary ion digital imaging system to determine the spatial distribution of various elements over the entire impact area, for the time being we have adopted a compromise – elemental ratio determinations from lateral profile data are estimated by taking ion intensities measured at the maximum of the $^{24}Mg^+$ signal.

During SIMS measurements of extended impacts on the Ge plates it became clear that the sensitivity of the analysis technique is not one of the limiting factors (interestingly, SEM-EDS studies of the same impacts gave no signals of projectile material, even at low voltages). The major
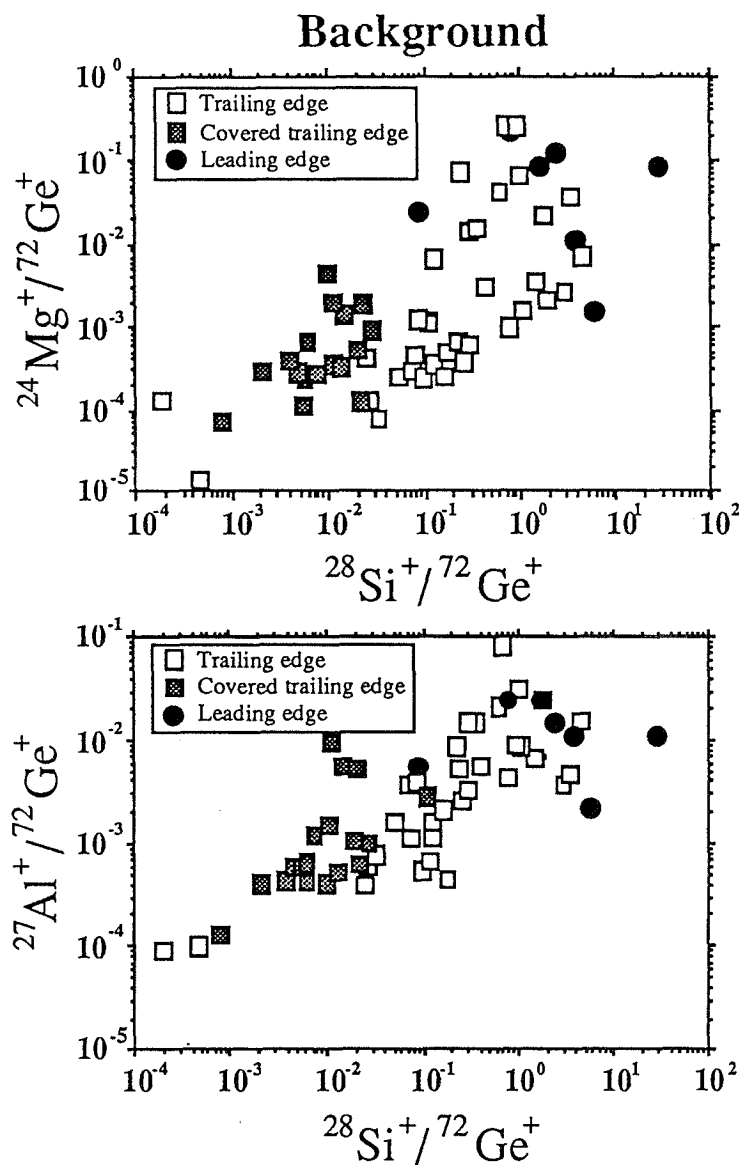
Fig. 5. Surface contamination on Ge target plates in regions well removed from impact debris.

limitation on the SIMS data is rather the high level of contamination encountered on the surface of the Ge plates. While contamination with Si is worst, high background levels are found also for other elements. Fig. 5 shows ion signals measured <u>outside</u> of the impact areas normalized to the $^{72}Ge^+$ signal. Background levels of Mg and Al are correlated with those of Si. The plots furthermore clearly show that the contamination levels are related to the exposure of the cells during flight: on average, the backgrounds are lowest on the plates from capture cells that retained their plastic foils and highest on the plates exposed on the leading edge. While we originally thought that outgassing of the RTV that was used to bond the Ge plates to the Al substrate was the main source for the Si contamination, the fact that other elements correlate with the Si demonstrates that there must be other sources of contamination. The fact that the leading edge plates have the highest background levels may be an important clue suggesting, for example, that redeposition of atomic oxygen induced erosion products may be significant.

Analysis of Impacts on the Leading Edge

To date we have performed SIMS analyses on 11 extended impacts from the leading edge. In 8 of these impacts enhancements were seen only for Al. Fig. 6 shows one of the impacts and the corresponding lateral ion intensity profiles. One additional impact showed enhancements mostly in Ti with minor Al. Its SEM micrograph and lateral ion intensity profiles are presented in Fig. 7. The remaining two impacts have hardly any elemental enhancements that can be attributed to projectile material in the region that exhibits damage features in the SEM. It has already been mentioned that the leading edge Ge plates suffer from extremely high levels of contamination (Fig. 5), and this may be the reason that no projectile material above background could be detected in these two impacts.
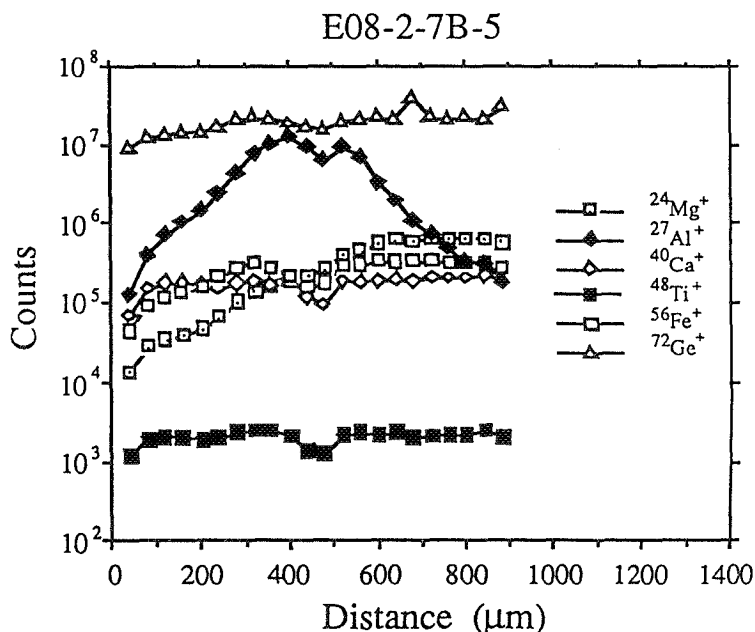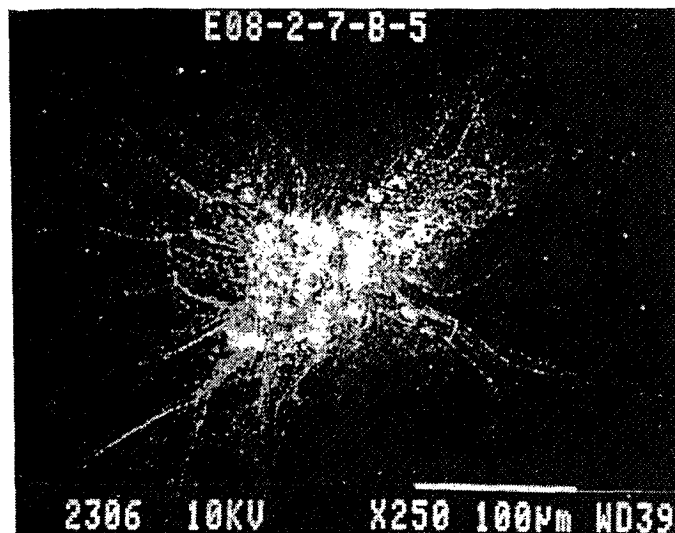
Fig. 6. Signature of an orbital debris impact found in a leading edge cell. The ion microprobe scan across impact E08-2-7B-5 shows Al as the only element that is present at enhanced levels.

The extended impacts from the leading edge capture cells thus differ significantly from those from the trailing edge capture cells in the chemical composition of their deposits. No impacts with only Al or Ti deposits such as those depicted in Figs. 6 and 7 have been seen on the trailing edge Ge plates. We can thus, with reasonable certainty, assign the 9 leading edge impacts that contain only Al or Ti to man-made debris. The first are most likely Al-oxide particles produced by solid-fuel rocket engines, the latter (mostly Ti) either is a chip of paint or a fragment of spacecraft hardware. Although the number of investigated leading edge impacts is still extremely limited, their chemical analysis shows that they are dominated by man-made debris.

Analysis of Impacts on the Trailing Edge

In the present work, we analyzed another 16 extended impacts from the bare trailing edge capture cells (increasing the total number of impacts from these cells analyzed by SIMS to 40) and 18 extended impacts from the 12 trailing edge cells that had retained their foils. Histograms of computed elemental ratios for all impacts with clear maxima of the plotted elements in the lateral intensity profiles (32 of the bare cell impacts and 16 of the covered cell impacts) are shown in Fig. 8. They are compared with elemental ratios measured by SIMS in interplanetary dust particles collected in the stratosphere (ref. 4,5). Chondritic ratios are indicated for reference.

E08-2-17A-3

Fig. 7. Another probable orbital debris impact in a leading edge cell. The ion microprobe traverse across extended impact E08-2-17A-3 shows enhancements of both Ti and Al.

For the Ca/Mg, Ti/Mg and Fe/Mg ratios there appears to be no systematic difference between the impacts from the bare and covered capture cells. The Al/Mg ratios, however, are on average smaller in impacts from the covered cells than in those from the uncovered cells. A possible explanation for this discrepancy is the higher level of contamination on the exposed Ge plates (Fig. 5).

Fig. 8. Histograms of elemental ratios measured in LDEF extended impacts compared to previous measurements of a set of interplanetary dust particles (IDPs) collected in the stratosphere. Average chondritic values are indicated by the arrows.

The systematic shift of the elemental ratios measured for extended impact residues compared to IDPs and chondritic ratios has previously been noted and discussed by us (ref. 1). We pointed out that laboratory simulation experiments indicated that projectile residue material on the Ge plates is

fractionated in its elemental composition relative to the original projectile with refractory elements being enhanced in the deposits relative to less refractory elements (ref. 6). These simulation experiments on foil/Ge cells identical to those flown on LDEF also showed that the elemental fractionations are larger for material on the Ge plates than for material deposited on the backside of the entrance foil (Fig. 9).

The impacts in the covered trailing edge cell provided us with the opportunity to test this elemental fractionation effect for projectiles captured on LDEF. So far we have attempted the analysis of foil deposits from 5 impacts in the covered cells. Unfortunately, the SIMS measurements of the foils are very difficult, mostly due to extreme embrittlement of the samples and their failure to stay stretched and smooth when mounted for ion probe analysis. We obtained a good SIMS analysis on only one foil deposit of the five tried. Data for this impact are discussed next.

Fig. 9. Element fractionation trends measured in laboratory impact experiments. The data are from the thesis of G. Lange Heidleberg, 1986 and were obtained with the W.U. ion microprobe. The ordinate shows measurements of the relative abundance of different elements in the impact debris compared to the abundance of those same elements in the glass projectiles used in the impact experiments. The abscissa orders the elements by a volatility index.

The extended impact on Ge and the backside of the foil featuring the penetration hole and signs of secondary ejecta are shown in Fig. 10 together with lateral profiles across the Ge impact and the deposits on the foil. The elemental ratios obtained from these profiles are plotted in Fig. 11 and compared to the fractionation of a projectile of chondritic composition expected from laboratory experiments. As expected, the material from impact EO3-2-11A-3 deposited on the Ge plate is more fractionated than the material found on the backside of the mylar foil. The relative fractionation for the LDEF impact is larger than the average obtained from the simulation experiments. This is probably a reflection of a difference in the impact velocities but could also reflect differences in chemical composition and physical properties (density, shape) of the projectile.

Although additional measurements on foil deposits are needed, the presence of elemental fractionations between Ge and foil deposits in one LDEF impact makes it likely that the dominant cause for the large differences between elemental ratios measured in extended impacts from the trailing edge and those measured in IDPs is elemental fractionation during the high velocity impact process. Intrinsic, large differences in chemical compositions between these two populations is less likely, although still possible.

522

E03-2-11A-3 Ge

E03-2-11A-3 Foil

Fig. 10. Ion microprobe profiles on both the Ge target plate and the underside of the entrance foil for impact E03-2-11A-3. Most of the capture cells lost their entrance foils during flight and those that survived are extremely brittle and difficult to mount. The data shown are for the only cell for which it has been proven possible to study impacts in the way that we had originally intended. As expected from simulation experiments the projectile signals are much higher for the debris on the foil than for the debris on the Ge target plate.

The presence of elemental fractionations in the impact deposits is the single largest impediment to accurate determination of projectile chemistry. In principle, all of the projectile material, except the small fraction that escapes back through the impact hole in the entrance foil, is deposited in the capture cell, i.e. in our design either on the Ge plate or the backside of the foil. However, more volatile elements are apparently deposited over a wider area of the Ge plate and foil and, when the surface concentration becomes too low, can no longer be detected. It is therefore important to measure the surface deposits over as wide an area as possible. Measuring the radial dependence of the abundances of different elements may allow the development of normalization procedures that could correct for fractionation
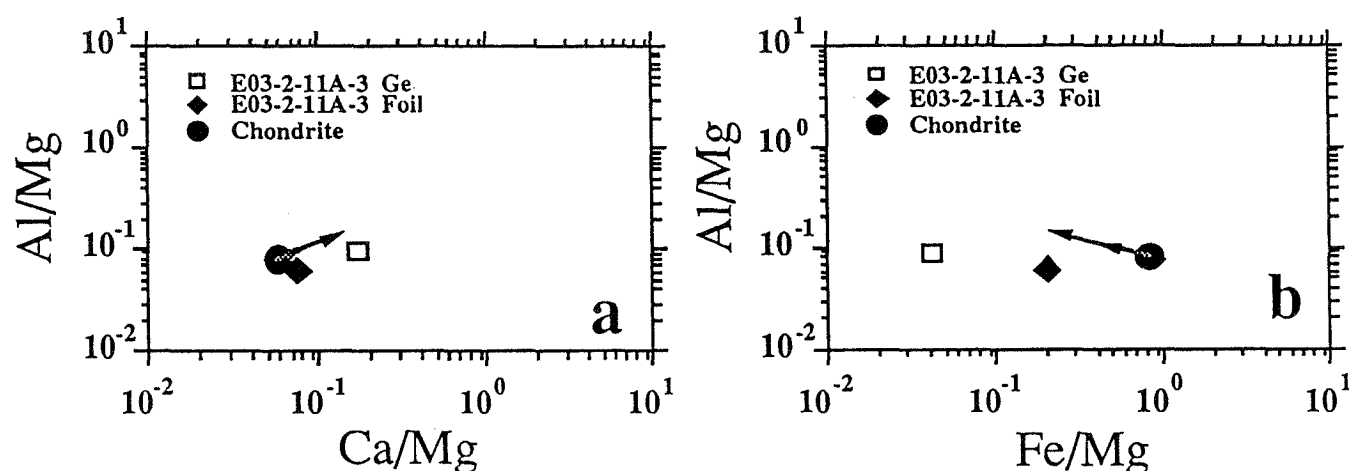
Fig. 11. Fractionation trends from the data on the intact cell shown in Fig. 10. The arrows indicate the fractionation trends previously obtained from laboratory simulation experiments of the type shown in Fig. 9. As expected from the prior work, the projectile material on the Ge plate is fractionated relative to that on the foil.

effects. In future space experiments, it would be desirable to have partitioned capture cells which would limit the area on which material from a given impact was deposited. It is not obvious, however, how to construct such a device while keeping all surfaces accessible to SIMS analysis.

IDENTIFICATION OF THE ORIGIN OF PROJECTILE MATERIAL

In spite of the problems caused by elemental fractionation the abundance data can be used to decide which LDEF impacts were caused by micrometeoroids and which ones by man-made debris. The situation is fairly simple for the extended impacts from the leading edge. Eight of these impacts show only Al enhancements and one shows Ti with minor Al and all can therefore be attributed to man-made debris with high confidence. Two impacts do not contain any clear enhancements and are thus unidentified.

The identification of the origin of trailing edge impacts is more difficult. One of them does not show any noticeable element enhancements and its origin is unidentified. Two impacts have enhancements in Fe only without any accompanying enhancements in Cr and Ni. They therefore cannot be caused by stainless steel debris particles. It is not unlikely that the projectiles are FeS particles. Such particles have been found in the stratospheric dust collection (ref. 7) and unmelted FeS fragments have been identified in LDEF craters (ref. 8). Since S is much more sensitive when measured as a negative secondary ion we do not have any S analysis yet on these two impacts but for the time being tentatively classify them as being of cosmic origin.

There are another four trailing edge impacts for which Fe is the dominant element (always discounting Si for which, as already discussed, no reliable measurements are possible because of its

524

extremely high contamination level). In one case the Fe is associated with Al, which makes man-made debris the most likely source for this particular impact. Although in the other three impacts Fe is very high, Mg enhancements are also clearly present. The Fe/Mg ratios are 24.8, 25.7, and 45.2, respectively. With some elemental fractionation during impact, the true Fe/Mg ratios of the projectiles are probably even higher. Although all three particles could have consisted mostly of FeS with some chondritic material attached, we cannot exclude a debris origin (Cr is low, however). The same is true for another two trailing edge impacts in which Al and Ca are dominated by contamination on the Ge plate and in which Fe/Mg is high.

The remaining 49 trailing edge impacts have their elemental ratios Al/Mg, Ca/Mg, Ti/Mg and Fe/Mg plotted in Fig. 12. Also plotted are the same ratios for interplanetary dust particles collected in the stratosphere and for chondrites. The arrows indicate the directions of elemental mass fractionation during hypervelocity
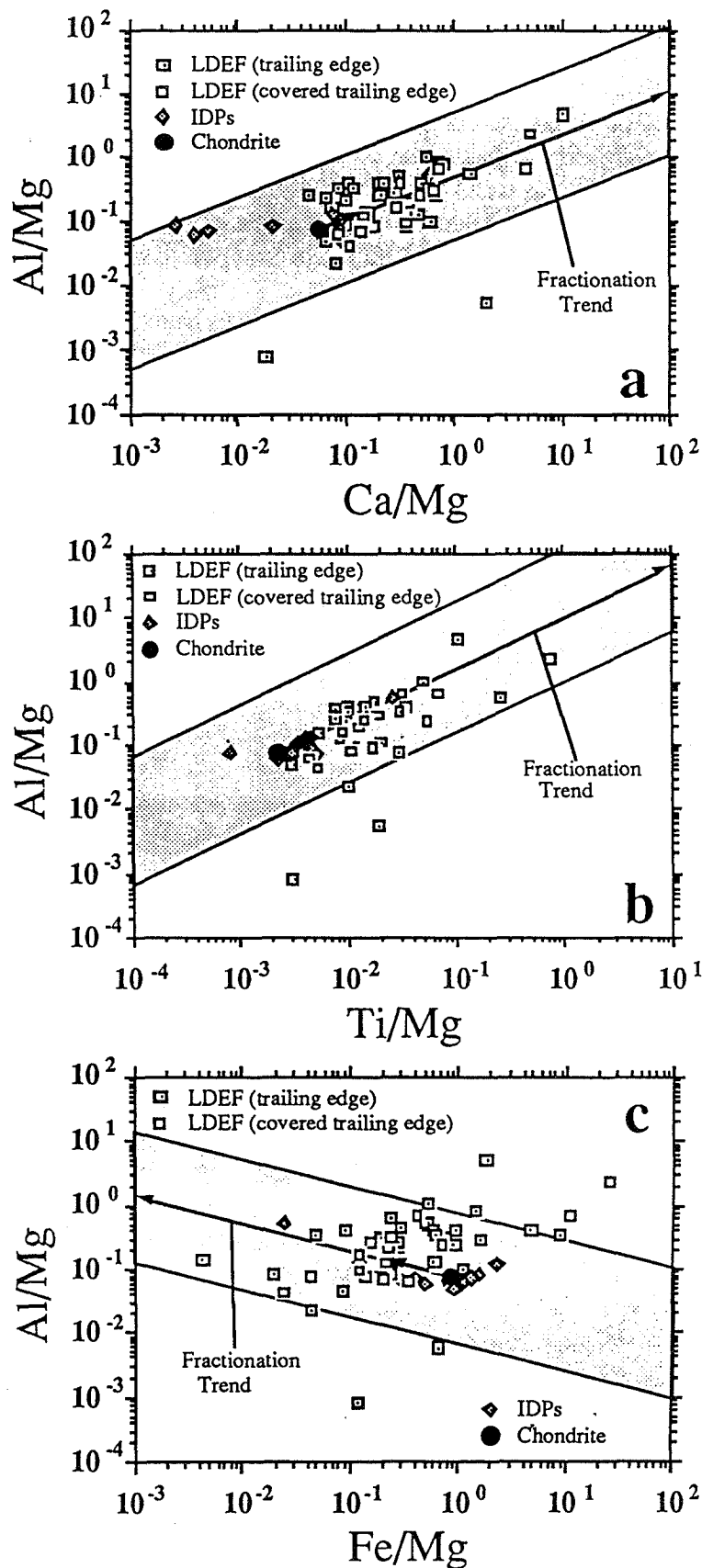
Fig. 12. Elemental ratios measured in the ion microprobe for trailing edge extended impacts. The arrows indicate elemental fractionation trends determined from laboratory simulation experiments. As discussed in the text, impacts whose compositions lie in the shaded regions are classified as "probably natural" and those outside as "possibly orbital debris." In striking contrast to the results for the leading edge cells, it appears that the majority of trailing edge impacts are produced by cosmic dust particles.

impacts determined in laboratory simulation experiments. The Al/Mg, Ca/Mg and Ti/Mg ratios of most trailing edge impacts actually deviate from the chondritic composition in the expected directions but, as already mentioned, the deviations are much larger than the fractionation seen in the laboratory experiments. We consider such large fractionations to be the likely result of the higher velocities of the LDEF impacts. As a working criterion for distinguishing between cosmic dust and man-made debris, we classify impacts that plot inside a region bounded by lines a factor of 10 above and below the fractionation trend extrapolated from laboratory experiments as being of likely interplanetary dust origin. Impacts that plot outside this region are classified as being of possibly man-made debris origin. In Figs. 12a and 12b all impacts except two plot inside of the region while in Fig. 12c, 7 plot outside.

A tentative classification of all impacts analyzed by SIMS is thus as follows (Table 2): nine of 11 leading edge impacts are of man-made origin, the origin of two impacts without projectile material cannot be identified. In contrast, 45 of 58 impacts on the trailing edge are of probably natural origin, two of them probably from FeS particles, 43 from particles with compositions similar to those of chondrites, whereas 12 impacts are possibly caused by man-made debris. It should be pointed out, however, that the identification of man-made debris is much more certain for the leading edge impacts than those from the trailing edge. The former have compositions (only Al, Ti) that are expected for debris while the debris classification for the trailing edge is mostly by default; only one impact (mostly Fe and Al) can reasonably be associated with an expected terrestrial composition and there are no impacts with Al only on the trailing edge. Thus, most of those classified as possibly man-made debris may, in fact, be cosmic particles.

Table 2. Identification of Projectile Material

	Leading edge			Trailing edge		
	Micro-meteoroids	Debris	Unid.	Micro-meteoroids	Debris	Unid.
No enhancements	-	-	2	-	-	1
Enhancement in single element	-	8 (Al)	-	2 (Fe)	-	-
Enhancement in several elements	-	1 (Ti)	-	43	12 (poss.)	-
Total	0	9	2	45	12 (poss.)	1

SUMMARY AND CONCLUSIONS

1. The basic capture cell design worked successfully. As long as the entrance foils stayed in place projectile particles produced "extended impacts" that could be successfully analyzed by ion probe mass spectrometry.

2. All of the entrance foils on the leading edge and 90% of those on the trailing edge failed during flight. However, the statistics of single craters and extended impacts show that many foils on both edges lasted for a considerable period. Thus, analysis of "extended impacts" on both the leading and trailing edges was possible.

3. Analysis of leading edge impacts shows that at least 9 of 11 impacts studied are produced by man-made debris (the remaining two did not yield any elemental enhancements due to projectile material).

4. In contrast, the analysis of the impacts on the trailing edge area shows that 45 out of 58 are of probably natural origin. The identification of the remainder is uncertain but they are possibly due to orbital debris. However, no unambiguous example of a space debris impact was found on the trailing edge.

5. Most extended impacts have compositions that differ markedly from those measured for IDPs collected in the stratosphere. The differences are consistent with volatile/refractory element fractionation affecting particles with cosmic compositions. This effect had previously been seen by us in simulation experiments of hypervelocity impacts, but is more pronounced in the LDEF data, probably due to the high velocities of the impactors. Elemental fractionation in the impact process itself represents the largest single impediment to accurate measurements of projectile chemistry.

6. Contamination of initially clean Ge surfaces during exposure in space was also found to be a significant effect limiting the ability to make accurate measurements of projectile chemistry. The source of the Si seems to be outgassing from RTV, but other sources, contributing elements such as Mg and Al, are still unknown.

7. Because leading and trailing edge entrance foils failed at comparable rates, the major causative failure factors must be similar. While atomic oxygen erosion contributed to a somewhat higher failure rate on leading edge cells, it cannot be the major cause of failure. We suspect that UV embrittlement coupled with thermal cycling is responsible for most of the foil degradation.

8. Future work will concentrate on the analysis of more leading edge impacts and the development of new techniques for measuring elemental abundances in extended impacts.

REFERENCES

1. Amari, S.; Foote, J.; Simon, C.; Swan, P.; Walker, R.; Zinner, E.; Jessberger, E. K.; Lange, G.; and Stadermann, F. J.: SIMS chemical analysis of extended impact features from the trailing edge portion of LDEF experiment AO187-2. LDEF - 69 Months in Space, NASA CP-3134, part 1; 1991, pp. 503-516.

2. Zook, H. A.: Asteroidal versus cometary meteoroid impacts on the Long Duration Exposure Facility (LDEF). Second LDEF Post-Retrieval Symposium, NASA CP-3194, 1993.

3. Mulholland, J. D.; Simon, C. G.; Cooke, W. J.; Oliver, J. P.; and Misra, V.: Long-term particle flux variability indicated by comparison of interplanetary dust experiment (IDE) timed impacts for LDEF's first year in orbit with impact data for the entire 5.75-year orbital lifetime. Second LDEF Post-Retrieval Symposium, NASA CP-3194, 1993.

4. Stadermann, F.: Rare earth and trace element abundances in individual IDPs. Lunar Planet. Sci. XXII, 1991, pp. 1311-1312.

5. Stadermann, F.: Messung von Isotopen- und Elementhäufigkeiten in einzelnen interplanetaren Staubteilchen mittels Sekundärionen-Massenspektrometrie. Ph.D. Thesis, University of Heidelberg, Germany, 1990.

6. Lange, G.: Quantitative Multielementanalyse von Einschlagsrückständen auf LDEF-Staubdetektoren. Ph.D. Thesis, University of Heidelberg, Germany, 1986.

7. Brownlee, D. E.; Tomandl, D. A.; and Olszewski, E.: Interplanetary dust; a new source of extraterrestrial material for laboratory studies. Proc. 13th Lunar Planet. Sci. Conf., 1977, pp. 149-160.

8. Brownlee, D. E.; Hörz, F.; and Bradley, J.: Interplanetary meteoroid debris in LDEF metal craters. Second LDEF Post-Retrieval Symposium, NASA CP-3194, 1993.

SIMS CHEMICAL AND ISOTOPIC ANALYSIS OF IMPACT FEATURES FROM LDEF EXPERIMENTS AO187-1 AND AO187-2

Frank J. Stadermann
Technical University Darmstadt, Material Science Department
Hilpertstr. 31, Geb. H, D-64295 Darmstadt, Germany
Phone: (+49) 6151-813223, Fax: (+49) 6151-813222

Sachiko Amari, John Foote, Pat Swan, Robert M. Walker, Ernst Zinner
McDonnell Center for the Space Sciences and Physics Department
Washington University, St. Louis, MO 63130, USA
Phone: 314-935 6257, Fax: 314-935 4083

SUMMARY

Previous secondary ion mass spectrometry (SIMS) studies of extended impact features from LDEF capture cell experiment AO187-2 showed that it is possible to distinguish natural and man-made particle impacts based on the chemical composition of projectile residues. The same measurement technique has now been applied to specially prepared gold target impacts from experiment AO187-1 in order to identify the origins of projectiles that left deposits too thin to be analyzed by conventional energy-dispersive x-ray (EDX) spectroscopy. The results indicate that SIMS may be the method of choice for the analysis of impact deposits on a variety of sample surfaces. SIMS was also used to determine the isotopic compositions of impact residues from several natural projectiles. Within the precision of the measurements all analyzed residues show isotopically normal compositions.

INTRODUCTION

Among the most noticeable effects of the space environment on spacecraft are impacts produced by the bombardment with small particles from various sources. Several experiments on board the Long Duration Exposure Facility (LDEF) satellite dealt with the analysis of impact craters and projectile debris. There are two basic objectives for such experiments. One is the study of

micrometeoroids in order to determine the flux of interplanetary particles in space and to learn about their nature and origin. The other is the assessment of possible hazards to space flight posed by such impacts. For this purpose it is important to determine (a) the absolute number of impacts and (b) the ratio of natural (micrometeoroids) to man-made (orbital debris) impact particles. Various attempts have been made to estimate this ratio, *e.g.*, by comparing particle fluxes on differently oriented LDEF surfaces. However, a more direct approach to this problem is based on the chemical characterization of particle residues. Since micrometeoroids and orbital debris particles have distinct chemical properties, it is possible to determine the relative contribution of either type to the total particle flux by analyzing the composition of impact debris on LDEF surfaces.

Although all outer surfaces of the LDEF satellite are covered by impact features of various types and sizes, only few are suited for micro-chemical analysis. What can usually be seen on space exposed materials are only the *effects of hypervelocity impacts*, such as craters, dents, and cracks, but not remnants of the impacting particle. Due to the high velocities of impacts (typically several km/sec), practically no projectile material survives the collisions unaltered and only rarely chunks of projectile material can be found within or in the vicinity of impact craters that are large enough for energy dispersive x-ray analysis (EDX) . However, frequently there is a thin layer of debris around impact features where some fraction of the particle material re-condensed after being vaporized during impact. This layer of debris is generally too thin to be seen in either optical or scanning electron microscopes (SEM), but secondary ion mass spectrometry (SIMS) can often be used to analyze this material even when its thickness is only a few atomic monolayers.
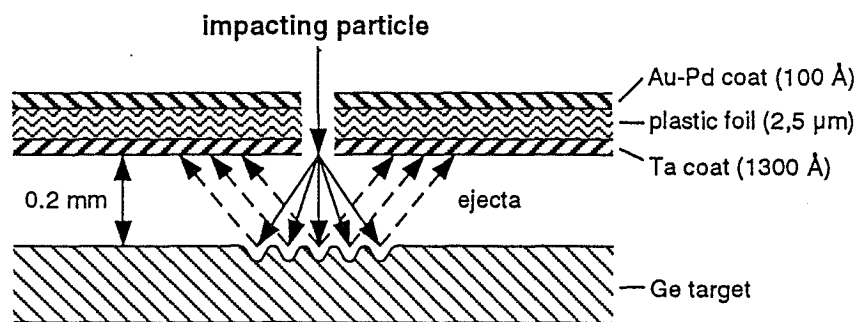
Figure 1. Schematic of capture cell experiment AO187-2.

In principle, impacts on all kinds of surfaces can be analyzed to determine the nature of the projectile material. In practice, however, most accurate analytical results can be achieved from impacts on clean substrates and with relatively large amounts of deposited debris. These conditions are satisfied in the capture cell experiment AO187-2, which was specifically designed for this kind of investigation. The principle of that experiment is shown in Figure 1. A target plate of high-purity germanium is covered with a thin foil separated by a small distance. A high velocity particle of sufficient size penetrates the foil and may be disrupted in the process, spreading out into a debris

shower. This shower impacts the target plate and is further disrupted, melted and vaporized. Some of the projectile material is retained in the impact region on the germanium plate. The projectile material ejected from the impact zone is collected on the backside of the foil and on the surrounding area of the germanium plate. Since only a small amount of material can escape through the impact hole in the cover foil, most impact debris stays in the capture cell and can be analyzed after the cell has been disassembled.

In our previous studies analyses were focused on samples from capture cell experiment AO187-2 (refs. 1, 2). Because most foils did not survive the $5\frac{1}{2}$ years of exposure in space, we analyzed extended impact features on the germanium plates, produced by projectiles which had arrived while the plastic foils were still in place. First, several different types of extended impact features were identified during optical and SEM analyses. The chemical compositions of the deposits were then determined by SIMS step scans across the impact features. At each step the composition of the surface layer was measured with an O$^-$ primary beam of 1-2 nA that was rastered over an area of 40 μm x 40 μm. The width of individual steps was chosen between 35 and 60 μm each. Since each measurement consisted of up to 50 steps, these traverses had a typical length of several hundred μm and width of about 40 μm. The secondary ion signals of the elements O, Mg, Al, Si, Ca, Ti, Fe, Ni, Ge, and Ta were monitored during the scans. These elements were chosen because they are the most abundant elements in cosmic dust particles and/or in the capture cells themselves. Typical results from one of these scans are shown in Fig. 2. The increase in secondary ion signals near the center of the impact can clearly be correlated with impact deposits.
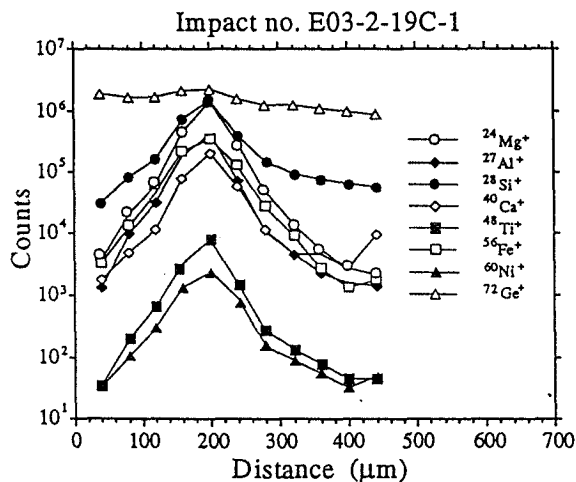
Figure 2. Secondary ion signals of different elements in a traverse across an impact feature on a Ge plate. The center of the impact is located near the 200 μm distance mark.

To date more than 60 extended impacts on germanium plates from experiment AO187-2 have been analyzed by SIMS for the chemical composition of the projectiles. Ion signals associated with material from the impacts could be detected in almost all analyzed impact areas despite serious problems with contamination. It was possible to discern the most likely origins of the projectiles by comparing the compositions of the deposits to those of cosmic dust particles and well known types of man-made debris. Thus we could show that at least 75% of the impacts on the trailing edge of LDEF were caused by micrometeoroids while virtually all analyzed impacts on the leading edge were caused by man-made debris particles (ref. 2).

After having established that SIMS is a useful analytical technique for the determination of the chemical composition of thin layers of impact deposits on the germanium capture cells, we undertook an investigation of its applicability to the analysis of impacts on other LDEF surfaces. We also used SIMS for the measurement of the isotopic compositions of certain impact debris fragments. Such measurements have not yet been possible on thin deposition layers on the germanium plates of the capture cells due to the thinness of the layers which causes the signal at a given isotopic mass to change rapidly with time.

CHEMICAL ANALYSIS OF GOLD TARGETS FROM EXPERIMENT AO187-1

Next to samples from the capture cell experiment, impacts on witness plates of high-purity Au from experiment AO187-1 appeared particularly interesting because debris analyses on these surfaces had already been performed by conventional SEM-EDX techniques (ref. 3). Unfortunately, in more than 50% of all Au impacts studied no detectable EDX signals could be found, obviously complicating the statistical interpretation of the data. We tried to improve this situation by analyzing these Au samples with the same SIMS analysis technique that we had used earlier on the Ge impacts. For a preliminary investigation Fred Hörz generously provided us with 15 Au samples that had previously been studied by SEM-EDX (ref. 3). Eleven of those impact projectiles had been classified as "natural", one as "man-made" and the origins of the other three were still unknown.

SIMS measurements of the Au impacts posed some analytical problems. The impact craters in the Au foil are generally relatively deep and are surrounded by a "lip" of Au that rises above the original sample surface. Since SIMS requires a flat sample surface it was necessary to develop a new sample preparation technique for the analysis of these kinds of impact craters (Fig. 3). Preliminary studies had shown that the most interesting areas to analyze in the Au samples are impact residues located inside the crater and on the lip. In order to flatten the lip a quartz plate was pressed onto the sample surface. After the surface was even, a needle was carefully pressed against the underside of the thin Au sheet to push the bottom of the crater up. The entire procedure was monitored under a

Figure 3: Steps in the sample preparation of Au targets from LDEF.

stereomicroscope through the quartz disk. That way the surfaces from inside the crater walls became accessible to SIMS measurements on a flat surface. After these preparations, the SIMS scanning technique was applied to the Au witness plates.
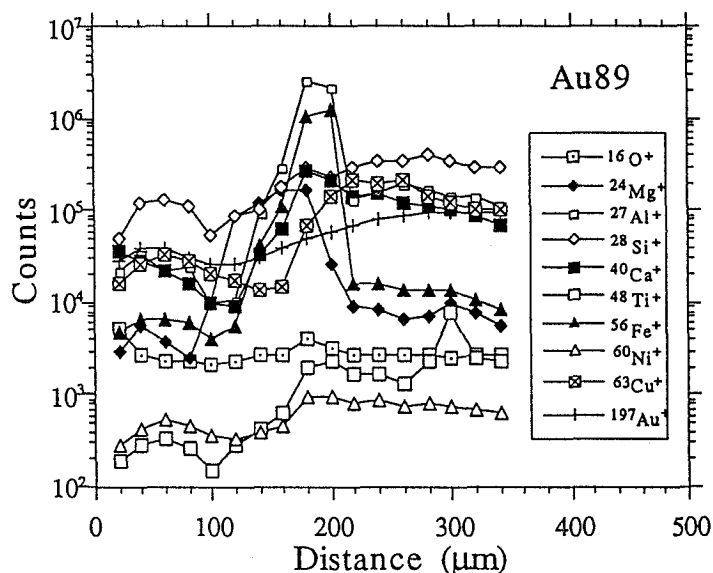
Figure 4: Secondary ion count rates from a SIMS scan across AO187-1 impact "Au89".
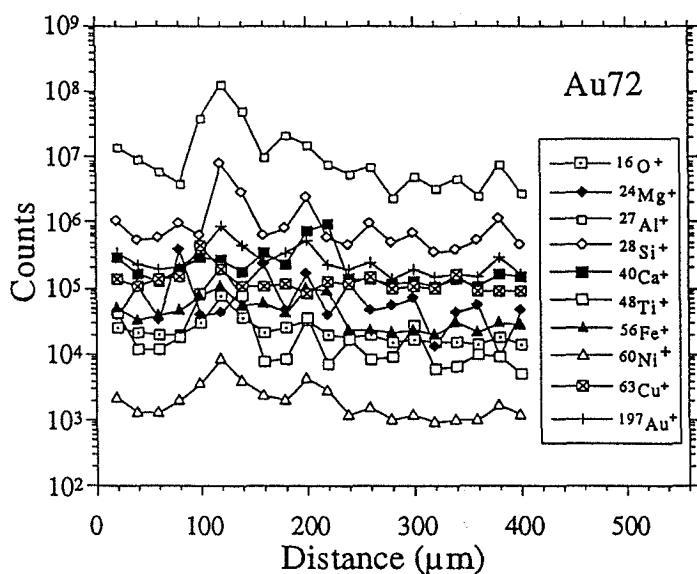
Figure 5: Secondary ion count rates from a SIMS scan across AO187-1 impact "Au72".

The SIMS scans of these "high-purity" Au substrates revealed high levels of contamination that cannot be attributed either to the impacts themselves or to contamination originating from the LDEF spacecraft (see Figs. 4–6). Instead, it appears that the Au target itself contains significant amounts of trace contaminants. In spite of this problem, which led to generally higher background-level in most of the measurements, it was indeed possible to determine the origin of the projectiles in several of the Au target impacts. To date SIMS scans have been made across seven flattened craters from experiment AO187-1. Examples of the results are shown in Figures 4–6.

Impact "Au89" (Fig. 4) had originally been classified as "natural" based on the EDX analysis of small chunks of debris that had been found in the crater. The SIMS scan shows a complex pattern with several elements –such as Al, Fe, Ca, and Mg– clearly enriched in the vicinity of the crater whose center is located near the 200 μm distance mark. An elemental signature like this is typical for a natural particle (micrometeoroid). The EDX classification of this impact can therefore be confirmed.

Figure 5 shows data from a scan across impact "Au72" that was classified as "man-made" before. Here too, that classification could be confirmed by the SIMS measurements.
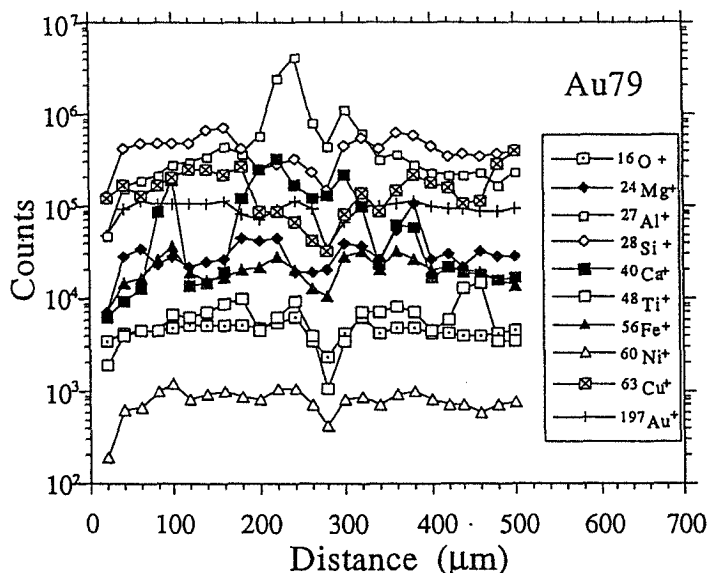
Figure 6: Secondary ion count rates from a SIMS scan across AO187-1 impact "Au79".

The most enriched element at the center of the crater (near the 120 μm mark) is Al, accompanied only by a smaller enrichment of Si. Such a prominent Al-rich composition is highly indicative of an aluminum-oxide particle from rocket exhausts.

The origin of the projectile that caused impact "Au79" was unknown because no debris could be found in the SEM-EDX study that was large enough for a determination of the chemical composition. Here the strength of SIMS as a highly-sensitive micro-analytical technique becomes obvious (Fig. 6). Only aluminum is significantly enriched near the position of the crater at the 240 μm distance mark. This impact can unambiguously be classified as "man-made".

The SIMS measurements did not always allow the identification of hitherto unknown projectiles, but the total number of "unknowns" was reduced. It appears that SIMS is the method of choice for the analysis of impact debris on various surfaces, provided the samples can be suitably prepared for SIMS analysis.

In an effort to characterize the chemical composition of some of the "natural" impact projectiles on the Au target plates in more detail, we measured the relative abundances of 24 elements in two chunks of debris from the impacts "Au104" and Au280". The results of these measurements are shown in Figures 7 and 8, together with values of the meteoritic abundances of C1 chondrites. These C1-abundances are well known from the study of meteorites (ref.4) and there is reason to expect that natural projectiles, *i.e.*, micrometeoroids, have compositions that are similar to those of C1 chondrites (ref. 5). Since only relative abundances can be measured with SIMS, all elements are normalized to Si, whose concentration was arbitrarily set to its C1-abundance.

Since two fragments were analyzed from each impact an upper limit of the precision of the measurement can be estimated from the variation between both measurement runs (inherent heterogeneities in the sample would lead to even bigger variations between the two measurements). The precision appears to be quite good for the majority of the elements. However, the accuracy of the determinations is not as good, possibly due to the inherent problems of quantification in the SIMS technique. Still, the similarity between the compositions of the projectiles and the C1-abundances is striking. Since all elemental abundances are normalized to Si, an over-abundance of

this element would lead to seemingly lower abundances of the other elements. Interestingly, in impact "Au280" Ca is depleted while in impact "Au104" Fe, Co, and Ni concentrations are lower than the C1-abundances. Both observations agree with earlier measurements of certain cosmic dust particles that were collected in the stratosphere (ref. 5). Clearly, this determination of the abundances of 24 elements leaves no doubt about the natural origin of the particles that caused these impacts.
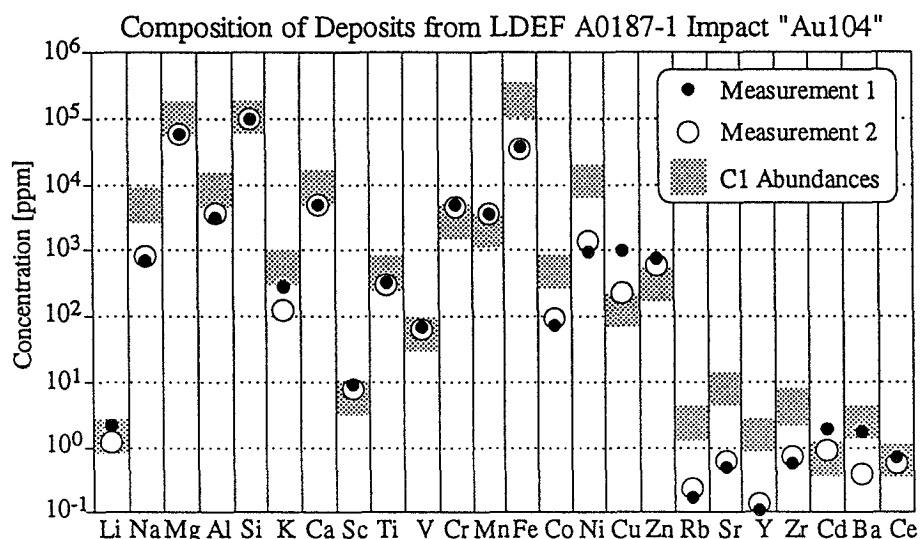
Figure 7: Elemental abundances of two fragments normalized to a condritic Si value and compared to C1-abundances.

Figure 8: Elemental abundances of two fragments normalized to a chondritic Si value and compared to C1-abundances.

ISOTOPIC MEASUREMENTS IN IMPACTS FROM AO187-1 AND AO187-2

We were also able to perform the first isotopic measurements of impact debris on LDEF. Isotopic analysis of LDEF impacts was one of the original objectives of experiment AO187-2. The isotopic composition of projectile material is of special interest since natural particles (micrometeoroids) are found to have isotopic compositions that sometimes are very different from normal, terrestrial values (refs. 6, 7). If similar anomalies could be found in impact debris that would be one more piece of evidence for an extraterrestrial origin of the projectile material. Moreover, the LDEF impacts represent a different, and possibly isotopically distinct, sampling of the total infall of extraterrestrial material than do micrometeorites recovered in the stratosphere. The results of the isotopic measurements are given here in the δ-notation, which denotes the deviation of the measured isotopic ratio from the normal ratio (*i.e.*, the ratio of a terrestrial standard) in permil (‰). Example: If a measured $^{15}N/^{14}N$ ratio were 5% higher than normal, the corresponding δ-value would be $\delta^{15}N = 50$‰. *Small* variations of the isotopic compositions can also be observed in terrestrial material. Therefore all results have to be compared to the maximum observed range of isotopic compositions in terrestrial material and only an object with isotopic compositions clearly outside of that range can unequivocally be classified as extraterrestrial. On the other hand, a normal isotopic composition does not necessarily imply a terrestrial origin.
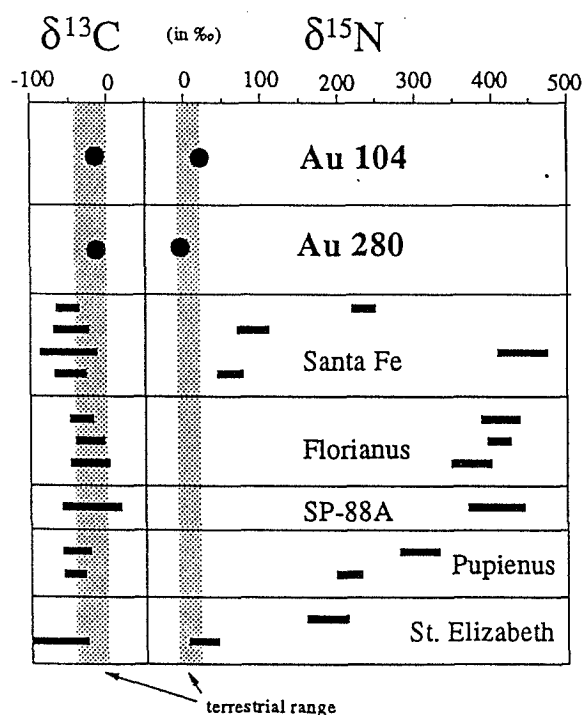
Figure 9: Average C and N isotopic compositions of impact residue from "Au104" and "Au280" and values of IDPs for comparison.

From the Au-foils from LDEF experiment AO187-1 we selected impacts Au104 and Au280 because both have large amounts of apparent projectile residues and both had been classified as "natural" according to the EDX analyses. As shown above, this classification was confirmed by the SIMS measurements of major and trace elements.

In Figure 9 the C and N isotopic compositions of impact residues are compared to the values measured in interplanetary dust particles (IDPs) collected in the stratosphere (ref. 7) and to the range of ratios found in terrestrial samples. Although both projectiles are clearly of natural origin their C and N isotopic compositions are close to normal. This is not very surprising since only one third of all analyzed IDPs show isotopic anomalies in N and none show anomalies in C. The particle "Santa Fe" which is shown for reference has the largest N anomaly among all measured particles of that kind.
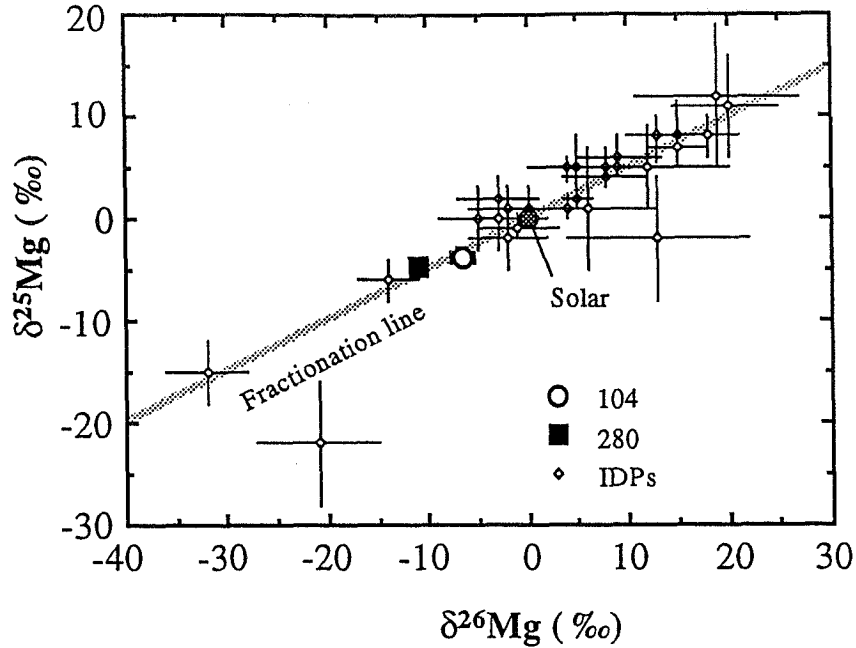
Figure 10: Three-isotope-plot of the Mg isotopic compositions of impact deposits from two AO187-1 impacts and those of Interplanetary Dust Particles (IDPs). The errors shown are 1σ.

Figures 10 and 11 show the Mg and Si isotopic compositions of impact debris from AO187-1 impacts "Au104" and "Au280" in three-isotope-plots. The isotopic compositions of elements with 3 stable isotopes are usually displayed in this way. The $\delta^{25}Mg$ and the $\delta^{26}Mg$ values refer to the $^{25}Mg/^{24}Mg$ ratio and the $^{26}Mg/^{24}Mg$ ratio, respectively ($^{29}Si/^{28}Si$ and $^{30}Si/^{28}Si$ for silicon). The normal isotopic compositions are denoted "Solar" in the diagrams. Small linear mass-dependent isotopic fractionations –which occur frequently, even in the terrestrial environment– would lead to isotopic compositions that are shifted from the "Solar" composition along a slope-$1/2$-line in a three-isotope-plot. This line is denoted "Fractionation line" in the diagrams. Any isotopic composition that differs only little from the "Solar" composition and that plots on that line is considered terrestrial while composition that are clearly off that line are indicative of an extraterrestrial origin. As can be seen, the measured impact debris has isotopic compositions of Si and Mg that are essentially terrestrial. The degree of Mg fractionation is also much smaller than the range observed in IDPs collected in the stratosphere, whose compositions are shown for comparison.
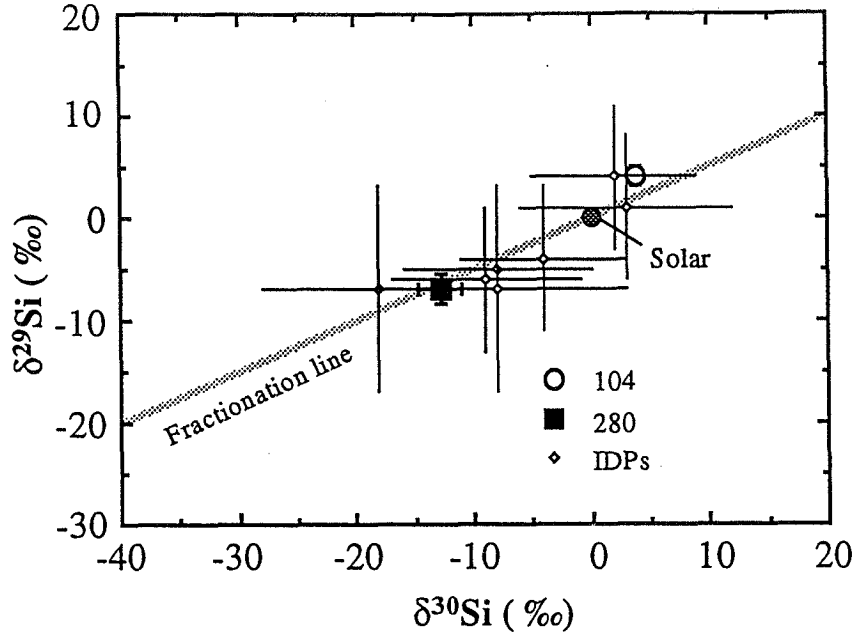
Figure 11: Three-isotope-plot of the Si isotopic compositions of impact deposit and those of Interplanetary Dust Particles (IDPs). The errors shown are 1σ.

Unfortunately, the isotopic analysis of projectile material in extended impacts on germanium plates from experiment AO187-2 is extremely difficult. The reason is the thinness of the impact deposits. An exception is impact C02-2-17C-1, where several solid fragments were found on the rim of the impact feature. The results of the Mg and Si isotopic analysis of these fragments are shown in Figures 12, 13, and Table 1. The isotopic compositions of the fragments plot close to the terrestrial values. Here too, the measured isotopic compositions do not have an identifiably extraterrestrial signature.

	$\delta^{25}Mg$ (‰)	$\delta^{26}Mg$ (‰)	$\delta^{29}Si$ (‰)	$\delta^{30}Si$ (‰)
Fragment a	30 ± 13	17 ± 9	-2 ± 14	6 ± 21
Fragment b	13 ± 12	13 ± 9	-6 ± 13	14 ± 17
Fragment c	-2 ± 10	-10 ± 10	-14 ± 13	-16 ± 16
Fragment d	-1 ± 7	28 ± 10	9 ± 12	-11 ± 12
Fragment e	10 ± 11	-7 ± 12	-8 ± 14	27 ± 17
Fragment f	-24 ± 8	-6 ± 8	3 ± 10	7 ± 9

Table 1. Results of the Mg and Si isotopic measurements of individual fragments on the rim of impact C02-2-17C-1. The errors are 1σ.
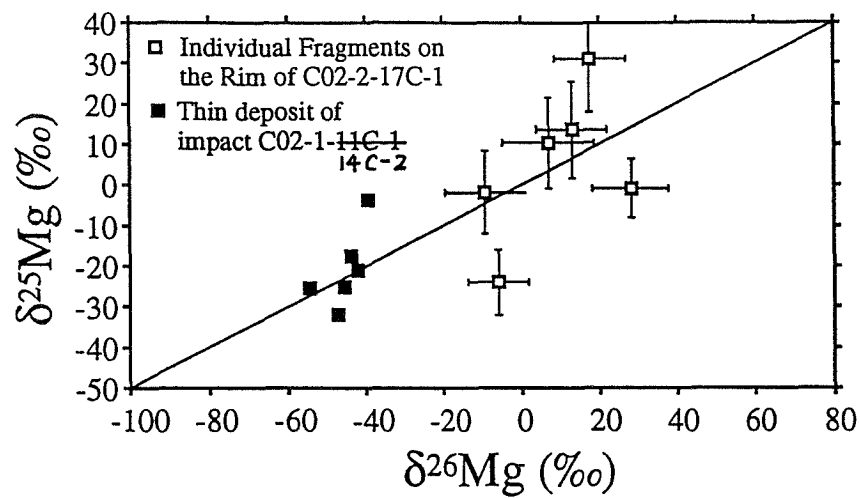
Figure 12. Three-isotope-plot of the results of the Mg isotopic measurements of fragments on the rim of impact C02-2-17C-1 and of deposits in the extended impact C02-1-14C-2. The errors shown are 1 σ and the diagonal line is the Terrestrial Fractionation Line.
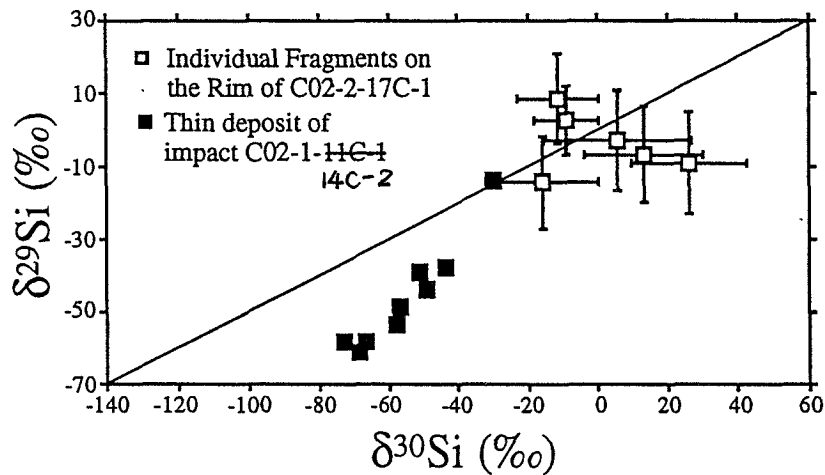
Figure 13. Three-isotope-plot of the results of the Si isotopic measurements of fragments on the rim of impact C02-2-17C-1 and of deposits in the extended impact C02-1-14C-2. The errors shown are 1 σ and the diagonal line is the Terrestrial Fractionation Line.

Impact C02-2-17C-1 was the only case of an extended impact from experiment AO187-2 in which we found projectile fragments that had apparently survived the impact. In contrast to the isotopic analyses of these fragments are the analyses of a thin debris layer from impact C02-1-14C-2 (Figures 12 and 13). Here both the Mg and Si isotopic data show large negative (shifts to the lower left, *i.e.* toward more negative δ-values) mass fractionation effects; in addition, the Si data show substantial deviations from the terrestrial mass fractionation line.

A more detailed analysis of these data revealed that these large fractionations and the deviations from the fractionation line are not genuine isotopic effects in the measured material but are artifacts resulting from the small thickness of the impact deposits. Because the layer of deposited projectile is sputtered away during SIMS analysis, the secondary ion signal from a thin layer is not constant but decreases rapidly as a function of time. Since the isotopes of Mg and Si are measured in sequence, the non-linear nature of this decrease can produce the effects shown by the C02-1-14C-2 data. High throughput (large magnet), multiple collector SIMS instruments capable of accurate isotopic measurements are currently being developed for the study of extraterrestrial materials (K. McKeegan, UCLA, private communication). Such instruments may have the required sensitivity and measurement capabilities to permit isotopic measurements of very thin impact deposits.

The extended impacts of LDEF experiment A0187-2 that have already been partially studied by existing SIMS techniques *represent an extremely important scientific resource for future work.* In particular, some of these impacts may make it possible to measure the isotopic composition of cometary material. Dust particles from long-period comets encounter the earth with very high velocities and are thus preferentially destroyed relative to slower, asteroidal particles during atmospheric entry (ref. 8). Cometary particles may thus be grossly under-represented in the stratospheric micrometeoroid collections. In contrast, high velocity particles produce extended impacts with high efficiency and should thus be well represented in the existing collection of capture cell impacts.

Because of their potential scientific importance, continued care should be taken to store the relevant surfaces of experiment AO187-2 under clean conditions so they may be properly analyzed by future, improved analytical instruments.

REFERENCES

1. Amari S., Foote J., Simon C., Swan P., Walker R.M., Zinner E., Jessberger E.K., Lange G., and Stadermann F.J.: SIMS chemical analysis of extended impact features from the trailing edge portion of experiment A0187-2. Proceedings of First LDEF Post-Retrieval Symposium, NASA CP 3134, 503-516, 1991.

2. Amari S., Foote J., Swan P., Walker R.M., Zinner E., and Lange G.: SIMS chemical analysis of extended impacts on the leading and trailing edges of LDEF experiment A0187-2. Proceedings of Second LDEF Post-Retrieval Symposium, NASA CP 3194, 513-528, 1993.

3. Bernhard R.P., See T.H., and Hörz F.: Projectile composition and modal frequencies on the "Chemistry of Micrometeoroids" LDEF experiment. Proceedings of Second LDEF Post-Retrieval Symposium, NASA CP 3194, 551-573, 1993.

4. Anders E. and Grevesse N.: Abundances of the elements: Meteoritic and solar. Geochimica et Cosmochimica Acta, 53, 197-214, 1989.

5. Stadermann F. J.: Rare earth and trace element abundances in individual IDPs. Lunar and Planetary Science, XXII, 1311-1312, 1991.

6. McKeegan K. D.: Ion microprobe measurements of H, C, O, Mg, and Si isotopic abundances in individual interplanetary dust particles. Ph. D. Thesis, Washington University, St. Louis, 187 pp, 1987.

7. Stadermann F. J., Walker R. M., and Zinner E.: Ion microprobe measurements of nitrogen and carbon isotopic variations in individual IDPs. Meteoritics, 24, 327, 1989.

8. Flynn G. J.: Atmospheric entry heating: a criterion to distinguish between asteroidal and cometary sources of interplanetary dust. Icarus 77, 287-310, 1989.

Abstracts of the 53rd Meeting of the Meteoritical Society
Perth, Western Australia, 17–21 September 1990

Ion probe studies of SiC from different chondrite groups. C. M. O'D. Alexander,[1] C. Prombo,[1] R. M. Walker,[1] E. Zinner[1] and J. W. Arden.[2] [1]McDonnell Center for the Space Sciences, Washington University, St. Louis, MO 63130, USA. [2]Dept. Earth Sciences, Oxford University, Oxford OX1 3PR, UK.

Here we give new results from our continuing survey of SiC in primitive meteorites. Previously we reported C and Si isotopic data for SiC grains in acid residues of the UOCs Krymka and Inman (1) that indicated differences exist in the isotopic composition of SiC both within the ordinary chondrites and between the CMs and UOCs. Subsequently we have analysed a further four UOCs (Tieschitz, Bishunpur, Chainpur and Semarkona) as well as the CV3 chondrite Leoville.

In Murchison the Si isotopic compositions are arrayed along a slope one line and seem to cluster into four groups that are delineated in Figs. 1 and 2. In terms of their Si isotopes the grains in Bishunpur and Chainpur (Fig. 1) show a similar spread in values as in Murchison but no apparent clustering. In contrast, the anomalous grains in Semarkona and Tieschitz show a more restricted range of Si compositions than in Murchison.

In general, the range of C isotopic compositions in UOC SiCs is similar to that in Murchison but with different distributions. For instance, in Chainpur the C isotopes are, on average, more ^{13}C enriched than in Murchison with 12 of the 36 grains analysed so far having $\partial^{13}C \geq 1000‰$ compared with only 10 out of 89 grains in Murchison. On the other hand, in Bishunpur, as is the case for the Si isotopes, the carbon isotopes show a similar distribution as in Murchison.

In four of the seven meteorites studied some fraction of the SiC grains is isotopically normal. Leoville (Fig. 2) seems to contain the greatest proportion of this 'normal' SiC; indeed, we have found only 2 isotopically anomalous grains out of 20 analysed. The normal isotopic compositions suggest these grains may have formed within the solar system. However, at present we cannot rule out the possibility of terrestrial contamination. Experiments are in progress to resolve this issue.

Our results reinforce the evidence for both intragroup and intergroup variations of the isotopic composition of SiC in primitive meteorites. However, it remains to be determined whether this is due to differences in sample preparation, nebular processing, or nebular heterogeneity. Reference: (1) Alexander et al. (1990) LPSC 21, 9–10.

Oxygen isotopic compositions of oxide grains in Semarkona. C. M. O'D. Alexander,[1] E. Zinner[1] and J. W Arden.[2] [1]McDonnell Center for the Space Sciences, Washington University, St. Louis, MO 63130, USA. [2]Dept. Earth Sciences, Oxford University, Oxford OX1 3PR, UK.

Oxygen is unique amongst the major rock-forming elements in exhibiting in a large size range of objects isotopic anomalies that cannot be explained in terms of mass fractionation or radioactive decay. In chondrites these variations are thought to result from exchange between isotopically distinct gas and solid (or liquid) reservoirs. For instance, it appears that refractory inclusions in carbonaceous chondrites were initially very ^{16}O-rich and that subsequently the minerals in them exchanged, to a greater or lesser extent, with a gaseous reservoir which had an isotopic composition that lay close to the terrestrial fractionation line (1). Allende chondrules show evidence for a similar exchange (2).

In the ordinary chondrites chondrules also show evidence for isotopic exchange (2, 3) but in their case it seems that, while the gaseous reservoir was similar to that in the carbonaceous chondrites, the solid material was ^{16}O-depleted (3). However, this model appears inconsistent with the positive 'correlation' between the degree of ^{16}O-depletion in the bulk meteorite and oxidation state, since presumably the most oxidised meteorites have experienced the greatest degree of exchange with the gas.

In an attempt to elucidate the nature of the oxygen reservoirs sampled by ordinary chondrite material we have analysed the oxygen isotopic composition of acid resistant mineral grains (that included spinel, chromite, TiO_2 and hibonite) from a Semarkona residue (Fig.). Despite the scatter in the data and with the exception of two hibonite grains the minerals plot near the composition of the putative gaseous reservoir rather than the ^{16}O-depleted solid reservoir. Large Cr-spinel grains from the Murchison matrix have, within the accuracy of our technique, identical isotopic compositions (4).

The composition of the hibonites are as extreme as those from carbonaceous chondrites (5, 6). It is as yet uncertain whether refractory inclusions in ordinary and carbonaceous chondrites share a common source. Nevertheless, it appears that the precursor materials had similar oxygen isotopic compositions. In the carbonaceous chondrites the bulk of the solid material is also thought to have been initially ^{16}O-rich. It is, therefore, puzzling that the bulk of the ordinary chondrite material was ^{16}O-depleted. References: (1) Clayton et al. (1977) EPSL 34, 209–224. (2) Clayton et al. (1983) In Chondrules and Their Origins, pp. 37–43. (3) Clayton et al. (1983) Meteoritics 18, 282. (4) Grossman et al. (1988) LPS 19, 435. (5) Fahey et al. (1987) Ap. J. 323, L91. (6) Ireland and Zinner (1989) Meteoritics 24, 279.

Micrometeoroid experiment on the long duration exposure facility. S. Amari,[1] J. Foote,[1] C. Simon,[1] P. Swan,[1] R. Walker,[1] E. Zinner[1] and E. K. Jessberger.[2] [1]McDonnell Center for the Space Sciences and Physics Department, Washington University, St. Louis, MO 63130, USA. [2]Max-Planck-Institut für Kernphysik, Heidelberg, W. Germany.

The Long Duration Exposure Facility (LDEF) was returned to earth in January after 5.8 yr in space. Experiment A0187-2 consisted of 237 "capture cells" (total area 2.1 m²), each consisting of polished Ge plates

Fig. 1 Chainpur (L/LL3)

Fig. 2 Leoville (CV3)

○ Spinel-chromite-TiO₂
● Hibonite
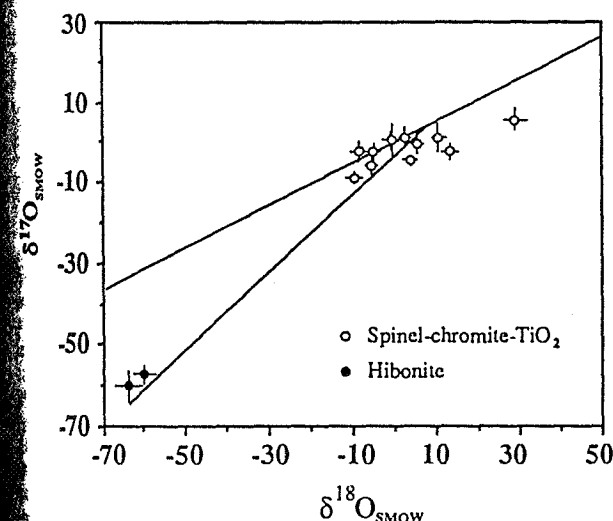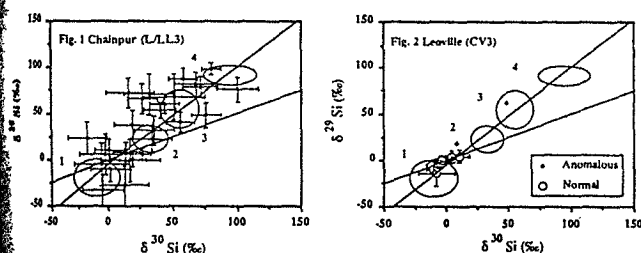
separated by 200 μm from thin (2 μm) mylar "entrance" foils coated on one side with 1000 Å of Ta and on the other with 100 Å of Au-Pd. Half of the cells were mounted on the leading edge (facing forward direction) of LDEF and the rest on the trailing edge. Laboratory impact experiments have demonstrated that debris and vapor deposits from impacts can be collected and analyzed by ion probe techniques on both the plastic foil and the Ge plate (1, 2). For unknown reasons, most of the plastic foils failed during flight; however, 12 cells on the trailing edge are intact. Numerous impacts, ranging in size from those that are visible to the naked eye to submicroscopic, are found on both the leading and trailing edges. Preliminary SEM scanning of one plate on the leading edge at 300× gives a density of ~60 cm² for craters >1 to 2 μm in size. The crater density is much lower on the trailing edge due to the differences in the average velocities of impacting particles caused by the orbital motion of LDEF. Impact craters on the trailing edge surfaces are also distinctly different than those on the leading edge, being more subdued and in some cases containing an abundance of Ta fragments. Three types of impacts are found on the Ge: 1) craters with "jagged" morphologies reflecting the brittle nature of Ge, 2) "spider webs" consisting of myriads of small craters arranged in complex patterns (3), and 3) features consisting of one or more larger craters in a spray of smaller craters. Type 2 and 3 features are produced by impactors that have undergone varying degrees of disruption in traversing the entrance foils. Their prevalence demonstrates that the plastic foils remained intact for considerable periods of time, even on the leading edge. Also seen are circular features with dendritic crystals in the center, probably caused by very low velocity impacts of partially liquid droplets of human, not cosmic, origin. Results of the initial analysis of a representative set of impacts will be presented at the meeting. References: (1) Jessberger E., Kuczera H., Lange G., Sutton S. and Zinner E. (1985) *LPSC* 16, 400–401. (2) Lange G., Eigner S., Igenbergs E., Jessberger E. K., Kuczera H., Maas D., Sutton S. and Zinner E. (1986) *LPSC* 17, 456–457. (3) Fechtig H., Horz F., Igenbergs E., Jessberger E., Kuczera H., Lange G., Pailer N., Sutton S., Swan P., Walker R. and Zinner E. (1985) In *Properties and Interactions of Interplanetary Dust* (eds. R. H. Giese and P. Lamy), pp. 121–126. Reidel.

Interstellar SiC and its origins. II. Ne-E without Na²², and other surprises. Sachiko Amari, Roy S. Lewis and Edward Anders. Enrico Fermi Institute and Dept. of Chemistry, Univ. of Chicago, Chicago, IL 60637-1433, USA.

Our new SiC size fractions (1) have very high noble-gas concentrations (e.g., He⁴ to 0.11 ml/g, Ne_E^{22} to 35 000 × 10⁻⁸ ml/g, Xe¹³⁰ to 1100 × 10⁻¹⁰ ml/g), exceeding those of previous separates (2, 3) by ~3–10×. As most previous samples were >90% pure SiC, the reason is not higher purity but presumably loss of gas-rich grains or surface layers in the earlier separations, either by chemical etching or by mechanical abrasion. He and Ne concentrations rise slightly with increasing grain size, peaking at ~1 μm, whereas Kr stays flat and Xe declines. Elemental and isotopic ratios show regular trends, and usually lie between the values calculated (4, 5) for the He-burning shells and envelopes of AGB (asymptotic giant branch) carbon stars. The example in Table 1 refers to a 1.5 M⊙ star of metallicity Z = 0.009 and C/O = 1 (4).

This match has important implications for the origin of Ne-E(H). The Ne in AGB star He-shells (4) actually is closer to pure Ne²² than the Ne in SiC (Table 1), and thus could serve as the sole source of Ne-E, without any help from Na²². Lacking non-volatile progenitors, He⁴ and Kr⁸² must have been trapped by ion implantation, and since He⁴/Ne_E²² and Ne²²/Kr⁸² ratios do not exceed those in the star, *there is no room for additional contributions by Na²²*. At least Ne-E(H) may be "parentless," nucleosynthetic Ne.

The new samples still contain excess—presumably cosmogenic—Ne²¹ relative to He-shell values (Table 1). Cosmic-ray exposure ages, calculated as before (2, 3, 6), range from 27 to 135 Ma, compared to the previous mean of ~40 Ma. The ages correlate with Ne²² content and with severity of the chemical treatment, suggesting that the samples are mixtures of gas-rich, old, reactive (radiation-damaged?) grains, and gas-poor, young, resistant grains (degassed during formation of the solar system?). The true age of the old grains thus must be higher than the age of the bulk samples, perhaps approaching the theoretical age of ~400 Ma. Acknowledgement: We thank R. Gallino and colleagues for making available to us their s-process calculations. References: (1) Lewis R. S., Amari S. and Anders E. (1990) *Meteoritics* 25, 379. (2) Amari S. and Lewis R. S. (1989) *Meteoritics* 24, 247–248. (3) Zinner E., Tang M. and Anders E. (1989) *GCA* 53, 3273–3290. (4) Gallino R., Busso M., Picchio G. and Raiteri C. M. (1990) *Nature* 348, 298–302. (5) Lewis R. S., Amari S. and Anders E. (1990) *Nature* 348, 293–298. (6) Tang M. and Anders E. (1988) *Astrophys. J.* 338, L31–L34.

TABLE 1.

Sample	Size (μm)	$\dfrac{He^{3a}}{He^4}$	$\dfrac{He^4}{Ne^{22}}$	$\dfrac{Ne^{20}}{Ne^{22}}$	$\dfrac{Ne^{21b}}{Ne^{22}}$	$\dfrac{Ne^{22}}{Kr^{82}}$	$\dfrac{Kr_s^{80}}{Kr_s^{82}}$	$\dfrac{Kr_s^{86}}{Kr_s^{82}}$	$\dfrac{Xe^{130}}{Xe^{132}}$
KJB	0.1–0.2	2.00	763	0.893	7.7	1560	0.050	0.65	0.360
KJC	0.2–0.3	1.48	618	0.636	9.1	2800	0.044	1.13	0.360
KJD	0.3–0.5	1.16	478	0.459	10.7	4600	0.040	1.76	0.356
KJE	0.5–0.8	0.81	372	0.298	12.8	6700	0.036	2.42	0.346
He-shell (4)		~0	384	0.073	5.4	13 800	0.036	2.28	0.41
Envelope (4)		9.6	10 600	5.76	142	18 000	0.056	1.77	0.25

ᵃ ×10⁻⁴.

ᵇ Extrapolated to Ne²⁰/Ne²² = 0.04 along trends defined by the data; ×10⁻⁴.

Two types of interstellar carbon grains in the Murchison carbonaceous chondrite. S. Amari,[1,2] E. Zinner[2] and R. S. Lewis.[1] [1]Enrico Fermi Institute and Department of Chemistry, University of Chicago, Chicago, IL 60637, USA. [2]McDonnell Center for the Space Sciences and the Physics Department, Washington University, St. Louis, MO 63130, USA.

The carrier of Ne-E(L), Cα, consists of dense, round grains of carbon, 1–6 μm in diameter (1, 2), ranging from well crystalized graphite to "more organic" compositions and with ¹²C/¹³C ratios from 8 to 4500 (2). Noble gas data on density fractions indicate that there are at least two types of Cα that differ in the release temperature of Ne-E(L) (3, 4).

In order to establish whether these two types also differ in their chemical and C-isotopic properties, we analyzed round grains from two density separates (4) in the ion microprobe: from KFA1 (density = 2.05–2.10 g/cm³, ²²Ne-E(L) = 13 000 × 10⁻⁸ cm³/g, two Ne-E release peaks at 600 °C and 800–900 °C) and KFC1 (density = 2.15–2.20 g/cm³, ²²Ne-E(L) = 5150 × 10⁻⁸ cm³/g, only one release peak at 900 °C). Although both separates contain grains with isotopically light and heavy carbon, they have markedly different distributions (Fig. 1): while KFA1 consists mostly of isotopically heavy (a total of 16) and normal grains (12) with fewer light grains (7), KFC1 consists predominantly of light grains (39), with only few heavy (8) and normal (3) ones. The range of ¹²C/¹³C in both separates is the same as that observed previously in Murchison separate LFC1 (2), except for one KFC1 grain with ¹²C/¹³C = 4.12 (δ¹³C = +20 590 ± 160‰).

Zinner et al. (2) noted that isotopically heavier grains have higher H, N and Si contents than light ones. Thus, the first type, Cα1, appears to consist of heavy carbon of lower density with generally higher contents of other elements, that outgasses at lower temperature (also evidenced

SIMS ANALYSIS OF MICROMETEOROID IMPACTS ON LDEF;

S. Amari[1], J. Foote[1], E. K. Jessberger[2], C. Simon[1], F. Stadermann[2], P. Swan[1], R. M. Walker[1] and E. Zinner[1], [1]McDonnell Center for the Space Sciences and Physics Dept., Washington University, One Brookings Drive, St. Louis, MO 63132, [2]Max-Planck-Institut für Kernphysik, Postfach 103980, D6900, Heidelberg, Germany.

LDEF experiment AO187-2 consisted of 237 capture cells, 120 on the leading edge, the rest on the trailing edge. In each cell a 2 µm plastic foil, metallized on both sides, covered polished Ge targets. Although all plastic covers except for 12 cells on the trailing edge failed during flight, the Ge plates contain many extended impact features that were apparently produced by projectile material that had penetrated the plastic foils while they were still intact. We optically scanned all cells without plastic foil from the trailing edge and found extended impact features from 200 to 4000 µm in diameter with 4 characteristic morphologies: a. craters surrounded by deposits, b. ring-shaped features, c. sprays, and d. "spider webs." 53 impacts were selected as high priority candidates for ion probe analysis. After detailed documentation in the SEM impacts were analyzed in the ion microprobe for the chemical composition of the remaining projectile material. Prior simulation studies [1] had shown that extended impact on the Ge plates contained sufficient projectile material for chemical and isotopic analysis by SIMS. We made multi-element point analyses in lateral scans across the impact features. Each point analysis consisted of depth profiles of a number of elements. In all of 12 impacts so far studied we found evidence for the presence of projectile material in the form of elemental enhancements in the impact region, in 5 cases significant amounts of projectile material were detected. One such analysis is shown in Figs. 1 and 2. Fig. 1 shows ion signals of different isotopes normalized to the ^{76}Ge signal for a scan across a "spider web" impact. In Fig. 2 the selected signals of ^{27}Al, ^{28}Si, ^{40}Ca, ^{48}Ti and ^{56}Fe were normalized with relative sensitivity factors determined from laboratory studies [1] to obtain elemental abundance ratios relative to Mg. Their abundances indicate an extraterrestrial origin except for Si, which is anomalously high and is probably dominated by contamination from RTV glue used to bond the Ge plates to the Al substrate. Enough material is present to allow isotopic measurements, which will be reported at the meeting.

[1] Lange G. et al . (1986) Lunar Planet. Sci. XVII, 456.
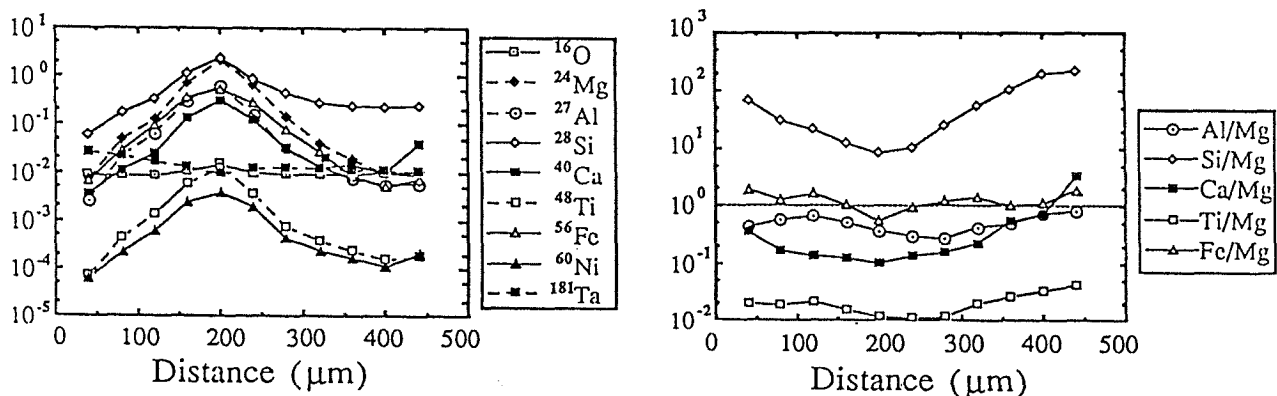
Distance (µm)   Distance (µm)

SIMS CHEMICAL ANALYSIS OF EXTENDED IMPACTS ON THE LEADING AND TRAILING EDGES OF LDEF EXPERIMENT AO187-2.

S. Amari[1], J. Foote[1], C. Simon[1], P. Swan[1], R. M. Walker[1], E. Zinner[1], E. K. Jessberger[2], G. Lange[2], and F. Stadermann[2]. [1]McDonnell Center for the Space Sciences and the Physics Department, Washington University, One Brookings Drive, St. Louis, MO 63130-4899. [2]Max-Planck-Institut für Kernphysik, Postfach 103980, D-6900 Heidelberg, Germany.

Experiment AO 187-2 on LDEF consisted of 237 capture cells each 8.6 x 9.4 cm in size. Each cell consisted of four polished high purity Ge target plates, 42 x 39 x 0.5 mm, covered with a 2.5 μm thick mylar cover foil spaced 200 μm from the Ge plates. The mylar was coated with 1000 Å of Ta on the side facing the Ge to facilitate ion-probe analysis, and was coated with 100 Å of Au-Pd on the top (space-facing) side to inhibit space erosion of the plastic. 120 cells were mounted in a tray on the leading edge of the spacecraft and 117 cells were mounted in portions of two separate trays on the trailing edge. Following the return of LDEF to earth after a much longer mission than originally planned, it was found that most of the plastic cover foils had failed. All of the foils on the leading edge were gone and only twelve cells on the trailing edge were still intact.

However, optical microscope and SEM examination showed that many of the bare cells on both the leading and trailing edges possessed numerous "extended impacts" that must have been caused by the clouds of debris formed when incoming particles traversed foils that were still intact at the time of impact. Our initial efforts have focussed on the ion probe study of extended impacts on the trailing edge cells that had lost their plastic foils. As described in more detail in a paper presented at the First LDEF Post-Retrieval Symposium [1], some 53 candidate impacts were found by optical scanning of 116 cells on the trailing edge. Successful ion probe analyses using our modified CAMECA IMS 3f instrument have now been performed on 40 of these impacts. Lateral scanning profiles across these impacts were made by rastering an O⁻ primary ion beam of 1-2 nA over an area 40 μm x 40 μm and then stepping across the impact. Multi-element depth profiles were obtained at each analysis site by cycling through a series of isotopic masses. Individual depth profiles were then integrated from cycles 3 to 20 to obtain an integrated secondary ion count for each point in a lateral traverse. Although the ion signals did not match perfectly the appearance of the impacts as seen in the SEM, projectile debris material could be detected in almost every impact (see Fig. 1). We found that the ratios of different elements were somewhat variable across individual lateral traverses – either due to inhomogenities in the projectiles themselves or to variable segregation of elements in the impact and collection processes. Rather than attempting to integrate the data across a single lateral traverse of a complex impact structure, we choose to report element ratios determined from the peak values seen in a traverse. Ion counts are converted to elemental ratios using the sensitivity factors previously determined on four glass standards [2].

Histograms of the ratios of Al, Fe, and Ti relative to Mg for 40 impacts are shown in Fig. 2. It can be seen that the distribution of values for the impact projectiles overlap those previously determined for IDPs [3] as well as average chondritic ratios. However, the average ratios for the LDEF impacts are systematically higher for the refractory elements Al, Ca, and Ti than those for either chondrites or IDPs. Conversely, the Fe/Mg ratios are systematically lower. Comparison of these data with earlier elemental fractionation trends obtained from studies of laboratory impacts of standard glasses [2] led us to suggest [1] that many of the apparent differences could be attributed to selective volatilization and redistribution of elements between the projectile as it existed in space and the deposits that are measured. The new data are consistent with the earlier results and can be similarly interpreted. However, it should be noted that the required elemental fractionation exceeds that previously measured (or extrapolated) for laboratory impacts and a difference between the interplanetary particles studied here and IDPs cannot be excluded. In particular we note that Ca depletions which have been observed for IDPs [4] do not seem to be reflected in the LDEF impacts.

Optical scanning of the bare leading edge cells also shows many extended impacts. Although this demonstrates that the cover foils remained intact for some time after the deployment

of LDEF, further analysis will be required to assess the value of the leading edge cells for the study of cosmic dust and/or orbital debris. A preliminary analysis of 7 front bside impacts suggests that most of them are due to space debris and not micrometeoroids. A new SIMS system for the analysis of impact material based on ion imaging of elements in the ion probe is currently under development.

References: [1] S. Amari *et al.* (1991) *Proc. 1st LDEF Post-Retrieval Symp.*, in press. [2] G. Lange *et al.* (1986) *LPS* **XVII**, 456. [3] F. Stadermann (1991) unpublished data. [4] L. S. Schramm *et al.* (1989) *Meteoritics* **24**, 99.

Fig. 2

E03-1-40B-1
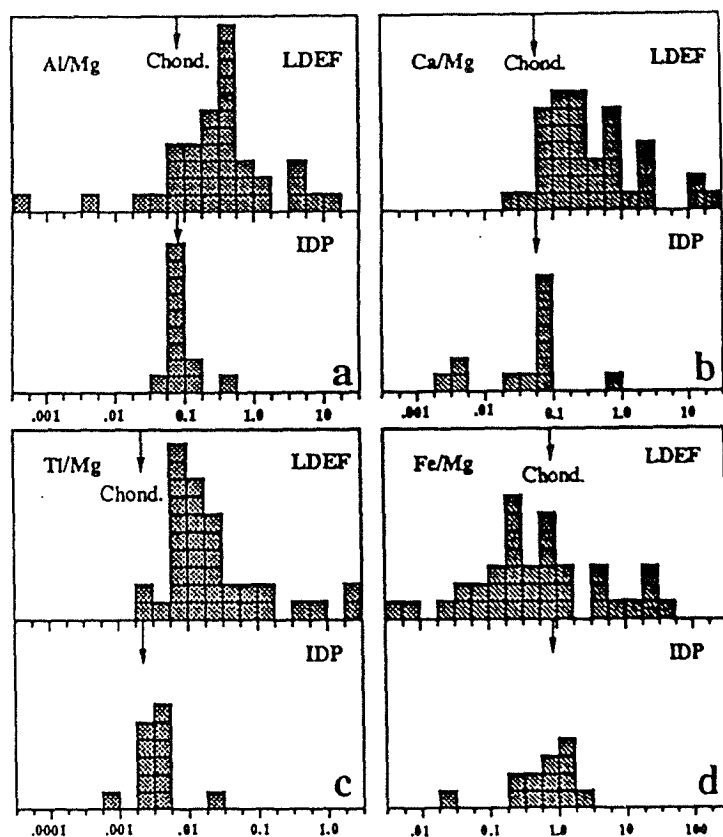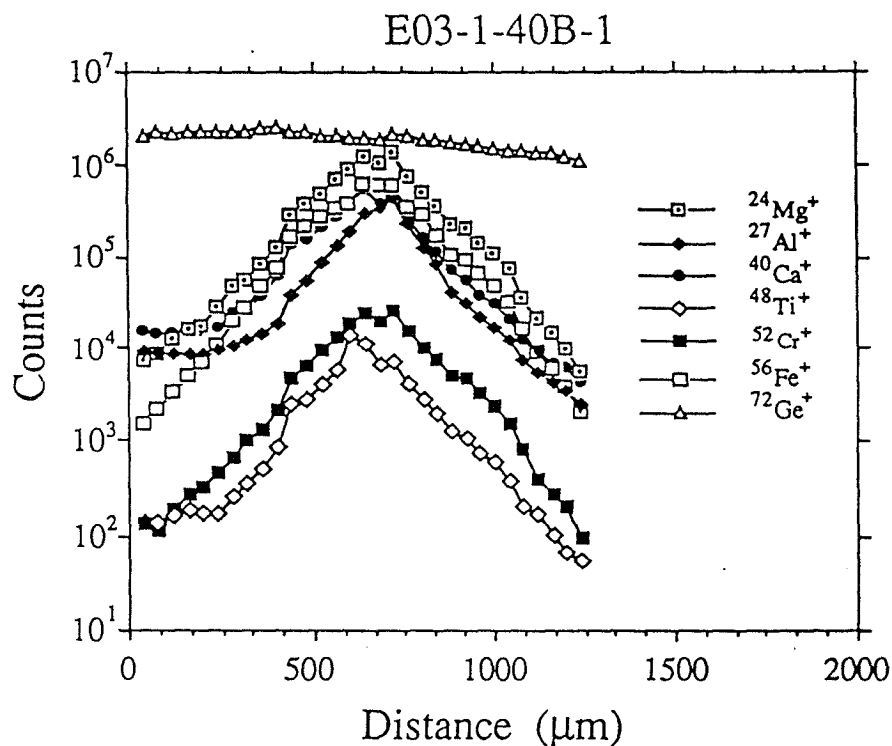
Fig. 1

TRAJECTORY CALCULATION OF INDIVIDUAL PARTICLES FROM LDEF IMPACTS;

F. J. Stadermann, TH Darmstadt, Hilpertstr. 31 (Geb. H); 64295 Darmstadt, Germany.

The capture cells from LDEF experiment A0187-2 were designed to determine the number and the chemical composition of particles that impacted the surface of the satellite. During routine investigations elliptical discolorations of the target material were observed adjacent to impact features. In a method demonstrated here, these elliptical features are interpreted as results of erosion by atomic oxygen through holes in a cover foil. Based on this assumption, it becomes possible to determine the pre-impact trajectories of individual particles in addition to their original chemical composition. What makes this method particularly intriguing is the fact that it was unexpected and that the experiment was not specially designed for this kind of investigation. It is the *only* experiment on LDEF that offers this kind of combined trajectory and chemistry information of individual particles.
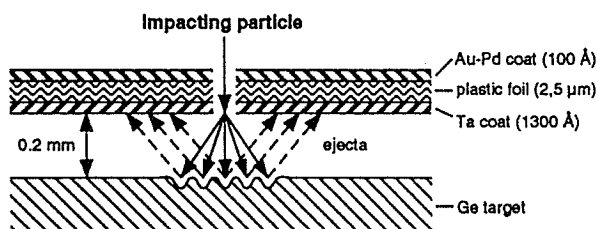
Figure 1: Schematic of LDEF capture cell experiment A0187-2.

INTRODUCTION. The LDEF experiment A0187-2 consisted of germanium target plates and a thin plastic foil, separated by 200 μm (Fig. 1). Impacting particles were partly disrupted and decelerated while passing through the foil and fragments of the particle were then collected both on the germanium plate and the back side of the foil. The extended impact features found on the germanium plates have typical diameters of several hundred μm, although the sizes of the corresponding projectiles (and of the holes in the foil) are only around 10 μm. Secondary ion mass spectrometry was then used to determine the composition of impact deposits and to infer the origin (natural or man-made) of individual particles [1]. Several extended impacts are accompanied by elliptical features (discolorations) of unknown origin on the target plate [2]. These elliptical features have diameters of around 400 μm and are always directly adjacent to or overlapping impact features. Although trays from experiment A0187-2 with identical setups were located on various differently oriented LDEF surfaces, the elliptical features are only found on tray E08 on the leading edge. On this leading edge tray none of the cover foils survived the extended exposure of the satellite, but at

Figure 2: Schematic of an impact event on tray E08 through the cover foil. The orientation of tray E08 relative to the LDEF flight direction is shown in the insert.

the time of the impacts the foils must still have been intact. The elliptical features may be explained as surface erosion effects by atomic oxygen *through the impact holes* in the foils at a time when the latter were still intact. Based on this assumption it is possible to determine (a) the exact positions of the impact holes in the foils, (b) the actual distances of the foils from the germanium plates, and (c) the trajectories of individual projectiles upon impact.

GEOMETRIC CONSIDERATIONS. The LDEF satellite was exposed to atomic oxygen, which hit the surface with a collision energy of 4-5 eV almost directly from the forward (ram) direction. Tray E08 was facing sideways from the leading edge at an angle of 30° as shown in Figure 2. Oxygen atoms entering the capture cell through an impact hole from ram direction spread inside in the shape of a circular cone (Fig. 3). The vertex of this cone corresponds to the hole in the foil, which is assumed to be significantly smaller than the features on the target plate. The area where this cone intersects with the surface, *i.e.*, where the oxygen atoms collide with the germanium has the

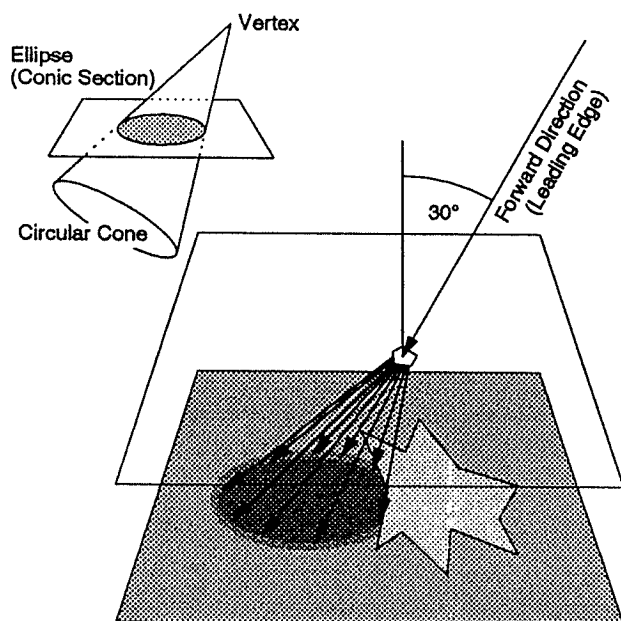TRAJECTORY CALCULATION OF INDIVIDUAL PARTICLES FROM LDEF IMPACTS: Stadermann F. J.

Figure 3: Schematic of cone-shaped distribution of atomic oxygen inside the capture cell and geometric interpretation of the elliptical feature as a conic section.

shape of an ellipse. The visible discolorations on the target show the range of physical or chemical reactions between atomic oxygen and germanium. Since all foils on the leading edge failed eventually, the entire surface (also outside of the ellipses) was subject to atomic oxygen at the end of the flight. Therefore the ellipses can only be understood as temporal features due to the longer exposure.

Mathematically an ellipse in a plane can be expressed as a conic section from a circular cone. With one additional piece of information – either the direction of the axis of the cone or the distance of the vertex from the surface – the cone's geometric properties can unambiguously be determined. After the location of the vertex of the cone (*i.e.*, the location of the penetration hole in the foil) has been calculated, the original trajectory of the particle before the impact can be calculated. For this the approximate location of the center of the impact feature has to be determined arbitrarily. The assumption that the 'center of gravity' of the visible extended impact feature lies on the extrapolated line of original particle trajectory may be a good first order approximation. From this information the impact angles α and ϑ (as shown in Fig. 4) can be calculated.

CONCLUSIONS. The method demonstrated here appears to be a viable way to determine individual particle trajectories from a record stored in the impact and oxygen erosion features on germanium targets from LDEF experiment A0187-2. It is possible to calculate particle trajectories *relative to LDEF* and – since LDEF was stabilized in its orbit – *relative to the Earth*. This information is not sufficient to determine individual projectile origins in the solar system by simply tracing back individual trajectories, because no information on the *timing* of the impacts is available. However, it is possible to distinguish between circular and elliptical orbits, and different entrance angles into the atmosphere. All this information can then be correlated with the measurements of the chemical compositions of the same particles and, thus, lead to a comprehensive understanding of individual particle histories. In previous studies [1, 2] the distribution of different extended impact features could not be explained, nor

Figure 4: Geometry of impact angles α and ϑ from projectile trajectory.

could the directions of the impacts be determined from the observed features on the germanium. A detailed analysis of the impacts with ellipses may lead to a better understanding of the extended impact features and may make it possible to deduce the approximate angle of impact solely from the shape of the impact feature. Once this step is reached, the study of individual particle trajectories can be extended to all impacts on germanium – even on the trailing edge. This would lead to the most complete database of particle trajectories and chemistry on LDEF.
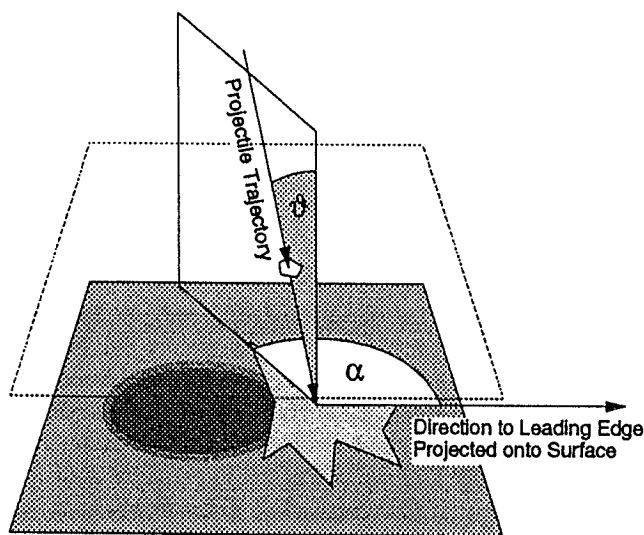
REFERENCES. [1] Amari S. et al. (1992) Proc. 1st LDEF Post-Retrieval Symposium [2] Amari S. et al (1993) Proc. 2nd LDEF Post-Retrieval Symposium

Interstellar oxide grains from the Tieschitz ordinary chondrite

L. R. Nittler, C. M. O'D Alexander, X. Gao, R. M. Walker & E. K. Zinner

McDonnell Center for the Space Sciences and Department of Physics, Washington University, One Brookings Drive, St. Louis, Missouri, 63130-4899, USA

MOST material in the Solar System has an isotopic composition that represents an average of the different stars that contributed material to the protostellar cloud. Primitive meteorites, on the other hand, preserve grains that retain the isotopic signatures of their individual stellar sources[1] and thus provide valuable insight into stellar and galactic evolution, nucleosynthesis, and solar nebular processes. A large number of pre-solar silicon carbide, graphite and diamond grains have now been isolated[1,2], but only three interstellar oxide grains have hitherto been recovered[3-7], even though oxygen-rich stars are believed to be the dominant source of dust in the Galaxy[8,9]. We report here the isolation of 21 interstellar oxide grains from the Tieschitz meteorite. The grains exhibit a wide range of oxygen isotope compositions, indicating that they originated in several distinct stellar sources having different masses and initial compositions. There is also evidence for the presence of the short-lived radionuclide ^{26}Al in nine of the grains at the time they formed. Although the isotopic compositions of many of the grains are consistent with both observations and theoretical models of oxygen-rich red giant stars, a significant fraction have no observed stellar counterpart.

Different isotopes are produced by a variety of nucleosynthetic processes, and the isotopic ratios in interstellar grains can therefore provide insight into the types of stellar sites that produced them. Here we determine the isotopic compositions of 21 inter-

stellar oxide grains isolated from the Tieschitz meteorite, and compare these values to astronomical observations and theoretical models of stellar evolution.

A sample of the Tieschitz (H/L 3.6) ordinary chondrite was physically and chemically processed to produce a residue[10,11], T8, in which chemically-resistant oxide phases were concentrated by a factor of $\sim 2.5 \times 10^5$. For ion microprobe analysis, a suspension of T8 was deposited on a gold foil[12] along with grains of the Burma Spinel oxygen isotope standard. To automatically locate rare interstellar oxides, a Photometrics CCD (charge-coupled device) camera was coupled to the microchannel plate/fluorescent screen of the modified Cameca IMS-3F ion microprobe[4] at Washington University. Low-mass-resolution ion images (in $^{16}O^-$ and $^{18}O^-$) of oxide grains were digitized, and the $^{16}O/^{18}O$ ratios ($\sigma \approx 4\%$) of individual grains were determined by image processing. Grains that deviated in duplicate analyses by more than 3σ from the solar $^{16}O/^{18}O$ ratio were selected for high-mass-resolution analysis. The high mass-resolving power needed to separate $^{16}OH^-$ ions from the $^{17}O^-$ ions precludes measurement of $^{16}O/^{17}O$ ratios by ion imaging in our instrument.

Ion imaging of $\sim 6,000$ grains yielded 53 candidates, the $^{16}O/^{18}O$ and $^{16}O/^{17}O$ ratios of which were subsequently measured at high mass resolution. Of these grains, 20 corundum (Al_2O_3) and 1 spinel ($MgAl_2O_4$) have a large range of anomalous (non-solar) $^{16}O/^{18}O$ and $^{16}O/^{17}O$ ratios (Fig. 1 and Table 1). Nine of the grains also have large ^{26}Mg excesses, corresponding to initial $^{26}Al/^{27}Al$ ratios of between 1.2×10^{-4} and 7.8×10^{-3}, much higher than the maximim value of 5×10^{-5} observed in primitive Solar System material (Fig. 2 and Table 1). All grains are 0.5–2 μm in size. For purposes of discussion, the 24 interstellar oxide grains found to date were divided into three groups on the basis of their oxygen isotope compositions (Fig. 1 and Table 1). Note that the range of oxygen isotope ratios usually observed in meteorites and terrestrial samples falls within the solar symbol in Fig. 1.

Group 1 grains have significant enrichments in ^{17}O and modest depletions in ^{18}O, similar to the isotopic compositions measured in O-rich red giants[13,14] (Table 1 and Fig. 1). These stars are thought to produce 65–75% of all dust, or ~ 80–90% of O-rich dust, in the Galaxy[8,9]. Because of this similarity, Group 1 grains probably formed in the atmospheres of red giants. The oxygen isotope compositions of such stars have been successfully reproduced by theoretical models in terms of the so-called first dredge-up, which occurs after exhaustion of H in the stellar core[15–18]. In this process, material that has undergone partial core H-burning via the CNO-cycle is mixed into the envelope. These models predict that the first dredge-up significantly decreases the envelope's initial $^{16}O/^{17}O$ ratio, the actual values depending primarily on stellar mass[16–18] (see Fig. 1). But the first dredge-up has only a relatively small effect on the $^{16}O/^{18}O$ ratio (20–50% increase), and larger differences in this ratio must be due to differences in the initial isotopic compositions of different stars[17] (Fig. 1). Such differences are the result of Galactic chemical evolution, reflecting age differences of the stars and/or the spread in chemical compositions observed in newly formed stars within a given Galactic epoch[19]. The range of the oxygen isotope compositions observed in the Group 1 grains indicates that they originated from several distinct stellar sources with different masses as well as different initial compositions.

As red giant stars continue to evolve, they can undergo two additional dredge-up episodes[15]. The second dredge-up occurs only in $>5M_\odot$ stars at the beginning of the asymptotic giant branch (AGB) phase, when He is exhausted in the star's core. The third dredge-up, which is experienced by all stars in the 1–$8M_\odot$ range, occurs during the thermally pulsing (TP) AGB phase when H and He burn alternately in thin shells on top of an inert core consisting now of C and O. These mixing episodes are not expected to significantly change the oxygen isotope composition of the envelope, although some spectroscopic observa-
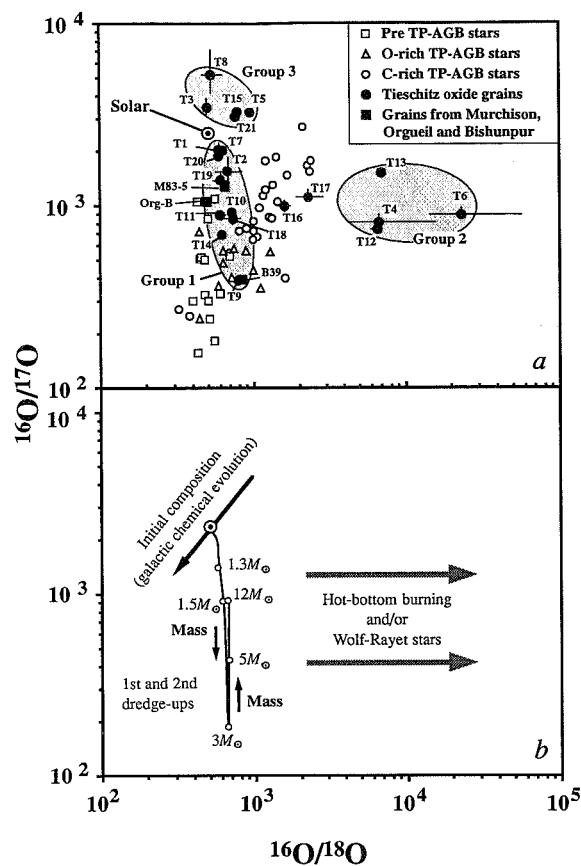

FIG. 1 a, Comparison of the oxygen isotope compositions of 24 interstellar oxide grains reported here and elsewhere[3–7] with those of red giant stars[13,14,20,21]. The red giant stars in a have been divided into three groups based on their spectral types and models of their evolution[15]. The oxide grains have also been divided into three groups based on their oxygen isotope compositions. b, Diagram of the expected oxgyen isotope compositions of red giant envelopes after the first and second dredge-ups as a function of stellar mass and initial composition. After core H-burning ceases, ^{17}O-enriched H-burnt material from the interior is mixed into the O-rich envelope of a red giant during two dredge-up episodes[15] (the second only in $>5M_\odot$ stars). The curve shows the predicted post-dredge-up ratios of stars with initially solar compositions but different masses[18]. The initial $^{16}O/^{17}O$ ratio influences the final ratio only in (1–1.5)$M_\odot$ stars[17]. The $^{16}O/^{18}O$ ratio is only slightly affected by these two dredge-ups[17]. The range of $^{16}O/^{17}O$ and $^{16}O/^{18}O$ ratios amongst Group 1 grains suggests that they come from several stars with different masses and different initial compositions. The initial oxygen isotope compositions, reflecting Galactic evolution, probably varied roughy as indicated (F. Timmes, personal communication). Subsequently, during the thermally pulsing asymptotic giant branch (TP-AGB) phase a third multiple dredge-up episode brings ^{12}C-rich He-burnt material to the surface. As a result, (1–5)$M_\odot$ stars will eventually become carbon stars (C/O > 1), but for (5–8)$M_\odot$ stars, H-burning at the base of the envelope (hot-bottom burning) is predicted to destroy ^{12}C and ^{18}O, thereby preventing formation of a carbon star[31]. Note that oxide grains may form even in carbon-star envelopes[32].

tions of TP-AGB stars suggest that their atmospheres have higher $^{16}O/^{18}O$ and $^{16}O/^{17}O$ ratios than pre-TP-AGB stars[13,14,20,21] (Fig. 1a).

The third dredge-up is expected to bring to the star's surface ^{26}Al that was produced by shell H-burning at much higher temperatures than those reached during core H-burning[22,23]. Models predict envelope $^{26}Al/^{27}Al$ ratios in the range from 5×10^{-4} to 10^{-2}, depending on stellar mass, mass loss rate and evolutionary stage during the TP-AGB phase. Eight of the ten Group 1 grains measured for Al-Mg have inferred initial $^{26}Al/^{27}Al$ ratios in this range (Fig. 2). An alternative production mechanism for ^{26}Al is H-burning at the base of the convective envelope of TP-AGB

TABLE 1   Isotopic compositions of 24 meteoritic interstellar oxide grains

Grain	$^{17}O/^{16}O$	$^{18}O/^{16}O$	$^{26}Mg^*/^{24}Mg$	$^{27}Al/^{24}Mg$	$^{26}Al/^{27}Al$	Group
Solar	3.83×10^{-4}	2.01×10^{-3}				
T1	$5.01\,(39) \times 10^{-4}$	$1.66\,(12) \times 10^{-3}$	$\leqslant 0.033$	$209\,(32)$	$\leqslant 1.6 \times 10^{-4}$	1
T2	$6.6\,(1.1) \times 10^{-4}$	$1.44\,(27) \times 10^{-3}$	$2.04\,(19)$	$263\,(65)$	$7.8\,(2.0) \times 10^{-3}$	1
T7	$5.05\,(22) \times 10^{-4}$	$1.55\,(7) \times 10^{-3}$	$0.369\,(15)$	$139\,(18)$	$2.65\,(37) \times 10^{-3}$	1
T9	$2.63\,(5) \times 10^{-3}$	$1.27\,(5) \times 10^{-3}$	$0.586\,(83)$	$1086\,(98)$	$5.40\,(90) \times 10^{-4}$	1
T10	$1.11\,(3) \times 10^{-3}$	$1.36\,(6) \times 10^{-3}$	$\leqslant 0.042$	$402\,(37)$	$\leqslant 1.0 \times 10^{-4}$	1
T11	$1.14\,(5) \times 10^{-3}$	$1.60\,(10) \times 10^{-3}$	NA	NA	NA	1
T14	$1.47\,(5) \times 10^{-3}$	$1.57\,(9) \times 10^{-3}$	$0.163\,(81)$	$1351\,(271)$	$1.20\,(64) \times 10^{-4}$	1
T18	$1.19\,(8) \times 10^{-3}$	$1.35\,(15) \times 10^{-3}$	NA	NA	NA	1
T19	$7.50\,(74) \times 10^{-4}$	$1.63\,(19) \times 10^{-3}$	NA	NA	NA	1
T20	$5.38\,(16) \times 10^{-4}$	$1.66\,(47) \times 10^{-3}$	$0.0303\,(14)$	$41\,(2)$	$7.34\,(46) \times 10^{-4}$	1
M83-5	$7.92\,(23) \times 10^{-4}$	$1.52\,(5) \times 10^{-3}$	$1.96\,(11)$	$2250\,(109)$	$8.73\,(64) \times 10^{-4}$	1
Org-B	$9.72\,(10) \times 10^{-4}$	$1.99\,(4) \times 10^{-3}$	$1.61\,(3)$	$1840\,(90)$	$8.7\,(1) \times 10^{-4}$	1
B39	$2.60\,(6) \times 10^{-3}$	$1.17\,(4) \times 10^{-3}$	$0.2336\,(104)$	$136\,(14)$	$1.7\,(0.2) \times 10^{-3}$	1
T16	$1.01\,(6) \times 10^{-3}$	$6.21\,(54) \times 10^{-4}$	NA	NA	NA	1/2
T17	$9.12\,(76) \times 10^{-4}$	$4.30\,(89) \times 10^{-4}$	NA	NA	NA	1/2
T4	$1.26\,(11) \times 10^{-3}$	$1.47\,(85) \times 10^{-4}$	$0.064\,(13)$	$17.0\,(2.3)$	$3.77\,(91) \times 10^{-3}$	2
T6	$1.14\,(8) \times 10^{-3}$	$4.3\,(2.6) \times 10^{-5}$	$0.423\,(57)$	$106\,(16)$	$4.01\,(82) \times 10^{-3}$	2
T12	$1.36\,(4) \times 10^{-3}$	$1.50\,(11) \times 10^{-4}$	$0.969\,(81)$	$135\,(11)$	$7.19\,(83) \times 10^{-3}$	2
T13	$6.72\,(24) \times 10^{-4}$	$1.41\,(10) \times 10^{-4}$	$10.4\,(13)$	$5442\,(707)$	$1.90\,(35) \times 10^{-3}$	2
T3	$2.92\,(29) \times 10^{-4}$	$1.98\,(13) \times 10^{-3}$	$\leqslant 0.0048$	$8.2\,(1)$	$\leqslant 6.0 \times 10^{-4}$	3
T5	$3.15\,(11) \times 10^{-4}$	$1.02\,(3) \times 10^{-3}$	$\leqslant 0.0099$	$47\,(6)$	$\leqslant 2.1 \times 10^{-4}$	3
T8	$1.92\,(51) \times 10^{-4}$	$1.85\,(29) \times 10^{-3}$	NA	NA	NA	3
T15	$3.20\,(23) \times 10^{-4}$	$1.26\,(6) \times 10^{-3}$	NA	NA	NA	3
T21	$3.25\,(17) \times 10^{-4}$	$1.29\,(59) \times 10^{-3}$	$\leqslant 0.025$	$549\,(33)$	$\leqslant 4.6 \times 10^{-5}$	3

The (meteorite) source of the grains is shown in the first column; Tieschitz (T), Murchison (M)[4], Orgueil (Org)[3,5,6] and Bishunpur (B)[7]. The grains have been divided into three groups on the basis of their oxygen isotopic compositions. $^{26}Mg^*$ is the excess of ^{26}Mg after correction for mass fractionation, and $^{26}Al/^{27}Al$ is the initial ratio if all $^{26}Mg^*$ results from the in situ decay of ^{26}Al. All errors, in parenthesis, are 1σ and upper limits are 2σ. All grains were analysed by SEM-EDS (Scanning electron microscopy—energy dispersive spectroscopy) after oxygen isotope measurements but before Mg-Al analysis in the ion probe. All but grain T3 appear to be corundum (Al_2O_3). The Al/Mg ratio of grain T3, measured by EDS, is about twice that expected for pure spinel ($MgAl_2O_4$) but much lower than those of the other grains. The ratio obtained in the subsequent ion-probe analysis of T3 is even higher, suggesting that the grain may be an intergrowth of spinel and corundum. The oxygen isotope ratios are given with ^{16}O in the denominator because in the reverse case the errors are asymmetric and nonlinear.

stars of $>5M_\odot$ (hot-bottom burning)[24,25]. But during hot-bottom burning the whole envelope is cycled through the high-temperature H-burning zone, resulting in the destruction of essentially all ^{18}O (producing high $^{16}O/^{18}O$ ratios), in disagreement with the oxygen isotope ratios observed in Group 1 grains. The oxygen isotope and $^{26}Al/^{27}Al$ ratios of these grains thus indicate that at least eight of them come from TP-AGB stars, and at least two from red giants before they reached the TP-AGB phase. It is worth noting that whereas the oxygen isotopes in red giant envelopes can be measured astronomically—albeit

FIG. 2 Plot of the $^{26}Mg/^{24}Mg$ ratio versus the $^{27}Al/^{24}Mg$ ratio in 17 pre-solar oxide grains. The large ^{26}Mg excesses, compared to solar Mg isotopic ratios, are best explained as the result of in situ decay of ^{26}Al. Also shown are Al-Mg evolution lines for five initial $^{26}Al/^{27}Al$ ratios. The $^{27}Al/^{24}Mg$ ratios in most of the Tieschitz corundum grains are not as high as might be expected, possibly because of significant background contributions from isotopically normal Mg to the Mg analysis. However, these contributions do not affect the inferred $^{26}Al/^{27}Al$ ratios.

with larger errors than those obtained in the grains—the determination of $^{26}Al/^{27}Al$ ratios in such stars is only possible from the laboratory analysis of pre-solar grains.

Unlike grains in Group 1, neither Group 2 nor Group 3 grains have spectroscopic counterparts and we must rely solely on comparisons with stellar evolution models to infer their likely sources. Group 2 grains have ^{17}O and ^{26}Al enrichments, and ^{18}O depletions that are much larger than previously observed in any meteoritic material or star. Two other grains, which lie on the edge of the carbon-star field, have intermediate ^{18}O depletions. Relatively low-temperature hot-bottom burning could destroy essentially all ^{18}O in an AGB envelope without significantly changing the ^{26}Al and ^{17}O abundances already established by the first, second and third dredge-ups[17]. Also, such isotopic compositions are predicted to exist at the surface of massive mass-losing stars which have shed their envelopes, exposing the H-burnt interior (Wolf–Rayet stars during the Of-WN phases)[26]. In any case, better modelling and more elemental and isotopic data on Group 2 grains are necessary for distinguishing between the two possible sources.

The Group 3 grains are moderately depleted in ^{17}O relative to the Solar System. They could conceivably have formed around low-mass red giant stars that have experienced the first dredge-up, provided that the initial $^{16}O/^{17}O$ ratios of the stars were higher than the measured grain values and, therefore, the solar value. On the other hand, massive stars ($>10 \, M_\odot$), which contribute ~6–12% of all Galactic dust[8,9], produce large excesses of ^{16}O and ^{18}O in certain shells[27] that could come to the surface as the star loses mass or could be ejected in a supernova explosion.

^{16}O enrichments and depletions with respect to the terrestrial isotopic ratios are common in materials of Solar System origin[28]; in meteorites the enrichments can reach up to 7% in corundum (Al_2O_3) and spinel ($MgAl_2O_4$) from Ca-Al-rich inclusions[29]. These enrichments prompted suggestions that ^{16}O-rich grains, probably corundum and spinel, from a supernova were incompletely mixed into the Solar System[28]. We have not found any
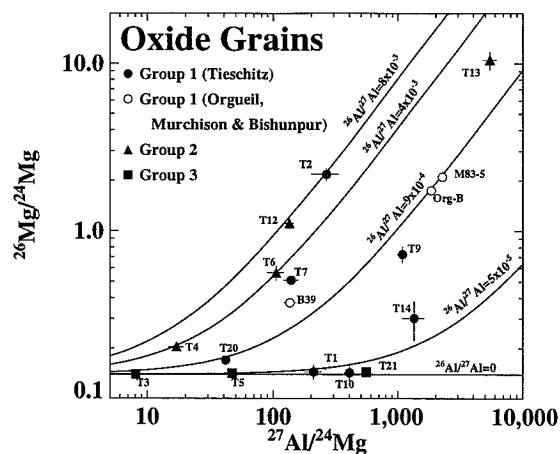
pre-solar grains with large ^{16}O enrichments. The Group 3 grains are ^{16}O-rich, but not with respect to both ^{17}O and ^{18}O. The discovery that ^{16}O can undergo mass-independent gas-phase chemical fractionation from both ^{17}O and ^{18}O has provided an alternative explanation for the observed ^{16}O enrichments in Solar System material[30].

Finally, if the Si/Al ratio is assumed to be solar in all stars and if all Al goes into corundum (Al_2O_3), interstellar corundum appears to be underabundant in meteorites, relative to interstellar SiC, by about a factor of between 20 and 50 (refs 4, 6, 10)

when compaerd to estimated Galactic dust production rates[8,9]. This is in spite of the fact that, in the solar nebula, corundum should have been more stable than SiC. Possible explanations are that interstellar corundum has a finer grain size distribution than SiC and was thus not detected by our technique, that Al primarily condenses in other phases (such as silicates) that are less resistant to the chemical treatments used to isolate the grains or, most speculatively, that corundum has a shorter lifetime in the interstellar medium than SiC. □

1. Anders, E. & Zinner, E. K. Meteoritics **28**, 490–514 (1993).
2. Ott, U. Nature **364**, 25–33 (1993).
3. Huss, G. R., Hutcheon, I. D., Wasserburg, G. J. & Stone, J. Lunar planet. Sci. **XXIII**, 563–564 (1992).
4. Nittler, L. R., Walker, R. M., Zinner, E. K., Hoppe, P. & Lewis, R. S. Lunar planet. Sci. **XXIV**, 1087–1088 (1993).
5. Huss, G. R., Hutcheon, I. D., Fahey, A. J. & Wasserburg, G. J. Meteoritics **28**, 369–370 (1993).
6. Hutcheon, I. D., Huss, G. R., Fahey, A. J. & Wasserburg, G. J. Astrophys. J. **425**, L97–L100 (1994).
7. Huss, G. R., Fahey, A. J., Gallino, R. & Wasserburg, G. J. Astrophys. J. (in the press).
8. Gehrz, R. D. in Interstellar Dust (eds Allamandola, L. J. & Tielens, A. G. G.) 445–453 (Kluwer Academic, Dordrecht, 1989).
9. Whittet, D. C. B. Dust in the Galactic Environment, 295 (Institute of Physics, Bristol, 1992).
10. Nittler, L. R., Alexander, C. M. O'D., Gao, X., Walker, R. M & Zinner, E. K. Lunar planet. Sci. **XXV**, 1005–1006 (1994).
11. Gao, X., Alexander, C. M. O'D., Swan, P. D. & Walker, R. M. Lunar planet. Sci. **XXV**, 401–402 (1994).
12. Zinner, E. K., Tang, M. & Anders, E. Geochim. cosmochim. Acta **53**, 3273–3290 (1989).
13. Harris, M. J. & Lambert, D. L. Astrophys. J. **285**, 674–682 (1984).
14. Smith, V. V. & Lambert, D. L. Astrophys. J. Suppl. Ser. **72**, 387–416 (1990).
15. Iben, I. Jr. Astrophys. J. Suppl. Ser. **76**, 55–114 (1991).
16. Dearborn, D. S. P. Phys. Rep. **210**, 367–382 (1992).
17. Boothroyd, A. I., Sackmann, I. J. & Wasserburg, G. J. Astrophys. J. (in the press).
18. El Eid, M. F. Astr. Astrophys. **285**, 915–928 (1994).
19. Edvardsson, B. et al. Astr. Astrophys. **275**, 101–152 (1993).
20. Harris, M. J., Lambert, D. L., Hinkle, K. H., Gustafsson, B. & Eriksson, K. Astrophys. J. **316**, 294–304 (1987).
21. Kahane, C., Cernicharo, J., Gomez-Gonzalez, J. & Guelin, M. Astr. Astrophys. **256**, 235–250 (1992).
22. Forestini, M., Paulus, G. & Arnould, M. Astr. Astrophys. **252**, 597–604 (1991).
23. Gallino, R., Raiteri, C. M., Busso, M. & Matteucci, F. Astrophys. J. (in the press).
24. Nørgaard, H. Astrophys. J. **236**, 895–898 (1980).
25. Cameron, A. G. W. in Protostars and Planets III (eds Levy, E. H. & Lunine, J. I.) 47–73 (Univ. Arizona Press, 1993).
26. Prantzos, N., Doom, C., Arnould, M. & de Loore, C. Astrophys. J. **304**, 695–712 (1986).
27. Woosley, S. E. in Nucleosynthesis and Chemical Evolution (eds Hauck, B., Maeder, A. & Meynet, G.) 1–195 (Observatoire de Genève, Geneva, 1986).
28. Clayton, R. N., Grossman, L. & Mayeda, T. K. Science **182**, 485–488 (1973).
29. Virag, A., Zinner, E. K., Amari, S. & Anders, E. Geochim. Cosmochim. Acta **55**, 2045–2062 (1991).
30. Thiemens, M. H. & Heidenreich, J. E. Science **219**, 1073–1075 (1983).
31. Renzini, A. & Voli, M. Astr. Astrophys. **94**, 175–193 (1981).
32. Lattimer, J. M., Schramm, D. N. & Grossman, L. Astrophys. J. **219**, 230–249 (1978).

CONTINUED STUDIES OF INTERSTELLAR SIC GRAINS OF TYPE X;

L. Nittler, S. Amari, K. Kehm, R. Walker, and E. Zinner, McDonnell Center for the Space Sciences and Dept. of Physics, Washington University, St. Louis, MO 63130-4899, USA. R. Lewis, Enrico Fermi Institute, University of Chicago, 5630 Ellis Ave., Chicago, IL 60637-1433, USA.

Previous studies have demonstrated the usefulness of quantitative isotopic imaging in the ion microprobe for efficiently locating rare presolar dust grains in meteorites [1-5]. To better characterize rare subsets of interstellar SiC grains, we have continued ion imaging searches in separates of the Murchison carbonaceous chondrite. Silicon isotopic mapping of 2750 SiC grains from Murchison separate KJG (average size 3μm) revealed 22 new members of the rare ($\lesssim$ 1%) sub-class of SiC, known as grains X [6]. We analyzed these by SIMS for their Si, C, and N isotopic compositions, and fourteen grains by laser gas extraction for their He, Ne, Ar, Kr and Xe compositions. None carry noble gases above detection limits. The 75-odd Murchison X grains found to date [2,5-6] have C, N, Si, Al, Ca, and Ti isotopic ratios qualitatively consistent with a type II supernova origin, although mixing of different nuclear burning zones must have occurred and several puzzles remain. There appear to be at least four distinct sub-groups of the X grains, based on their silicon isotopic compositions.

Of 2750 imaged KJG SiC grains, twenty-two showed high $^{28}Si/^{30}Si$ ratios, characteristic of X grains. High-mass-resolution analyses of C, N, and Si isotopic ratios in the grains confirmed excesses of ^{15}N and ^{28}Si and a wide range of C-isotopic ratios (Figures), as previously observed in X grains [2,6]. Subsequent laser gas extraction analysis of fourteen of the grains found none with detectable noble gases. Previous noble gas studies of individual interstellar SiC grains have shown that only a small fraction ($\sim$5%) are gas-rich [7]. The lack of gas-rich grains in the current sample may be due to the small number of grains or to extensive sputtering in the ion probe prior to noble gas measurements. On the other hand, X grains may be fundamentally different with respect to noble gases, as they are with respect to their other elements. Additional noble gas measurements on a larger sample of X grains are planned.

The silicon isotopic compositions of 34 KJG and two KJH X grains [2,6] are shown in Figure 1. All of the grains are highly enriched in ^{28}Si, relative to the solar system. Most of the grains lie above a mixing line of slope 1 between pure ^{28}Si and solar system Si, and have been labeled X-A [5]. The best-fit line to these grains has a slope of 0.69±.03 and passes through the origin, although there is considerable scatter about this line. A few grains lie on or near the slope 1 line and represent the sub-population X-B [5]. One KJG grain (245-4) lies well below the others and represents a new sub-type, X-D (X-C also has only one member, which lies above the other data [5]). All of the KJG and KJH X grains have isotopically heavy N: $^{14}N/^{15}N$ = 13-181 (Solar ratio=272) (Figure 2), and typically have higher N contents than "mainstream" SiC. Carbon in these X grains, on the other hand, ranges from very heavy to very light ($18 < ^{12}C/^{13}C < 2500$), relative to the solar ratio of 89 (Figure 2). Previous measurements have revealed extremely high $^{26}Al/^{27}Al$ ratios (0.1 - 0.6) in all of the nine X grains where Al-Mg measurements were possible, as well as enrichments in ^{49}Ti in four grains and ^{44}Ca in one grain [2,6].

Type II supernovae (SN) have been proposed as the most likely stellar sources for X grains [6], and they can explain, in principle, most of the isotopic signatures found in these grains, provided different zones within the pre-supernova star are selectively mixed during the explosion. Zinner et al.[8] have explored mixing in supernova models of different masses, and have successfully reproduced the isotopic compositions of a class of interstellar graphite grains. Although their results provide strong evidence for extensive mixing in supernova ejecta, there are some serious problems to quantitatively account for the isotopic compositions of SiC X grains by the same scheme. The low $^{14}N/^{15}N$ ratios and high $^{12}C/^{13}C$ ratios seen in most X grains point to a contribution from the He-burning region of the pre-SN star, whereas high $^{26}Al/^{27}Al$ ratios and low $^{12}C/^{13}C$ ratios indicate a significant contribution from the overlaying zone, where H-burning by the CNO cycle

has occurred. But this zone has much more nitrogen than the partially He-burnt zone, and this N is essentially pure ^{14}N, making it difficult to reconcile ^{26}Al and ^{13}C excesses with the ^{15}N excesses characteristic of all X grains, and to explain the high N contents of the grains. The silicon isotopic compositions of X grains can be explained qualitatively by invoking mixing of material from the inner O- and Ne-burning zones of the star, which produce essentially pure ^{28}Si, with the outer H- and He-burning regions. Ca and Ti anomalies in X grains also point to a contribution from these inner zones [6,9]. However, problems arise when attempting to quantitatively reproduce the observed silicon isotopic ratios. In particular, the enrichment of ^{29}Si relative to ^{30}Si in grains X-A is not predicted in regions with appreciable amounts of ^{28}Si [10].

Ion imaging provides an efficient method for identifying relatively large numbers of the rare class of interstellar dust, SiC grains X. Together with low density graphite grains [8-9], and perhaps the recently discovered nitrides [11-12], these interesting grains are sensitive probes of the complicated physics of exploding stars. Further isotopic measurements on these grains, particularly of trace elements such as noble gases, Ca and Ti, will likely provide ever more stringent constraints on models of supernovae and on the number of such stars which contributed material to the solar nebula.

REFERENCES [1] Nittler, L. R. *et al.*(1993) *LPS* **24**, 1087. [2] Nittler, L. *et al.*(1993) *Meteoritics* **28**, 413. [3] Nittler, L. R. *et al.*(1994) *Nature* **370**, 443. [4] Hoppe, P. *et al.*(1994) *Meteoritics* **29**, 474. [5] Hoppe, P. *et al.*(1995) This volume. [6] Amari, S. *et al.*(1992) *Ap. J.* **394**, L43. [7] Nichols, R. H., Jr. *et al.*(1993) *Meteoritics* **28**, 410. [8] Zinner, E. *et al.*(1995) This volume. [9] Amari, S. *et al.*(1995) This volume. [10] Woosley, S. E. and Weaver, T. A. (1995) *Ap. J.* submitted. [11] Alexander, C. M. O'D. (1993) *GCA* **57**, 2869. [12] Hoppe, P. *et al.*(1994) *LPS* **25**, 563.

Figure 1

Figure 2
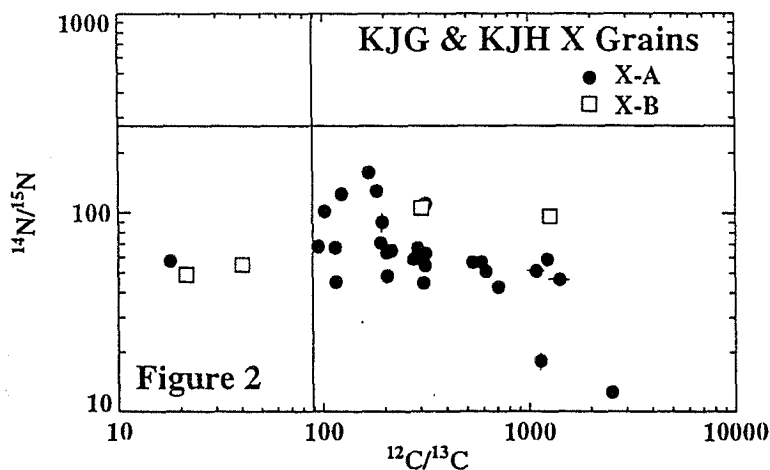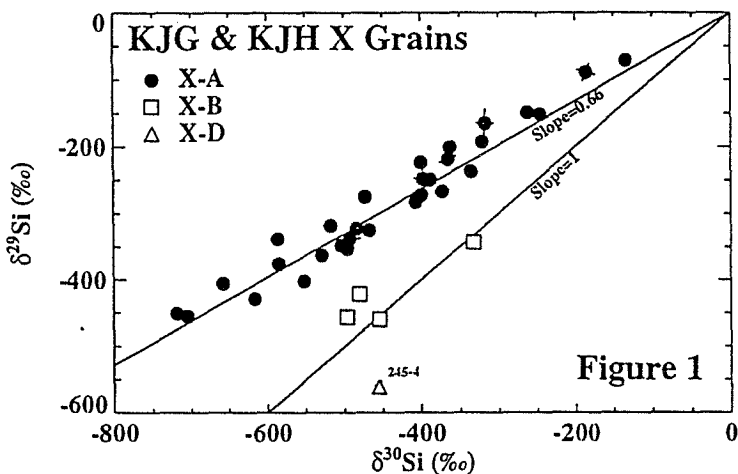
intent to preserve the samples themselves under clean room conditions for the indefinite future and to make sure that adequate documentation is maintained so that access to the samples is not compromised by future changes in laboratory personnel. It will likely be a long time before an experiment as large and specialized as AO187-2 will be flown in space for an extended duration – LDEF is unique in this respect.

REFERENCES

1.	Amari S., Foote J., Simon C., Swan P., Walker R.M., Zinner E., Jessberger E.K., Lange G., and Stadermann F. (1991) SIMS chemical analysis of extended impact features from the trailing edge portion of experiment AO187-2. In *LDEF – 69 Months in Space. First Post-Retrieval Symposium* (A.S. Levine, ed.), NASA CP-3134 (Part 1), 503-516.

2.	Amari S., Foote J., Swan P., Walker R.M., Zinner E., and Lange G. (1993) SIMS chemical analysis of extended impacts on the leading and trailing edges of LDEF experiment AO187-2. In *LDEF – 69 Months in Space. Second Post-Retrieval Symposium* (A.S. Levine, ed.), NASA CP-3194 (Part 2), 513-528.

3.	Stadermann F. J., Amari S., Foote J., Swan P., Walker R.M., and Zinner E. (1995) SIMS chemical and isotopic analysis of impact features from LDEF experiments AO187-1 and AO187-2. In *LDEF–69 Months in Space. Third Post-Retrieval Symposium* (A.S. Levine, ed.), NASA CP-3275, 461-473.

4.	Amari S., Foote J., Simon C., Swan P., Walker R., Zinner E., and Jessberger E. K. (1990) Micrometeoroid experiment on the long duration exposure facility. *Meteoritics* **25**, 347-348.

5.	Amari S., Foote J., Jessberger E. K., Simon C., Stadermann F., Swan P., Walker R.M., and Zinner E. (1991) SIMS analysis of micrometeoroid impacts on LDEF. *Meteoritics* **26**, 313.

6.	Amari S., Foote J., Simon C., Swan P., Walker R. M., Zinner E., Jessberger E. K., Lange G., and Stadermann F. (1992) SIMS chemical analysis of extended impacts on the leading and trailing edges of LDEF experiment AO187-2. *LPSC* **XXIII**, 25-26.

7.	Stadermann F. J. (1994) Trajectory calculation of individual particles from LDEF impacts. *LPSC* **XXV**, 1327-1328.

8.	Nittler L., Alexander C.M.O'D., Gao X., Walker R.M., and Zinner E. (1994) Interstellar oxide grains from the Tieschitz ordinary chondrite. *Nature* **370**, 443-446.

9.	Nittler L., Amari S., Kehm K., Walker R., and Zinner E. (1995) Continued studies of interstellar SiC grains of type X. *LPSC* **XXVI**, 1057-1058.